

**STRUCTURAL STUDIES OF HUMAN IMMUNODEFICIENCY VIRUS TYPE 1
BY CRYO-ELECTRON TOMOGRAPHY**

Thesis by
Jordan Benjamin

In Partial Fulfillment of the Requirements
for the Degree of
Doctor of Philosophy

California Institute of Technology

Pasadena California

2006

(Defended May 23, 2006)

© 2006

Jordan Benjamin

All Rights Reserved

ACKNOWLEDGEMENTS

I would like to thank my advisor, Grant Jensen, for all the support and guidance I have received over the years. He has always been extremely accessible, and is a man of great vision and optimism. His enthusiasm for science is truly inspirational. It has been an honor to be his first graduate student.

Wes Sundquist has been a wonderful collaborator on the HIV project. He has generously hosted us in his laboratory during the past four years, and I have greatly enjoyed our discussions. His knowledge and insight into virology is humbling.

I am very grateful to my committee members Pamela Björkman, Scott Fraser, and Ellen Rothenberg for generously giving me their feedback, advice, and acerbic wit. It's been a real pleasure to have been brought into contact with Paul Sternberg, Ray Deshaies, and Henry Lester, who are extraordinary scientists and exceptional teachers. Liz Ayala has been an invaluable source of help and is a credit to the division.

Thanks to all the members of the Jensen lab, especially: Greg Henderson and Gavin Murphy for being there with me (almost) from the beginning, and for being good neighbors; Bill Tivol, Prabha Dias, and Cristina Iancu for all their help over the years; Ariane Briegel for making the lab a more fun place to work; Jane Ding for technical assistance; Dylan Morris, Peter Leong, and Christian Suloway for carrying the lab into the future. Special thanks to Liz Wright, for joining me on the HIV project, and for being a wonderful colleague and friend.

For everything outside of the lab, I thank Julien Muffat, Mark Zarnegar, Meghan Adams, Amber Southwell, Tim Chung, Michal Brown, Alice Robie, Lori Lee, and all the other great friends I've found at Caltech. Hamburger Hamlet, Burger Continental, and

Amigo's greatly improved the graduate school experience. I am highly indebted to Bank of America, Chase, and American Express, but that's another story. I am very grateful for SPC and everyone there, especially my fellow "midnight cowboys" from the I & II shifts.

Devin Tesar has been an amazing friend, and so he gets his own paragraph. He is indeed a comic genius. Without him it is unlikely I would be writing this document now.

Finally, my deepest gratitude goes to Jennifer Schooler, the love of my life. She makes it all worthwhile, and it is to her that I dedicate this dissertation.

ABSTRACT

Gag, the major structural component of the type 1 human immunodeficiency virus (HIV-1), comprises the matrix (MA), capsid (CA), nucleocapsid (NC), and p6 proteins, as well as the SP1 and SP2 spacer peptides. In the immature HIV-1 virion, the domains of Gag are arranged radially with the amino-terminus of MA at the membrane. Mature viral particles are formed when Gag is proteolytically cleaved, allowing CA to reassemble into the viral core, which contains NC bound to genomic RNA. While the structures of nearly every HIV-1 protein are known in atomic detail from X-ray crystallography and NMR spectroscopy, many questions remain about the intermolecular interactions in both the immature and mature particles.

We have obtained three-dimensional structures of individual immature and mature HIV-1 virus-like particles by cryoelectron tomography. Reconstructions of the mature particles revealed diverse core morphologies with a preference for conical shapes consistent with 5,7 fullerene cones. Uniform positioning of the wide end of the cores and an internal density likely to be the NC/RNA complex were also observed, as were multiple and nested viral cores. Our results support the fullerene cone model for the core structure and suggest that specific interactions may occur between the CA, MA, and NC layers in the mature virion. These experiments also aided the characterization of a new cryostage allowing routine collection of dual-axis tomograms.

Tomograms of the immature virions revealed patches of hexagonally ordered Gag molecules interspersed with regions of disordered or absent Gag. We developed novel tools for analysis of locally ordered lattices embedded in curved structures, including a method for locating and averaging the Gag unit cell in situ. The unit cell average revealed that the CA domains and the SP1 spacer peptides were organized in a hexagonal lattice with ring-to-ring spacing of 8 nm in the CA layer and 7.5 nm in SP1. No regular lattice was found in the MA or NC layers. Based on the averaged Gag unit cell, we proposed a pseudoatomic model for the CA and SP1 domains in the immature virion.

TABLE OF CONTENTS

ACKNOWLEDGEMENTS.....	iii
ABSTRACT.....	v
TABLE OF CONTENTS.....	vi
LIST OF TABLES AND FIGURES.....	viii
Chapter 1: Introduction.....	1
Virion Components.....	1
Viral Life Cycle: Early.....	2
Viral Life Cycle: Late.....	3
Morphology and Maturation.....	4
Matrix.....	6
Capsid.....	7
Fullerene Cone Model.....	10
Maturation Switches.....	11
Cryoelectron Tomography.....	13
Personal Contributions.....	14
References.....	15
Figures.....	30
Chapter 2: Three-dimensional structure of HIV-1 virus-like particles by electron cryotomography.....	35
Abstract.....	36
Introduction.....	37
Results.....	40
Discussion.....	45
Materials and Methods.....	51
Acknowledgements.....	53
References.....	54
Figure and table legends.....	60
Chapter 3: Immature HIV-1 virus-like particles imaged by electron cryotomography....	69
Abstract.....	70
Introduction.....	71
Results.....	73
Discussion.....	76
Materials and Methods.....	79
Acknowledgements.....	82
References.....	82
Figures.....	88
Appendix A: A “flip-flop” rotation stage for routine dual-axis electron cryotomography	99
Abstract.....	100
Introduction.....	101
The flip-flop rotation stage.....	103
Technical characterization.....	105
Qualitative comparisons of single- versus dual-axis tomograms.....	106

Novel data processing challenges	109
Size of the missing pyramid in single- versus dual-axis data collection	112
Discussion	114
Acknowledgements	116
References	117
Figure and table legends.	120

LIST OF TABLES AND FIGURES

Figure 1-1. Matrix protein trimer.....	30
Figure 1-2. Capsid amino and carboxy terminal domains.....	31
Figure 1-3. Capsid NTD maturation.....	32
Figure 1-4. N-MLV capsid NTD hexamer.....	33
Figure 1-5. Fullerene cone model.....	34
Figure 2-1. Primary data and processing steps.....	60
Figure 2-2. Montage of all segmented HIV-1 VLPs.....	62
Figure 2-3. Nested capsids.....	64
Figure 2-4. Cone angle variation in 3D.....	65
Figure 2-5. Conserved patterns of density in VLPs.....	66
Table 2-1. Surface area measurements.....	67
Figure 3-1. Primary data and tomogram.....	88
Figure 3-2. Gag sectors and associated membrane structure.....	89
Figure 3-3. Immature HIV-1 VLP and radial density plot.....	90
Figure 3-4. Gag shell surface projections of an immature HIV-1 VLP.....	91
Figure 3-5. Ordering of the Gag polyprotein within the immature HIV-1 VLP.....	92
Figure 3-6. Analysis of the surface projection of the CA protein within one immature HIV-1 VLP.....	93
Figure 3-7. Montage of the averaged unit cell of an immature HIV-1 VLP.....	94
Figure 3-8. Averaged unit cell with radial density plot.....	95
Figure 3-9. Top view of Gag components docked into the averaged density.....	96
Figure 3-10. Side view of Gag components docked into the averaged density.....	97
Figure 3-11. Comparison of immature and mature lattices.....	98
Figure A-1. Flip-flop rotation stage.....	120
Figure A-2. Single- and dual-axis tomograms of an intact cell.....	122
Figure A-3. Single- and dual-axis tomograms of an HIV-1 virus-like particle.....	124
Figure A-4. Single- and dual-axis tomograms of prokaryotic carboxysomes.....	126
Figure A-5. Single- and dual-axis tomograms of individual protein complexes.....	127
Figure A-6. Missing pyramid and intensity scaling.....	129
Figure A-7. Diagram used to find the area of the “missing pyramid.”.....	130
Table A-1. Percent coverage of reciprocal space in single- and dual-axis tomography.....	131

Chapter 1: Introduction

HIV-1 is the causative agent of AIDS, a disease afflicting ~40 million people worldwide [1]. A vast effort has been directed at understanding the structure, function, and life cycle of this virus, with substantial results. The atomic structures of all viral enzymes, structural proteins, and accessory proteins (except Vif) have now been determined by X-ray crystallography, NMR, or both [2, 3]. Many of the most important remaining structural questions about HIV concern the higher-order structures of these proteins.

Virion Components

HIV-1 is a member of the lentivirus subfamily of retroviruses. Its virions contain two copies of a 9.2 kb RNA genome bearing the gag, pol, and env genes common to all retroviruses, as well as the nef, tat, rev, vif, vpr, and vpu genes, of which rev and tat are shared by all other lentiviruses. At the 5' and 3' ends of the genome are long terminal repeats (LTRs) that are important for integration and transcription. The gag gene encodes the 55 kDa Gag polyprotein, which comprises the structural proteins matrix (MA), capsid (CA), spacer peptide 1 (SP1 or p2), nucleocapsid (NC), spacer peptide 2 (SP2 or p1), and p6. Contained in the pol open reading frame are the viral enzymes protease (PR), reverse transcriptase and RNase H (RT), and integrase (IN). The pol gene is not expressed on its own, but only after a -1 frameshift at the gag stop codon, leading to the production of the 160 kDa Gag-Pro-Pol polyprotein. This frameshift is mediated by a 12 bp RNA stem loop in the viral genome, and occurs at a rate of about 5% [4, 5]. Both the Gag and Gag-Pro-Pol gene products are processed by viral protease. Finally, the env gene encodes the

envelope proteins gp120 (SU) and gp41 (TM), which are glycosylated in the host endoplasmic reticulum and cleaved from each other by host cell proprotein convertases in the Golgi apparatus [6-8].

Viral Life Cycle: Early

In the early phase of the viral life cycle, the HIV envelope complexes gp120/gp41 bind to the CD4 receptor on the surface of a host cell, as well as one of the chemokine receptors CCR5 or CXCR4 (reviewed in [9]). Through a conformational change in the gp41 transmembrane anchor, the host and viral plasma membranes will fuse, leading to viral entry into the cell. This is an inefficient process that is accomplished by only about one in one thousand retroviruses [10]. It is of interest to the structural biologist to know whether this is because most of the viruses are defective from the beginning, or if they simply fall victim to rapid decay and a difficult entry process. Results from mathematical modeling suggest that a relatively high proportion of the viruses are infective, but that adsorption to the cell is limited by the slow rate of diffusion and the short half-lives of the particles [11-13].

Little is known about what happens immediately after viral entry, but it appears that the viral core forms a particle known as the reverse transcription complex (RTC), which crosses the actin cytoskeleton with the aid of the viral protein Nef [14-16]. The RTCs are then transported toward the nucleus using dynein motors and the microtubule network [17, 18]. Reverse transcription then occurs in the nucleus, and the capsid is dismantled in a process known as uncoating, which leads to the formation of the preintegration complex (PIC). Uncoating is regulated by interactions with host factors [19]. The role of the structural proteins in these complexes is unclear, although there is

evidence that at least some CA protein remains associated with the RTC after entry into the cell, and that this must be removed for successful formation of the PIC [17, 20-23]. Successful integration of the DNA provirus into the host cell's genome marks the end of the early phase.

Viral Life Cycle: Late

The late phase of the replication cycle begins with the transcription of genomic RNA via host RNA polymerase II [2]. This occurs through the action of the promoter found in the viral LTRs in concert with the host cell transcription factor NF- κ B, but may also be mediated by the basal activity in the region of chromatin where the provirus integrated. In contrast to other retroviruses, transcription of HIV-1 RNA products only occurs from DNA integrated into the host genome. The HIV-1 RNA transcripts are alternatively spliced into more than 40 different final forms, in addition to the full-length copies that will be packaged into new virions. Export of the unspliced genomic RNAs from the nucleus is facilitated by the viral protein Rev and the *cis*-acting sequence RRE (Rev Response Element). Translation of gag mRNA appears to be mediated by an internal ribosome entry site (IRES) within the gag open reading frame itself [24].

As Gag molecules are produced, their NC domains bind to genomic RNA, leading to multimerization [25-28]. This is important for both genome packaging (reviewed in [29]) and particle assembly. The NC domain appears to control the preferential packaging of dimeric RNA bearing signals from the 5' untranslated regions (UTRs) of the HIV-1 genome [30-32], although its role in particle assembly does not require specific interactions with viral RNA [33, 34]. At the same time, Gag molecules are transported to the cell membrane by an unknown mechanism, where the MA domains bind to the

phospholipids of the membrane, leading to the formation of arrays of Gag (and Gag-Pro-Pol) bound to genomic RNA. As the Gag arrays assemble they induce local curvature of the membrane, eventually forming closed spherical shells that may contain up to ~5,000 monomers [35]. Also present in the membranes of the budding particles will be the viral Env proteins and various host membrane proteins, while the particles will contain in their Gag shells two copies of the RNA genome and numerous other viral and host proteins.

During the budding process, the Gag domain p6 recruits Tsg101, a cellular protein that is part of ESCRT-1 (endosomal sorting complex required for transport) [36-38]. Tsg101 normally binds ubiquitin during the processing of proteins in multivesicular bodies, but can also bind the PTAP motif of p6 [37, 39-44]. Through a mechanism that is still unknown, this complex facilitates the completion of the budding process. The viruses will then undergo a series of proteolytic cleavages of the Gag and Gag-Pol polyproteins, releasing matrix, capsid and nucleocapsid [45]. This leads to the maturation process that will be described in the next section.

Morphology and Maturation

The morphology of the immature virion is dominated by the roughly spherical Gag shell inside of a lipid membrane derived from the host cell [46-50]. The Gag molecules are bound to the membrane *via* their myristoylated N-terminal glycine residues as well as basic residues at the upper surface of the MA domains. The RNA genome and other viral proteins are contained within this shell, and trimers of Env comprising the transmembrane gp41 and extracellular gp120 are distributed throughout the membrane [2]. Gag expressed alone in insect and human cells will assemble at the plasma membrane and bud off into spherical virus-like particles, with no other viral proteins

being necessary for this assembly [46, 48]. These virus-like particles and the immature virions appear roughly spherical, sometimes with a faceted appearance. Image processing of cryo-EM projections does not indicate icosahedral symmetry, despite some initial reports to the contrary [46, 48, 49, 51]. Hexagonal lattices with spacing around 8 nm have been observed in the Gag layer of the immature particles. Although the structure of Gag monomers at high resolution is not known, radial density averages are consistent with the individual domains of the Gag proteins adopting an extended conformation along radial spokes, and the same organization has been observed in immature M-MuLV [35, 46-48, 52].

Following budding, the Gag polyprotein is cleaved to yield MA, CA, NC, and two spacer peptides [45]. This results in the loss of the radially organized Gag shell and the formation of a cone shaped electron dense core of capsid protein, with NC and the genomic RNA contained within it [53]. There is evidence that as little as 30% of CA protein is used to form the conical core *in vivo*, indicating that core formation may partly be concentration-driven [35, 54, 55]. Although the precise timing of these events is not known, it is clear that it is a regulated process. The five protease sites are cleaved at different rates *in vitro*, such that the first cleavage would separate SP1 from NC, then MA/CA and SP2/p6, and finally CA/SP1 and NC/SP2 [56, 57]. This, combined with mutational analysis, led to a model in which the cleavage of NC from SP1 allows condensation of the RNA/NC complex, followed by the reorganization of capsid once the MA/CA and CA/SP1 sites are cleaved [45]. The timing and order of the proteolysis appears to be regulated in part by the dimerization of PR, which is required for its activity [58, 59]. In addition, it has been shown that the cleavage of PR from Gag-Pro-Pol is an

intramolecular reaction [60], and that when PR is embedded in the Gag-Pro-Pol precursor, its specificity is altered such that it preferentially cleaves itself free before processing other substrates [61]. Finally, it is not entirely clear when proteolysis begins. It had been reported that PR was active in the cytoplasm of infected cells [62], and subsequently that the activity of PR began at the membrane prior to budding and was required for optimal budding efficiency [63]. However, other groups have been able to obtain large quantities of immature particles by inactivating protease, and assembly was not compromised. Additionally, expression of a single-chain PR dimer abolished assembly and infectivity, but particle assembly could be restored by a protease inhibitor [64, 65]. This suggests that viral assembly requires that the activation of PR be delayed, possibly by slowing the rate of dimerization. Interestingly, when particles were produced in the presence of protease inhibitors, removal of the inhibitors did not restore infectivity, nor did it result in morphological changes associated with maturation, possibly indicating that some level of PR activity is necessary during particle formation [66].

Matrix

Structures of matrix proteins from HIV and several related viruses have been solved by X-ray crystallography and NMR (Figure 1-1) [67-69]. The structures are all highly similar, even in cases of low sequence identity. HIV MA consists of five helices and a three-strand beta sheet, with the N-terminal glycine myristoylated [68]. The protein crystallized in three different lattice forms, all as trimers. In the two lattices yielding high-resolution diffraction data, the structures and crystal contacts were identical, and

they were very similar in the SIV crystal structure; SIV and HIV MA are about 50% identical at the primary sequence level.

As with the Gag shell of the immature virion, the quaternary structure of the matrix layer in the mature particle is not known. Evidence for icosahedral symmetry has not been obtained [70], leading to the suggestion that the matrix may be globally disordered with local order, although it has been suggested that it could be a flexible or distorted icosahedron [71]. A model for an MA lattice structure has been proposed based on crystal structures, cryo-EM data from the Gag shell, and molecular modeling [71]. The model consists of a threefold symmetric lattice of hexagonal rings, with ring spacing of 7 nm and 4 nm holes in the rings. It is proposed that the transmembrane Env component gp41 binds in the rings, which is supported by mutational analysis indicating that some ring-lining residues of MA are important for Env binding. However, several lines of evidence indicate that MA may not form an ordered lattice in the mature virion. MA has been shown to be dispensable for virion assembly [72-74] and replication [75], so long as the N-terminal myristoylation is retained. Cryo-EM studies in projection have also failed to find evidence of a regular MA lattice in immature particles [47].

Capsid

As with matrix, the structure of capsid has been determined in several forms by NMR and X-ray crystallography (Figure 1-2) [76-80]. The protein is divided into an N-terminal domain (NTD) of 145 residues separated by a 15-residue flexible linker from the 70 residue C-terminal domain (CTD). Gag radial density plots indicate that these domains are also separate in the polyprotein. The NTD is a flattened molecule composed of seven α -helices in a roughly parallel arrangement, except for helices 5 and 6, which are

oriented perpendicularly near the N-terminus. A 17 residue loop between helices 4 and 5 is the site at which cyclophilin A binds [79]. Upon proteolytic cleavage from the Gag precursor, the N-terminus refolds to form a salt bridge between a highly conserved and deeply buried aspartate (D51) and the newly N-terminal proline, creating a β -hairpin structure that can act as a dimerization interface [81]. This β -hairpin appears to be important for *in vitro* assembly of capsid tubes, *in vivo* capsid formation, and viral reproduction, but not Gag shell assembly [82]. In the NMR structure of the Gag fragment containing MA and the CA N-terminal domain the β -hairpin is not formed and the corresponding region exists as a disordered linker (Figure 1-3) [83]. The structure of a hexamer of CA NTDs from the related N-tropic murine leukemia virus has been determined by X-ray crystallography, revealing a ring 90 Å in diameter and 40 Å thick, with the oligomerization interface comprising the β -hairpins and an 18-helix bundle formed by helices 1, 2, and 3 (Figure 1-4) [84].

The CTD has a globular structure composed of four α -helices. Helix 1 contains the highly conserved 20-residue major homology region (MHR), which is essential for viral assembly [72]. Constructs comprising CA residues 146–231 and 151–231 crystallized with different dimer interfaces, both mainly involving helix 2 [77, 85]. The CTD also forms dimers in solution [77] and, along with the SP1 spacer peptide at its C-terminus, has been shown to be absolutely required for viral particle assembly and replication [72, 74, 86-88]. A crystal structure of a SCAN (SRE-ZBP, CTfin-51, AW-1, Number 18 cDNA) domain revealed a domain-swapped CA CTD homolog, and it was proposed that this may represent an intermediate in the process of virion formation [89].

Capsid protein appears to form a broad range of higher-order structures, indicating considerable flexibility in its self-association. It has been shown that recombinant CA protein can form cones and cylinders in the presence of high salt concentration, such as 1M NaCl [90]. CA-NC expressed *in vitro* can also form tubes and cones if provided with RNA or high salt [91, 92]. In another experiment, the structures showed pH dependence, where a transition from spheres to tubes occurred around pH 6.8 [93]. Below pH 6.6 the protein existed only as dimers. Such sensitivity to environmental conditions is consistent with a model in which capsid protein has multiple quaternary structures that are energetically very close to each other.

A study of *in vitro* assembled CA-NC tubes using cryoelectron microscopy exploited the helical symmetry of the tubes to obtain reconstructions at 20–30 Å resolution [92]. Nine reconstructions were obtained with great variability in unit cell orientation, as well as hexamer spacing ranging from 100 to 115 Å. By manually docking the crystal structures into the electron density from the cryoEM reconstructions, a model was made in which the NTDs formed hexamers with helices 1 and 2 and the β -hairpins at the center, with adjacent hexamers connected by CTD dimers. The model agrees well with the N-MLV CA NTD hexamer crystal structure solved several years later [84]. Two-dimensional crystallography of CA from Moloney murine leukemia virus showed a similar lattice with 80 Å spacing, and it was proposed that all the observed CA structures could be explained by changes in the positions of the CTD dimers relative to the NTD hexamers, *via* the flexible linkers connecting them [94]. A similar lattice with 96 Å spacing was found in tubular cores from mature viruses *in vivo* using Fourier filtration of cryoEM projection images [53].

The results mentioned in the previous paragraph were all obtained with CA constructs that would correspond to the mature form, and no data about the immature lattice is available to that resolution. Membrane-bound CA proteins imaged by two-dimensional electron crystallography in negative stain have formed hexagonal networks with spacings of 64 Å and 91 Å [95, 96]. The construct yielding a spacing of 64 Å differed from the 91 Å construct only by the addition of 13 residues at the N-terminus, and reconstructions of the more tightly spaced lattice revealed close NTD dimers not present in the larger form; it was proposed that the closely spaced lattice represented the immature Gag network. Those numbers are reasonably consistent with other results when the shrinkage from negative staining is taken into account, which can be upwards of 10%. A similar study using a Gag construct truncated after the NC domain, but still containing full length MA and CA, found a hexamer spacing of ~80 Å [97]. Electron microscopy of immature virions has found evidence of hexagonal lattices with spacings of ~80 Å *in vivo* [35, 47, 48].

Fullerene Cone Model

The fullerene cone model has been proposed to explain the capsid structure, in which capsid monomers form a hexagonal lattice, which according to Euler's Theorem can be made into a closed surface by the inclusion of exactly twelve pentagonal "defects" (Figure 1-5) [91, 98]. Fullerene cones will vary in shape according to the positions of the pentons; a cone will have between one and five pentons near its small end, and the others at the large end (six would produce a rod). More aberrant shapes may be produced if some pentons are near the middle. A prediction of this model is that the angles of cone-shaped capsids will be quantized into five values depending on their arrangement of

pentons, with the most commonly observed 5,7 cone having an angle of 19.2°. Electron microscopy of HIV cores shows a Gaussian distribution of cone angles roughly centered on this value [53, 99, 100]. However, those measurements were made on projections, which can be misleading since the cone angle will appear greater if the viewing axis is not perpendicular to the cone's axis of rotational symmetry.

Maturation Switches

Three distinct structural switches have been identified in HIV maturation. The best characterized of these is the N-terminal β -hairpin structure formed after cleavage of the CA NTD from MA [81]. The β -hairpin appears to play a role in stabilizing capsid tubes and cones, but mutations in the corresponding region have little effect on viral assembly or budding. Indeed, mutational analysis shows that the NTD as a whole is important for formation of mature capsid cores, but much less important for the formation of immature particles or spherical CA assemblies [74, 82, 101-104].

The second involves matrix protein, which had been observed to have lower affinity for the membrane once cleaved from Gag than in the polyprotein. NMR studies then showed that MA exists in two states: a trimer in which the myristyl group is fully exposed, and a monomer with the myristyl group partially retracted [105-107]. The mechanism is postulated to be an entropic change in equilibrium, rather than a gross conformational change. By coupling MA oligomerization and membrane binding, this also allows the localization of MA to be regulated by NC RNA binding and Gag proteolysis. It is not yet clear whether MA fully dissociates from the plasma membrane upon Gag proteolysis, however, as the high local concentration of MA could still promote oligomerization and thus stabilize membrane binding.

The 14-residue SP1 spacer peptide has been shown to be crucially important for viral particle assembly *in vivo*, and the formation of CA spheres *in vitro* [72, 74, 88, 101-103, 108]. Mutation of the cleavage site between CA and SP1 results in assembly and budding of particles that fail to undergo the maturation process and instead form a somewhat spherical CA layer separate from the membrane/MA [45]. One study found that CA-SP1 could form tubes *in vitro*, although only at high pH and salt concentration [34]. Taken together, these results indicate that SP1 may serve to stabilize the spherical, immature form of the CA lattice, and therefore to help facilitate the proteolytic regulation of the maturation process. It was computationally predicted that SP1 could form an α -helix, and insertion of helix-breaking residues into the region caused defects in particle assembly [88]. Mutation of residues H359, K360, A361, L364, A367, and M368 resulted in impaired virus production both in the presence and absence of PR, and also eliminated Gag multimerization as assayed by ultracentrifugation [109, 110]. The predicted α -helical region was disordered in the crystal structure [85] and an NMR study of the CA CTD-SP1-NC domains showed a small α -helical propensity, but did not find a significant difference in the dimerization affinity relative to CA alone [111]. However, it is not known whether those results can be extrapolated to the physiological case, in which the full length Gag molecule is present along with RNA. A synthetic peptide composed of SP1 along with 21 residues at its N-terminus and 13 residues at its C-terminus was found to form an amphipathic α -helix in 30% trifluoroethanol by NMR [112]. Gel filtration indicated that the peptide had a tendency to aggregate, but it appeared to form dimers as well. Additionally, the authors found that SP1 promotes RNA binding by NC-p7 and showed by molecular dynamics simulations that both dimers and trimers would be

avored by the peptide. This is intriguing in light of the important structural role played by RNA in HIV assembly.

Cryoelectron Tomography

Although X-ray crystallography and electron microscopic single particle analysis methods have been used to solve the structures of many viruses with great success, HIV presents unusual challenges. Since each HIV particle is structurally unique and lacking any global symmetry, techniques based on averaging of whole particles or icosahedrally symmetric unit cells cannot be employed.

Cryoelectron tomography is an ideal method with which to answer many of the remaining structural questions about the virus. The native structure of the sample is preserved down to the conformations of macromolecules, and the resulting images represent the actual electron density of the sample. Electron tomography can obtain three-dimensional information about structurally authentic virus-like particles by recording a series of images with the sample incrementally tilted around an axis perpendicular to the beam [113]. These views can then be used to reconstruct the three-dimensional density of the original sample through weighted backprojection. According to the dose fractionation theorem, a given electron dose spread out over a tilt series will yield the same resolution in three dimensions as it would have in a two-dimensional projection, as long as the dose for each image in the tilt series is sufficient for alignment [114]. In general, the resolution of a tomogram will depend on the tilt increments and range, sample thickness, alignment accuracy, and signal-to-noise ratio of images, which is itself fundamentally limited by the electron dose [115, 116]. Electron tomography has been used with great success to study

the internal structures of other viruses lacking global symmetry [117] and surface proteins on retroviruses including HIV [118-120].

Personal Contributions

In chapter 2, I present the results of a study of mature HIV-1 virus-like particles. This project was intended to catalog the three-dimensional morphologies of viral cores *in vivo*, measure the cone angles in three dimensions in order to test the fullerene cone model, and to make other structural observations as they became possible. I began working on that project as soon as the lab was running, and through the time that the resulting paper was published I was the only person in the Jensen lab primarily working on HIV. I traveled to Dr. Sundquist's lab in Utah along with Drs. Jensen and Tivol, where the three of us collaborated in freezing the virus-like particles as they were produced and purified by Dr. Ganser-Pornillos (then a graduate student in the Sundquist lab). Drs. Jensen and Tivol also assisted in the microscopy. I performed all of the tomographic reconstructions and did all of the subsequent computational analysis. This included segmentation using Amira (Mercury Computer Systems, Inc., San Diego CA), development of all custom modules in Amira using the C++ programming language, creating scripts to make measurements and generate figures, and final preparation of all figures except for 2-1 and 2-4, which were assembled by Dr. Jensen. In the course of that project, I assisted in the evaluation of the flip-flop cryostage and dual axis tomography system, resulting in my contribution of Figure A-3 to Appendix A.

In chapter 3, I present our results from the study of immature HIV-1 virions. (We considered these to be virions, albeit noninfectious, because they contained all structural proteins including Env. This was in contrast to the mature particles, which lacked Env as

well as functional copies of RT.) Improvements to our experience with the microscope, along with a better CCD camera, allowed substantial increase in the quality of images for this study. That project was carried out in collaboration with Dr. Elizabeth Wright. My involvement in the particle freezing, microscopy, and tomographic reconstructions was shared equally with Dr. Wright. I wrote all the Amira modules used in the project, including the generation of spherical shells, projection of density onto a surface (this was later modified by Dr. H. Jane Ding into the version used for most of the analysis), location of density extrema, classification of local order, computation of Voronoi cells around each unit cell, Voronoi partitioned radial averaging (but Dr. Ding wrote the initial version of the radial averaging module), and unit cell alignment and averaging. I carried out the averaging of the Gag unit cells and manual docking of crystal structures. Dr. Wright wrote the majority of the first draft of the paper, while I wrote the text dealing with our computational analysis and also revised the rest of it. Dr. Wright prepared Figures 3-1, 3-2, 3-4, and 3-5, and I prepared the others.

References

1. UNAIDS, *AIDS epidemic update: December 2005*. 2005, Geneva, Switzerland: UNAIDS.
2. Coffin, J.M., S.H. Hughes, and H. Varmus, *Retroviruses*. 1997, Plainview, N.Y.: Cold Spring Harbor Laboratory Press. xv, 843 p.
3. Turner, B.G. and M.F. Summers, *Structural biology of HIV*. J Mol Biol, 1999. **285**(1): p. 1-32.

4. Parkin, N.T., M. Chamorro, and H.E. Varmus, *Human immunodeficiency virus type 1 gag-pol frameshifting is dependent on downstream mRNA secondary structure: demonstration by expression in vivo*. J Virol, 1992. **66**(8): p. 5147-51.
5. Jacks, T., et al., *Characterization of ribosomal frameshifting in HIV-1 gag-pol expression*. Nature, 1988. **331**(6153): p. 280-3.
6. Franzusoff, A., et al., *Biochemical and genetic definition of the cellular protease required for HIV-1 gp160 processing*. J Biol Chem, 1995. **270**(7): p. 3154-9.
7. Decroly, E., et al., *Identification of the paired basic convertases implicated in HIV gp160 processing based on in vitro assays and expression in CD4(+) cell lines*. J Biol Chem, 1996. **271**(48): p. 30442-50.
8. Taylor, N.A., W.J. Van De Ven, and J.W. Creemers, *Curbing activation: proprotein convertases in homeostasis and pathology*. FASEB J, 2003. **17**(10): p. 1215-27.
9. Moore, J.P., et al., *The CCR5 and CXCR4 coreceptors--central to understanding the transmission and pathogenesis of human immunodeficiency virus type 1 infection*. AIDS Res Hum Retroviruses, 2004. **20**(1): p. 111-26.
10. Rein, A.L., et al., *A replication-defective variant of Moloney murine leukemia virus. I. Biological characterization*. J Virol, 1978. **25**(1): p. 146-56.
11. Andreadis, S.T. and J.R. Morgan, *Quantitative measurement of the concentration of active recombinant retrovirus*. Methods Mol Med, 2002. **69**: p. 161-72.
12. Andreadis, S., et al., *Toward a more accurate quantitation of the activity of recombinant retroviruses: alternatives to titer and multiplicity of infection*. J Virol, 2000. **74**(7): p. 3431-9.

13. Kwon, Y.J., et al., *Determination of infectious retrovirus concentration from colony-forming assay with quantitative analysis*. J Virol, 2003. **77**(10): p. 5712-20.
14. Bukrinskaya, A., et al., *Establishment of a functional human immunodeficiency virus type 1 (HIV-1) reverse transcription complex involves the cytoskeleton*. J Exp Med, 1998. **188**(11): p. 2113-25.
15. Campbell, E.M., R. Nunez, and T.J. Hope, *Disruption of the actin cytoskeleton can complement the ability of Nef to enhance human immunodeficiency virus type 1 infectivity*. J Virol, 2004. **78**(11): p. 5745-55.
16. Lehmann-Che, J. and A. Saib, *Early stages of HIV replication: how to hijack cellular functions for a successful infection*. AIDS Rev, 2004. **6**(4): p. 199-207.
17. McDonald, D., et al., *Visualization of the intracellular behavior of HIV in living cells*. J Cell Biol, 2002. **159**(3): p. 441-52.
18. de Soultrait, V.R., et al., *HIV-1 integrase interacts with yeast microtubule-associated proteins*. Biochim Biophys Acta, 2002. **1575**(1-3): p. 40-8.
19. Auewarakul, P., et al., *Uncoating of HIV-1 requires cellular activation*. Virology, 2005. **337**(1): p. 93-101.
20. Miller, M.D., C.M. Farnet, and F.D. Bushman, *Human immunodeficiency virus type 1 preintegration complexes: studies of organization and composition*. J Virol, 1997. **71**(7): p. 5382-90.
21. Dismuke, D.J. and C. Aiken, *Evidence for a functional link between uncoating of the human immunodeficiency virus type 1 core and nuclear import of the viral preintegration complex*. J Virol, 2006. **80**(8): p. 3712-20.

22. Nermut, M.V. and A. Fassati, *Structural analyses of purified human immunodeficiency virus type 1 intracellular reverse transcription complexes*. J Virol, 2003. **77**(15): p. 8196-206.
23. Fassati, A. and S.P. Goff, *Characterization of intracellular reverse transcription complexes of human immunodeficiency virus type 1*. J Virol, 2001. **75**(8): p. 3626-35.
24. Buck, C.B., et al., *The human immunodeficiency virus type 1 gag gene encodes an internal ribosome entry site*. J Virol, 2001. **75**(1): p. 181-91.
25. Muriaux, D., et al., *RNA is a structural element in retrovirus particles*. Proc Natl Acad Sci USA, 2001. **98**(9): p. 5246-51.
26. Dorfman, T., et al., *Mapping of functionally important residues of a cysteine-histidine box in the human immunodeficiency virus type 1 nucleocapsid protein*. J Virol, 1993. **67**(10): p. 6159-69.
27. Zhang, Y., et al., *Analysis of the assembly function of the human immunodeficiency virus type 1 gag protein nucleocapsid domain*. J Virol, 1998. **72**(3): p. 1782-9.
28. Zhang, Y. and E. Barklis, *Effects of nucleocapsid mutations on human immunodeficiency virus assembly and RNA encapsidation*. J Virol, 1997. **71**(9): p. 6765-76.
29. D'Souza, V. and M.F. Summers, *How retroviruses select their genomes*. Nat Rev Microbiol, 2005. **3**(8): p. 643-55.
30. Sakuragi, J., T. Shioda, and A.T. Panganiban, *Duplication of the primary encapsidation and dimer linkage region of human immunodeficiency virus type 1*

- RNA results in the appearance of monomeric RNA in virions.* J Virol, 2001. **75**(6): p. 2557-65.
31. Sakuragi, J., et al., *Possible role of dimerization in human immunodeficiency virus type 1 genome RNA packaging.* J Virol, 2003. **77**(7): p. 4060-9.
 32. Sakuragi, J., A. Iwamoto, and T. Shioda, *Dissociation of genome dimerization from packaging functions and virion maturation of human immunodeficiency virus type 1.* J Virol, 2002. **76**(3): p. 959-67.
 33. Campbell, S. and A. Rein, *In vitro assembly properties of human immunodeficiency virus type 1 Gag protein lacking the p6 domain.* J Virol, 1999. **73**(3): p. 2270-9.
 34. Gross, I., H. Hohenberg, and H.G. Krausslich, *In vitro assembly properties of purified bacterially expressed capsid proteins of human immunodeficiency virus.* Eur J Biochem, 1997. **249**(2): p. 592-600.
 35. Briggs, J.A., et al., *The stoichiometry of Gag protein in HIV-1.* Nat Struct Mol Biol, 2004. **11**(7): p. 672-5.
 36. Stuchell, M.D., et al., *The human endosomal sorting complex required for transport (ESCRT-I) and its role in HIV-1 budding.* J Biol Chem, 2004. **279**(34): p. 36059-71.
 37. von Schwedler, U.K., et al., *The protein network of HIV budding.* Cell, 2003. **114**(6): p. 701-13.
 38. Freed, E.O., *The HIV-TSG101 interface: recent advances in a budding field.* Trends Microbiol, 2003. **11**(2): p. 56-9.

39. Demirov, D.G., et al., *Overexpression of the N-terminal domain of TSG101 inhibits HIV-1 budding by blocking late domain function*. Proc Natl Acad Sci USA, 2002. **99**(2): p. 955-60.
40. Martin-Serrano, J., T. Zang, and P.D. Bieniasz, *HIV-1 and Ebola virus encode small peptide motifs that recruit Tsg101 to sites of particle assembly to facilitate egress*. Nat Med, 2001. **7**(12): p. 1313-9.
41. Katzmann, D.J., M. Babst, and S.D. Emr, *Ubiquitin-dependent sorting into the multivesicular body pathway requires the function of a conserved endosomal protein sorting complex, ESCRT-I*. Cell, 2001. **106**(2): p. 145-55.
42. Sundquist, W.I., et al., *Ubiquitin recognition by the human TSG101 protein*. Mol Cell, 2004. **13**(6): p. 783-9.
43. Pornillos, O., et al., *Structure and functional interactions of the Tsg101 UEV domain*. EMBO J, 2002. **21**(10): p. 2397-406.
44. Pornillos, O., et al., *Structure of the Tsg101 UEV domain in complex with the PTAP motif of the HIV-1 p6 protein*. Nat Struct Biol, 2002. **9**(11): p. 812-7.
45. Wiegers, K., et al., *Sequential steps in human immunodeficiency virus particle maturation revealed by alterations of individual Gag polyprotein cleavage sites*. J Virol, 1998. **72**(4): p. 2846-54.
46. Wilk, T., et al., *Organization of immature human immunodeficiency virus type 1*. J Virol, 2001. **75**(2): p. 759-71.
47. Briggs, J.A., et al., *Cryo-electron microscopy reveals conserved and divergent features of gag packing in immature particles of Rous sarcoma virus and human immunodeficiency virus*. J Mol Biol, 2006. **355**(1): p. 157-68.

48. Fuller, S.D., et al., *Cryo-electron microscopy reveals ordered domains in the immature HIV-1 particle*. *Curr Biol*, 1997. **7**(10): p. 729-38.
49. Nermut, M.V., et al., *Further evidence for hexagonal organization of HIV gag protein in prebudding assemblies and immature virus-like particles*. *J Struct Biol*, 1998. **123**(2): p. 143-9.
50. Ohagen, A., et al., *The morphology of the immature HIV-1 virion*. *Virology*, 1997. **228**(1): p. 112-4.
51. Nermut, M.V., et al., *Further evidence of icosahedral symmetry in human and simian immunodeficiency virus*. *AIDS Res Hum Retroviruses*, 1993. **9**(10): p. 929-38.
52. Yeager, M., et al., *Supramolecular organization of immature and mature murine leukemia virus revealed by electron cryo-microscopy: implications for retroviral assembly mechanisms*. *Proc Natl Acad Sci USA*, 1998. **95**(13): p. 7299-304.
53. Briggs, J.A., et al., *Structural organization of authentic, mature HIV-1 virions and cores*. *EMBO J*, 2003. **22**(7): p. 1707-15.
54. Lanman, J., et al., *Identification of novel interactions in HIV-1 capsid protein assembly by high-resolution mass spectrometry*. *J Mol Biol*, 2003. **325**(4): p. 759-72.
55. Lanman, J., et al., *Key interactions in HIV-1 maturation identified by hydrogen-deuterium exchange*. *Nat Struct Mol Biol*, 2004. **11**(7): p. 676-7.
56. Krausslich, H.G., et al., *Processing of in vitro-synthesized gag precursor proteins of human immunodeficiency virus (HIV) type 1 by HIV proteinase generated in Escherichia coli*. *J Virol*, 1988. **62**(11): p. 4393-7.

57. Pettit, S.C., et al., *Processing sites in the human immunodeficiency virus type 1 (HIV-1) Gag-Pro-Pol precursor are cleaved by the viral protease at different rates*. *Retrovirology*, 2005. **2**: p. 66.
58. Loeb, D.D., et al., *Complete mutagenesis of the HIV-1 protease*. *Nature*, 1989. **340**(6232): p. 397-400.
59. Pettit, S.C., et al., *The dimer interfaces of protease and extra-protease domains influence the activation of protease and the specificity of GagPol cleavage*. *J Virol*, 2003. **77**(1): p. 366-74.
60. Pettit, S.C., et al., *Initial cleavage of the human immunodeficiency virus type 1 GagPol precursor by its activated protease occurs by an intramolecular mechanism*. *J Virol*, 2004. **78**(16): p. 8477-85.
61. Pettit, S.C., et al., *Ordered processing of the human immunodeficiency virus type 1 GagPol precursor is influenced by the context of the embedded viral protease*. *J Virol*, 2005. **79**(16): p. 10601-7.
62. Kaplan, A.H. and R. Swanstrom, *Human immunodeficiency virus type 1 Gag proteins are processed in two cellular compartments*. *Proc Natl Acad Sci USA*, 1991. **88**(10): p. 4528-32.
63. Kaplan, A.H., M. Manchester, and R. Swanstrom, *The activity of the protease of human immunodeficiency virus type 1 is initiated at the membrane of infected cells before the release of viral proteins and is required for release to occur with maximum efficiency*. *J Virol*, 1994. **68**(10): p. 6782-6.

64. Krausslich, H.G., *Specific inhibitor of human immunodeficiency virus proteinase prevents the cytotoxic effects of a single-chain proteinase dimer and restores particle formation.* J Virol, 1992. **66**(1): p. 567-72.
65. Krausslich, H.G., *Human immunodeficiency virus proteinase dimer as component of the viral polyprotein prevents particle assembly and viral infectivity.* Proc Natl Acad Sci USA, 1991. **88**(8): p. 3213-7.
66. Humphrey, R.W., et al., *Removal of human immunodeficiency virus type 1 (HIV-1) protease inhibitors from preparations of immature HIV-1 virions does not result in an increase in infectivity or the appearance of mature morphology.* Antimicrob Agents Chemother, 1997. **41**(5): p. 1017-23.
67. Rao, Z., et al., *Crystal structure of SIV matrix antigen and implications for virus assembly.* Nature, 1995. **378**(6558): p. 743-7.
68. Hill, C.P., et al., *Crystal structures of the trimeric human immunodeficiency virus type 1 matrix protein: implications for membrane association and assembly.* Proc Natl Acad Sci USA, 1996. **93**(7): p. 3099-104.
69. Conte, M.R. and S. Matthews, *Retroviral matrix proteins: a structural perspective.* Virology, 1998. **246**(2): p. 191-8.
70. Wilk, T. and S.D. Fuller, *Towards the structure of the human immunodeficiency virus: divide and conquer.* Curr Opin Struct Biol, 1999. **9**(2): p. 231-43.
71. Forster, M.J., B. Mulloy, and M.V. Nermut, *Molecular modelling study of HIV p17gag (MA) protein shell utilising data from electron microscopy and X-ray crystallography.* J Mol Biol, 2000. **298**(5): p. 841-57.

72. Borsetti, A., A. Ohagen, and H.G. Gottlinger, *The C-terminal half of the human immunodeficiency virus type 1 Gag precursor is sufficient for efficient particle assembly*. J Virol, 1998. **72**(11): p. 9313-7.
73. Lee, P.P. and M.L. Linial, *Efficient particle formation can occur if the matrix domain of human immunodeficiency virus type 1 Gag is substituted by a myristylation signal*. J Virol, 1994. **68**(10): p. 6644-54.
74. Accola, M.A., B. Strack, and H.G. Gottlinger, *Efficient particle production by minimal Gag constructs which retain the carboxy-terminal domain of human immunodeficiency virus type 1 capsid-p2 and a late assembly domain*. J Virol, 2000. **74**(12): p. 5395-402.
75. Reil, H., et al., *Efficient HIV-1 replication can occur in the absence of the viral matrix protein*. EMBO J, 1998. **17**(9): p. 2699-708.
76. Gitti, R.K., et al., *Structure of the amino-terminal core domain of the HIV-1 capsid protein*. Science, 1996. **273**(5272): p. 231-5.
77. Gamble, T.R., et al., *Structure of the carboxyl-terminal dimerization domain of the HIV-1 capsid protein*. Science, 1997. **278**(5339): p. 849-53.
78. Berthet-Colominas, C., et al., *Head-to-tail dimers and interdomain flexibility revealed by the crystal structure of HIV-1 capsid protein (p24) complexed with a monoclonal antibody Fab*. EMBO J, 1999. **18**(5): p. 1124-36.
79. Gamble, T.R., et al., *Crystal structure of human cyclophilin A bound to the amino-terminal domain of HIV-1 capsid*. Cell, 1996. **87**(7): p. 1285-94.
80. Momany, C., et al., *Crystal structure of dimeric HIV-1 capsid protein*. Nat Struct Biol, 1996. **3**(9): p. 763-70.

81. von Schwedler, U.K., et al., *Proteolytic refolding of the HIV-1 capsid protein amino-terminus facilitates viral core assembly*. EMBO J, 1998. **17**(6): p. 1555-68.
82. Gross, I., et al., *N-Terminal extension of human immunodeficiency virus capsid protein converts the in vitro assembly phenotype from tubular to spherical particles*. J Virol, 1998. **72**(6): p. 4798-810.
83. Tang, C., Y. Ndassa, and M.F. Summers, *Structure of the N-terminal 283-residue fragment of the immature HIV-1 Gag polyprotein*. Nat Struct Biol, 2002. **9**(7): p. 537-43.
84. Mortuza, G.B., et al., *High-resolution structure of a retroviral capsid hexameric amino-terminal domain*. Nature, 2004. **431**(7007): p. 481-5.
85. Worthylake, D.K., et al., *Structures of the HIV-1 capsid protein dimerization domain at 2.6 Å resolution*. Acta Crystallogr D Biol Crystallogr, 1999. **55 (Pt 1)**: p. 85-92.
86. Dorfman, T., et al., *Functional domains of the capsid protein of human immunodeficiency virus type 1*. J Virol, 1994. **68**(12): p. 8180-7.
87. Mammano, F., et al., *Role of the major homology region of human immunodeficiency virus type 1 in virion morphogenesis*. J Virol, 1994. **68**(8): p. 4927-36.
88. Accola, M.A., S. Hoglund, and H.G. Gottlinger, *A putative alpha-helical structure which overlaps the capsid-p2 boundary in the human immunodeficiency virus type 1 Gag precursor is crucial for viral particle assembly*. J Virol, 1998. **72**(3): p. 2072-8.

89. Ivanov, D., et al., *Mammalian SCAN domain dimer is a domain-swapped homolog of the HIV capsid C-terminal domain*. Mol Cell, 2005. **17**(1): p. 137-43.
90. Ehrlich, L.S., B.E. Agresta, and C.A. Carter, *Assembly of recombinant human immunodeficiency virus type 1 capsid protein in vitro*. J Virol, 1992. **66**(8): p. 4874-83.
91. Ganser, B.K., et al., *Assembly and analysis of conical models for the HIV-1 core*. Science, 1999. **283**(5398): p. 80-3.
92. Li, S., et al., *Image reconstructions of helical assemblies of the HIV-1 CA protein*. Nature, 2000. **407**(6802): p. 409-13.
93. Ehrlich, L.S., et al., *HIV-1 capsid protein forms spherical (immature-like) and tubular (mature-like) particles in vitro: structure switching by pH-induced conformational changes*. Biophys J, 2001. **81**(1): p. 586-94.
94. Ganser, B.K., et al., *Three-dimensional structure of the M-MuLV CA protein on a lipid monolayer: a general model for retroviral capsid assembly*. EMBO J, 2003. **22**(12): p. 2886-92.
95. Barklis, E., et al., *Organization of HIV-1 capsid proteins on a lipid monolayer*. J Biol Chem, 1998. **273**(13): p. 7177-80.
96. Mayo, K., et al., *Retrovirus capsid protein assembly arrangements*. J Mol Biol, 2003. **325**(1): p. 225-37.
97. Huseby, D., et al., *Assembly of human immunodeficiency virus precursor gag proteins*. J Biol Chem, 2005. **280**(18): p. 17664-70.
98. Thurston, W.P., *Shapes of polyhedra and triangulations of the sphere*. Geometry & Topology Monographs, 1998. **1**: p. 511-549.

99. Welker, R., et al., *Biochemical and structural analysis of isolated mature cores of human immunodeficiency virus type 1*. J Virol, 2000. **74**(3): p. 1168-77.
100. Accola, M.A., A. Ohagen, and H.G. Gottlinger, *Isolation of human immunodeficiency virus type 1 cores: retention of Vpr in the absence of p6(gag)*. J Virol, 2000. **74**(13): p. 6198-202.
101. Gross, I., et al., *A conformational switch controlling HIV-1 morphogenesis*. EMBO J, 2000. **19**(1): p. 103-13.
102. Ganser-Pornillos, B.K., et al., *Assembly properties of the human immunodeficiency virus type 1 CA protein*. J Virol, 2004. **78**(5): p. 2545-52.
103. Von Schwedler, U.K., et al., *Functional surfaces of the human immunodeficiency virus type 1 capsid protein*. J Virol, 2003. **77**(9): p. 5439-50.
104. Forshey, B.M., et al., *Formation of a human immunodeficiency virus type 1 core of optimal stability is crucial for viral replication*. J Virol, 2002. **76**(11): p. 5667-77.
105. Tang, C., et al., *Entropic switch regulates myristate exposure in the HIV-1 matrix protein*. Proc Natl Acad Sci USA, 2004. **101**(2): p. 517-22.
106. Zhou, W. and M.D. Resh, *Differential membrane binding of the human immunodeficiency virus type 1 matrix protein*. J Virol, 1996. **70**(12): p. 8540-8.
107. Hermida-Matsumoto, L. and M.D. Resh, *Human immunodeficiency virus type 1 protease triggers a myristoyl switch that modulates membrane binding of Pr55(gag) and p17MA*. J Virol, 1999. **73**(3): p. 1902-8.

108. Krausslich, H.G., et al., *The spacer peptide between human immunodeficiency virus capsid and nucleocapsid proteins is essential for ordered assembly and viral infectivity*. J Virol, 1995. **69**(6): p. 3407-19.
109. Liang, C., et al., *Characterization of a putative alpha-helix across the capsid-SP1 boundary that is critical for the multimerization of human immunodeficiency virus type 1 gag*. J Virol, 2002. **76**(22): p. 11729-37.
110. Liang, C., et al., *A structurally disordered region at the C terminus of capsid plays essential roles in multimerization and membrane binding of the gag protein of human immunodeficiency virus type 1*. J Virol, 2003. **77**(3): p. 1772-83.
111. Newman, J.L., et al., *Flexibility in the P2 domain of the HIV-1 Gag polyprotein*. Protein Sci, 2004. **13**(8): p. 2101-7.
112. Morellet, N., et al., *Helical structure determined by NMR of the HIV-1 (345-392)Gag sequence, surrounding p2: implications for particle assembly and RNA packaging*. Protein Sci, 2005. **14**(2): p. 375-86.
113. Lucic, V., F. Forster, and W. Baumeister, *Structural studies by electron tomography: from cells to molecules*. Annu Rev Biochem, 2005. **74**: p. 833-65.
114. McEwen, B.F., K.H. Downing, and R.M. Glaeser, *The relevance of dose-fractionation in tomography of radiation-sensitive specimens*. Ultramicroscopy, 1995. **60**(3): p. 357-73.
115. Grimm, R., et al., *Electron tomography of ice-embedded prokaryotic cells*. Biophys J, 1998. **74**(2 Pt 1): p. 1031-42.
116. Jensen, G.J., *Alignment error envelopes for single particle analysis*. J Struct Biol, 2001. **133**(2-3): p. 143-55.

117. Cyrklaff, M., et al., *Cryo-electron tomography of vaccinia virus*. Proc Natl Acad Sci USA, 2005. **102**(8): p. 2772-7.
118. Forster, F., et al., *Retrovirus envelope protein complex structure in situ studied by cryo-electron tomography*. Proc Natl Acad Sci USA, 2005. **102**(13): p. 4729-34.
119. Zhu, P., et al., *Electron tomography analysis of envelope glycoprotein trimers on HIV and simian immunodeficiency virus virions*. Proc Natl Acad Sci USA, 2003. **100**(26): p. 15812-7.
120. Zhu, P., et al., *Distribution and three-dimensional structure of AIDS virus envelope spikes*. Nature, 2006.

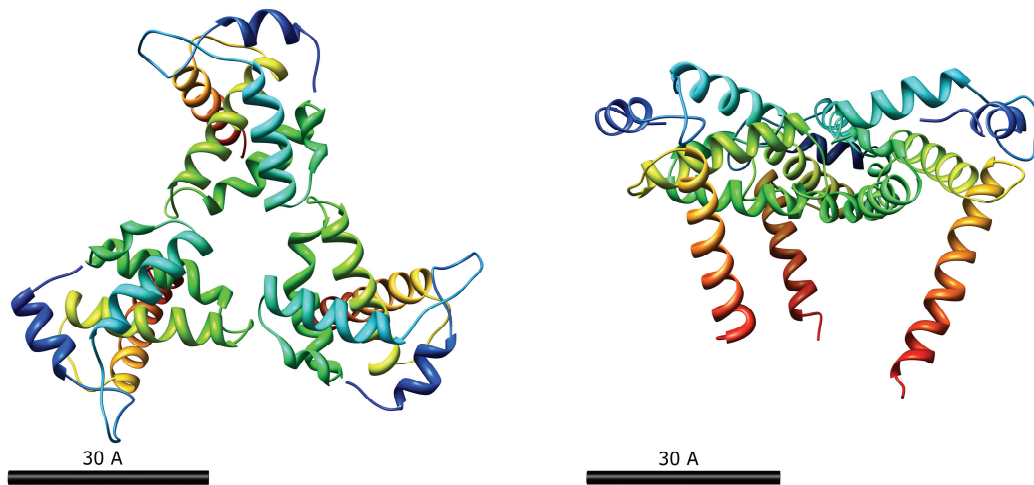
Figures

Figure 1-1. Matrix protein trimer.

From PDB 1HIW. Amino termini are in blue, carboxy termini in red.

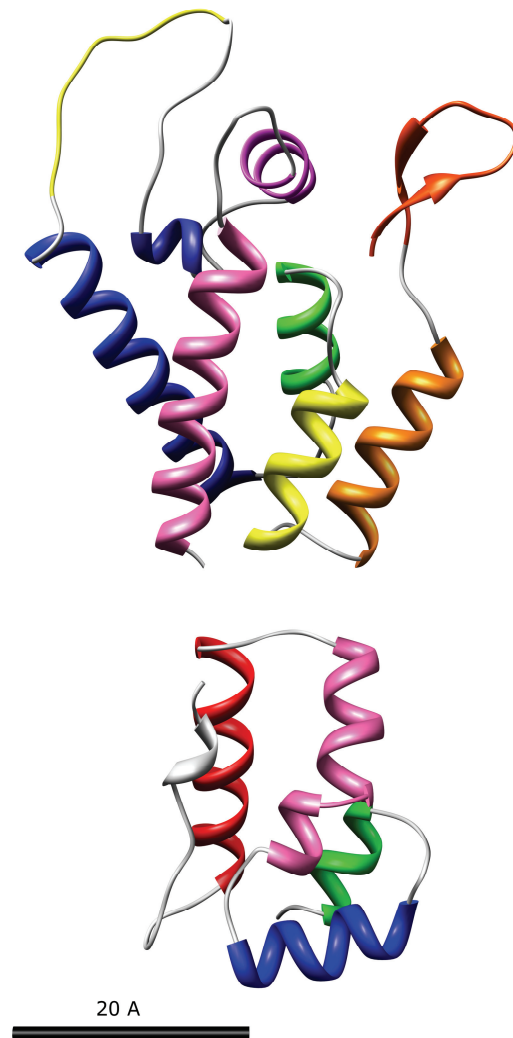


Figure 1-2. Capsid amino and carboxy terminal domains.

From PDB 1AK4 and 1A43. Colors are after original publications (NTD: β -hairpin, red orange; helix 1, orange; helix 2, yellow; helix 3, green; helix 4, blue; cyclophilin A binding loop, yellow; helix 5, dark blue; helix 6, magenta; helix 7, pink; CTD: helix 1, red; helix 2, pink; helix 3, blue; helix 4, green).

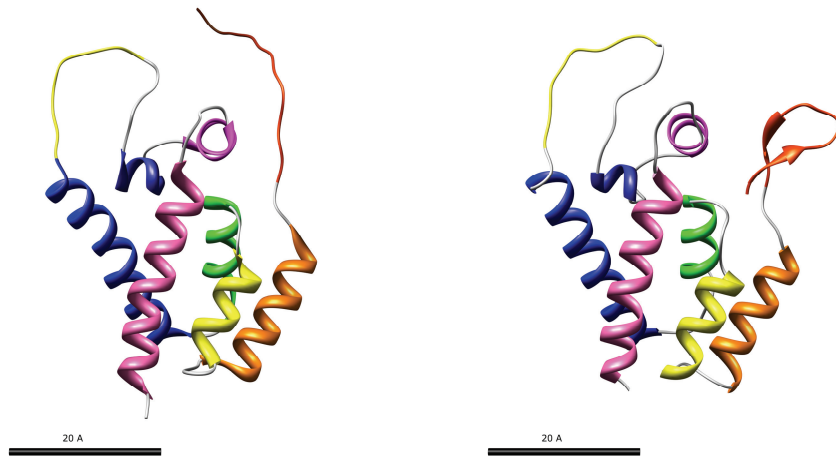


Figure 1-3. Capsid NTD maturation.

Left: Immature. From PDB 1L6N.

Right: Mature. From PDB 1AK4.

Colors as in Figure 1-2.

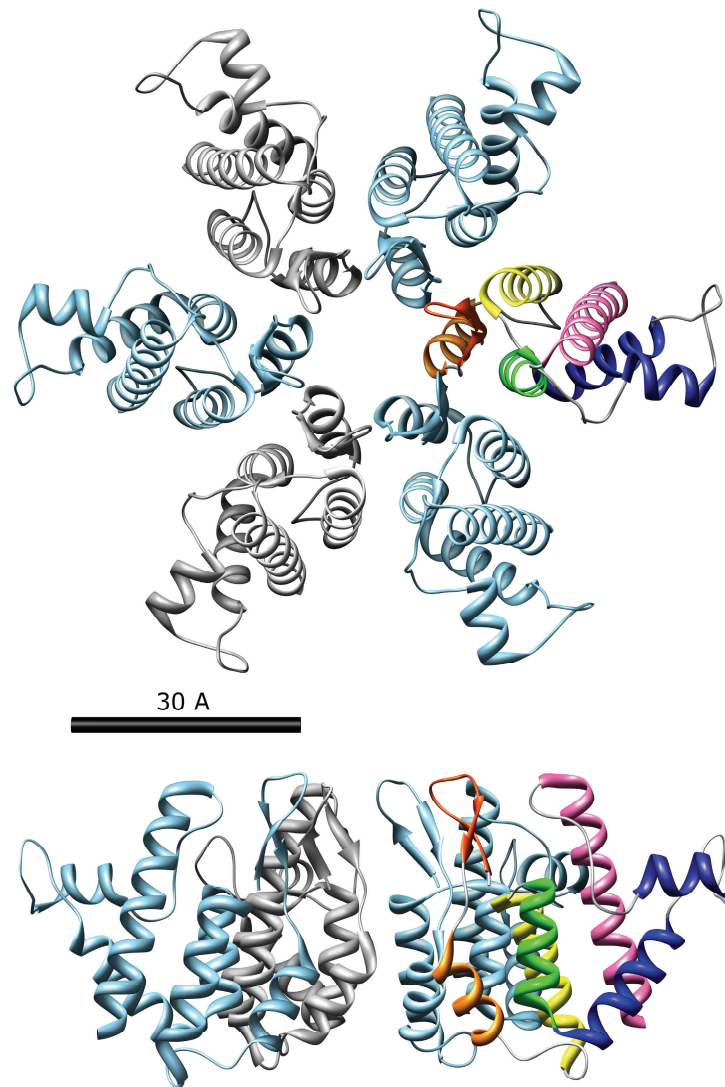


Figure 1-4. N-MLV capsid NTD hexamer.

From PDB 1U7K.

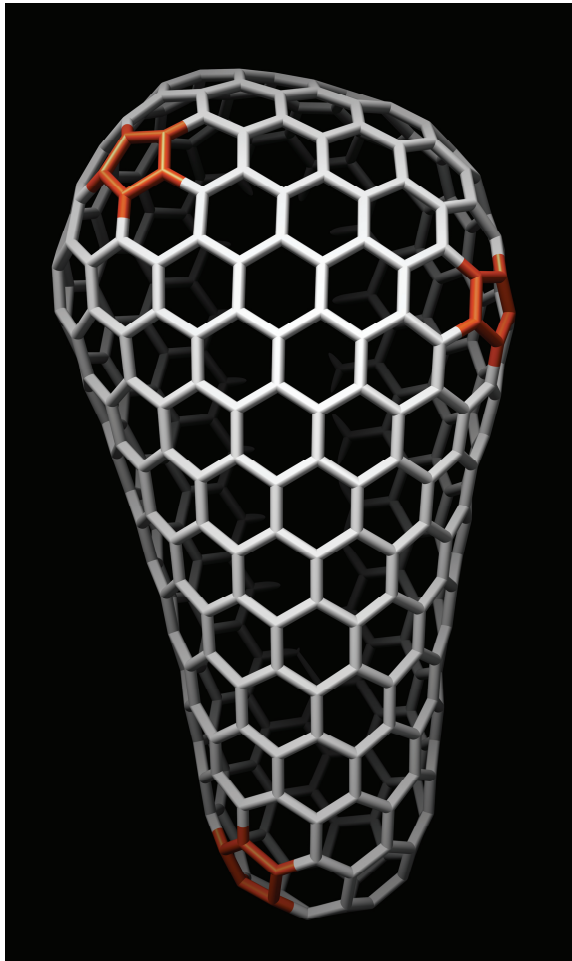


Figure 1-5. Fullerene cone model.

Three penton defects are highlighted in orange. Model courtesy of Dr. Barbie Ganser-Pornillos.

Chapter 2: Three-dimensional structure of HIV-1 virus-like particles by electron cryotomography

Jordan Benjamin¹, Barbie K. Ganser-Pornillos², William F. Tivol¹,
Wesley I. Sundquist³, Grant J. Jensen^{1*}

¹Division of Biology, California Institute of Technology, 1200 E. California Blvd.,
Pasadena, California, 91125

²Department of Cell Biology, The Scripps Research Institute, La Jolla, California, 92037

³Department of Biochemistry, University of Utah School of Medicine, 20 N, 1900 E, Salt
Lake City, Utah, 84132-3201

*Corresponding author, email address jensen@caltech.edu

Published in *Journal of Molecular Biology* 2005 Feb 18; 346(2):577–88

doi:10.1016/j.jmb.2004.11.064

Received 24 September 2004; revised 18 November 2004; accepted 23 November 2004.

Edited by M. F. Summers. Available online 8 December 2004.

Abstract

While the structures of nearly every HIV-1 protein are known in atomic detail from X-ray crystallography and NMR spectroscopy, many questions remain about how the individual proteins are arranged in the mature infectious viral particle. Here we report the three-dimensional structures of individual HIV-1 virus-like particles (VLPs) as obtained by electron cryotomography. These reconstructions revealed that while the structures and positions of the conical cores within each VLP were unique, they exhibited several surprisingly consistent features, including similarities in the size and shape of the wide end of the capsid (the “base”), uniform positioning of the base and other regions of the capsid 11 nm away from the envelope/MA layer, a cone angle that typically varied from 24° to 18° around the long axis of the cone, and an internal density (presumably part of the NC/RNA complex) cupped within the base. Multiple and nested capsids were also observed. These results support the fullerene cone model for the viral capsid, indicate that viral maturation involves a free re-organization of the capsid shell rather than a continuous condensation, imply that capsid assembly is both concentration- and template-driven, suggest that specific interactions exist between the capsid and the adjacent envelope/MA and NC/RNA layers, and show that a particular capsid shape is strongly favored *in vivo*.

Keywords

HIV, virus structure, tomography, electron cryomicroscopy, capsid

Introduction

While high-resolution structures of many viruses have now been determined by X-ray crystallography, such models will not be obtainable for the type 1 human immunodeficiency virus (HIV-1) because virions are individually unique. Instead, molecular models for HIV-1 must for now be obtained by combining high resolution structural studies of isolated viral components together with lower resolution reconstructions of intact virions generated by electron microscopy (EM). Thus our understanding of HIV-1 structure has advanced stepwise with the development and application of ever more sophisticated EM methods. After the virus was first identified in the early 1980s, its gross structure and organization were quickly characterized using the traditional EM techniques of thin sectioning and immuno- or negative staining (reviewed in^{1; 2}). Structural models of the mature virion have subsequently been refined using data from “cryo-” EM³, STEM⁴, and tomography^{5; 6}.

We now know that the mature HIV-1 virion has a roughly spherical outer lipid bilayer 120–200 nm in diameter³, which is studded with trimeric clusters of the transmembrane Env protein⁶. Inside the bilayer, there is a series of structural shells that organize the viral RNA genome and its associated enzymes for uncoating and replication in a new host cell. These different shells are assembled during the process of viral maturation, when the immature Gag polyprotein is proteolytically processed to produce the smaller MA, CA, and NC proteins (as well as several smaller peptides). The outermost shell of the mature virus (the “matrix”) is associated with the inner face of the bilayer and is composed of ~4000–5000 copies of the N-myristoylated MA protein. Inside the matrix is an unusual conical particle (the “core”), whose conical outer shell

(the “capsid”) is composed of ~1000–1500 copies of the viral CA protein. Within the capsid is a ribonucleoprotein (RNP) particle composed of two copies of the positive-sense RNA genome, thousands of copies of the RNA-binding NC protein, and ~250 copies each of the reverse transcriptase (RT) and integrase (IN) enzymes⁴.

High-resolution structural models are now available for essentially all of the HIV-1 proteins or their constituent domains, including MA, CA, and NC (reviewed in⁷). Moreover, molecular models for higher-order interactions within the viral matrix^{8; 9; 10} and capsid¹¹ lattices have been proposed based upon structural analyses of recombinant MA and CA protein assemblies. In the case of the capsid, EM analyses of helical and two-dimensional crystals of HIV-1 CA have revealed that the protein preferentially assembles into p6-based lattices composed of CA hexamers^{11; 12}. It has been proposed that the conical viral capsid assembles on a similar hexagonal CA net following the structural principles of a fullerene cone^{13; 14; 15; 16}. In the fullerene cone model, the body of the conical capsid is composed of CA hexamers, and the two ends of the cone are allowed to close through the introduction of pentameric defects, with five pentons at the narrow end and seven pentons at the wide end. The fullerene cone model correctly predicts the observed quantization of the cone angles of synthetic capsid assemblies¹⁵, and is also strongly supported by a series of cryo-EM measurements made on authentic viral cores³. However, all of these cone angle measurements were made with simple projection images, and this precluded a direct comparison of actual capsid cone angles to the quantized values predicted by the fullerene cone model because the authentic capsids could adopt variable orientations with the respect to the electron beam³ and because the

synthetic capsids were flattened and possibly distorted in other ways when dried onto carbon films¹⁵.

The recent development of electron cryotomography provides a new and more powerful way to investigate HIV-1 structure. This method offers the advantages inherent in cryoEM, in which a sample in solution is spread into a thin film across an EM grid and plunged into liquid ethane¹⁷. This procedure preserves the sample in a near-native, “frozen-hydrated” state, and allows the actual structure of the biological macromolecules to be imaged through their inherent contrast against an aqueous background. In tomography, a series of images is recorded of a specimen while it is tilted incrementally about some axis. Three-dimensional reconstructions of the specimen (“tomograms”) are then calculated by merging the images by back-projection in real space, or alternatively, by Fourier interpolation in reciprocal space. While the potential advantages of electron cryotomography have been discussed for decades, only in the past several years has it become practically feasible and effective through the advent of high quality CCD cameras, motorized and computer-controlled stages, programmable EMs, and development of automatic protocols to control specimen tracking, focusing, and exposures^{18; 19; 20}.

Two tomographic analyses of HIV particles have been reported previously, yielding information on the structure of the virion⁵ and on the shape and distribution of envelope glycoproteins on the virion surface⁶. Both of these studies, however, utilized negative staining procedures that limited the accurate visualization of internal core structures. Here, we report the first application of electron cryotomography to determine

the three-dimensional structure of several tens of individual, unfixed, unstained, whole HIV-1 virus-like particles (VLPs).

Results

Non-infectious HIV-1 VLPs were produced from a proviral expression construct with debilitating mutations in the RT and RNase H enzymes and a frameshift mutation that prevented Env protein expression. VLPs were produced in cultured human 293T cells, recovered from the supernatant, and purified by sucrose density centrifugation. As expected, the HIV-1 CA, MA, and NC proteins were the major protein components in the sample as analyzed by SDS-PAGE (data not shown).

HIV-1 VLPs were plunge-frozen onto EM grids and imaged in a 300 kV FEG TEM. A variety of particles was seen, including many VLPs with mature cores, a few immature VLPs with spherical Gag shells, and some “empty” vesicles without any visible core-like internal density (Figure 2-1 top). Energy filtered, dual-axis tilt series were recorded of 10 fields of VLPs at high defocus with the new “flip-flop” cryo-rotation stage, and three-dimensional reconstructions were calculated using the IMOD tomography package²¹ (Figure 2-1 middle). Inclusion of the second orthogonal tilt series improved the point-spread-function, as could be seen by the circular shape of the defocus fringe surrounding the gold fiducials in tomogram slices. Seventy-six mature VLPs were selected from the tomograms and denoised with nonlinear anisotropic diffusion²² (examples in Figure 2-1 bottom). Despite dual-axis data collection, there is still a “missing pyramid” of data in reciprocal space, which causes a loss of resolution in the direction parallel to the electron beam. Thus the shapes of the VLP capsids were best

resolved when they were oriented with their long axes “vertically” in the thin “horizontal” layer of ice. These approximately one-third (26) clearest capsids and their corresponding envelopes were segmented in three dimensions using a semi-automatic procedure guided by manually identified landmarks. While the majority of the surface of each capsid was clearly recognizable, especially across the long, straight edges, there were also some gaps arising presumably from noise, which in some unfavorable cases can actually be emphasized by the denoising algorithm. The structures of the capsid “tips” (narrow ends of the cones) were most difficult to detect, perhaps because their surfaces lay perpendicular to the electron beam (and are therefore smeared by the missing pyramid of data), but perhaps also because they are small and change abruptly. Following segmentation, the three principal axes of each segmented capsid were calculated so that the VLPs could be roughly aligned and compared.

Figure 2-2 shows a montage of all 26 segmented VLPs from the three orthogonal viewing directions. Of the 26, 16 exhibited the well-known conical capsid morphology. There were also several rod-shaped capsids as well as another class of pleiomorphic shapes that, while non-uniform, nevertheless presented corners, edges, and angles similar to those seen in the conical capsids. In addition, two VLPs contained multiple capsids: “3g” contained one conical and one rod-shaped capsid, and “1g” actually had a total of 5 capsids. Surprisingly, two VLPs (“10a” and “1g”) presented internal layers of density that appeared to be nested capsids, an organization that has not to our knowledge been reported previously (Figure 2-3). VLP envelopes were typically spheroidal with a mean largest diameter (the largest distance between any two points on the three-dimensional surface) of 143nm (standard deviation 10.8nm), but exhibited significant variability and

in many cases (VLPs “1k,” “6b,” “1n,” “2f,” “3j,” and “7g”) followed the contours of the capsid a consistent distance of 11 nm away (“peak-to-peak” distance from middle of lipid envelope/MA layer to middle of CA layer) for a significant portion of their surfaces.

Knowledge of the three-dimensional shapes of the envelope/matrix and capsid layers allowed us to measure volumes and surface areas accurately. The mean external surface areas were 49,000 nm² and 21,000 nm² (standard deviations 5,200 nm² and 9,000 nm²), respectively (Table 2-1). For this calculation, in those cases where VLPs presented multiple capsids (“10a,” “3g,” and “1g”), the surface areas of all the capsids were summed. The mean volumes of the VLPs and the conical cores were 980,000 nm³ and 190,000 nm³ (standard deviations 160,000 nm³ and 26,000 nm³), respectively. These small volumes imply that even single-copy proteins are present at appreciable concentrations (~9 μM) within viral cores, and that the concentrations of the viral RT and IN enzymes are quite high (~2 mM).

Previous studies have demonstrated that the virion diameter does not change upon maturation³. Thus, to calculate the number of MA subunits in the matrix shell, the packing was assumed to be identical to a recent model for the packing of Gag in the immature virus: hexagonal, with six monomers per unit cell and center-to-center spacings of 8.0 nm, observed 12.5 nm from the outside edge of the lipid bilayer⁴. We therefore contracted the boundaries of our segmented envelope/matrix layers by 12.5 nm normal to their surfaces at every point, and divided the contracted surface area by the presumed area per Gag monomer. For CA, we again assumed hexagonal packing, and used the measured center-to-center spacing of unit cells at the outside surface of 10.7 nm¹¹. The resulting averages of 4,000 and 1,300 monomers in the matrix and capsid shells agree

well with previous estimates⁴. This indicates that in general, only about one-third of the available CA protein is involved in an organized capsid layer. In the extreme case of the five-capsid VLP “1g,” however, 71% of the total CA protein was incorporated into a capsid layer.

When aligned and compared in three-dimensions, the majority class of capsids are more similar than suggested by the projection images found currently in the literature. Because the best current model for the organization of the capsid is a hexagonal net of CA protein arrayed following the principles of a fullerene cone¹⁵, the cone angle, which in theory should adopt only certain quantized values (19.2°, 38.9°, 60°, etc.), is of particular interest. We measured the cone angle for all the conical capsids rigorously in three-dimensional space by considering the intersection of the capsid’s surface with planes containing its primary principal axis. In other words, we measured the cone angle in sections through the capsid ranging 180° from “sagittal,” past “coronal,” and back to sagittal. For each section, the tip and base of the capsid were ignored, and lines were fit to the long edges by minimizing squared errors. These two lines defined a cone angle, which was plotted as a function of rotation angle around the long axis of the cone (Figure 2-4). The plots show a pattern of cone angle progression from ~24° to ~18°, which agrees well with the predicted 19°, since in fact any real 5,7 fullerene cone with finite unit cells cannot be perfectly symmetric. Although the measured angles varied by a few degrees depending on the precise boundaries used to exclude the tip and base of each capsid, the overall shape of each curve is insensitive to these parameters (data not shown). Most of the cones do tend to “flare” slightly (cone angle increases by a few degrees), however, towards their base. The observation that some capsids exhibit cone angles that appear

more “flattened,” and reach as much as 30°, is robust to perturbations of the procedure. For comparison, the corresponding cone angles from three idealized fullerene cone models^{11; 23} are also plotted in Figure 2-4 (black lines). The mean angle across all rotations for the 16 actual capsids measured was 20.1°. The mean angle across all rotations for the idealized fullerene cone models was exactly the same: 20.1°.

To compare the cores further and look for other conserved structural features, we averaged the VLP densities in three ways. First, guessing that important conserved structures within mature HIV-1 would be fixed with respect to the capsid, we aligned the VLPs by superposing their capsids’ principal axes as we had done before to measure cone angles, and calculated a three-dimensional average. Because the capsids vary in length, however, this produced confusing interferences. We next aligned the VLPs with respect to either the base or the tip of their capsids. Clear patterns in the resulting VLP averages then emerged (Figure 2-5). When bases were aligned, an inherent asymmetry became apparent in that their most distal points appeared to the side of their cone axes (panel 2-5B). The gross shape of the entire base was conserved, as was the 11 nm distance between the base of the capsid (green arrow in panel 2-5E) and the envelope/matrix layer (magenta arrow in panel 2-5E) surrounding it. When tips were aligned, the conserved cone angle and the same conserved distance of 11 nm between the tip and the envelope/matrix was again apparent (panels 2-5C and 2-5D), but no clear density in the very top of the tip (hereafter referred to as the “cap”) was observed (yellow arrow in panels 2-5G and 2-5H). This appears to be a hole and may very well be in many of the VLPs, although it might alternatively reflect variability in the shape of the cap or the smearing due to the missing pyramid of data. To clarify this ambiguity, we looked

carefully at the non-denoised individual reconstructions in this region and observed that indeed there were many capsids without clear cap densities. In addition, the smearing effect of the missing pyramid would be expected to obscure both the base and the tip regions equally, but the base regions and their averages uniformly showed strong density. Thus we favor the interpretation that the cap region is variable and in some cases is not even completely closed. This would not have been easily observed previously in projection images because the lip of density surrounding the cap region would have appeared in that location. Finally, when the densities inside the capsids in the VLP averages are compared, we observe that more density appears within the base than the tip. This density seems to be concentrated in a third concentric layer (yellow arrow in panel 2-5E) cupped ~10 nm inside the capsid base.

Discussion

The architecture of the layers of HIV-1 and their morphogenesis are not only intrinsically interesting from a structural point of view, but may also lead to novel therapeutics that block assembly or maturation. Indeed, several small molecules have already been reported to block structural transitions required for the assembly or maturation of several viruses, including HIV-1^{24; 25; 26}. Unfortunately, the architecture of HIV-1 has been difficult to study because each virus is unique, and therefore traditional X-ray crystallographic and EM methods are not applicable. For unique specimens, the highest resolution structural technique available today is electron tomography. In this study we have applied state-of-the-art electron cryotomography to produce the first three-dimensional structures of whole, native HIV-1 VLPs.

Several lines of evidence indicate that the VLPs we imaged were indeed authentic structural homologs of wild type HIV-1. Firstly, the point mutations introduced into the RT and RNase H proteins would not be expected to have any structural consequence at the low resolutions seen here. Similarly, the absence of Env protein is also unlikely to impact the internal structure, since in a recent study Env trimers were not observed to be distributed uniformly or in any particular pattern⁶. Moreover, our measurements of viral particle size and the general sizes and shapes of the viral core are in excellent agreement with recent cryo-EM measurements made on authentic, but chemically inactivated HIV-1 particles^{3;4}.

The structures reported here support the fullerene cone model of the organization of the capsid. While the usual variety of capsid morphologies was seen ranging from cones to rods to other irregular shapes, all the capsids observed here, including those that were pleiomorphic, contain similarly shaped edges, vertices, and angles, giving the impression of objects built from the same underlying motifs. The majority were cones, and they could be aligned surprisingly well in three dimensions. The fullerene cone model predicts that for a cone with five “pentons” in the tip and seven in the base, the cone angle should be $\sim 19^\circ$, but of course this would only be uniform around the long axis of the cone if the distribution of pentons in the base and the tip were perfectly symmetric, which is physically impossible for a 5,7 fullerene cone. We observed a conserved progression of cone angles from $\sim 24^\circ$ to $\sim 18^\circ$, consistent with the predicted 19° but indicating that the cones are slightly flattened and have roughly elliptical cross sections. All of these measurements agreed very well with the corresponding cone angle parameters observed for idealized fullerene cones.

Our data also strongly support the idea that HIV capsid assembly must involve a *de novo* assembly process rather than a concerted condensation of the immature Gag lattice. Specifically, we observed VLPs with multiple capsids, and even what we believe are nested capsids, both of which are incompatible with a concerted condensation mechanism. While it is possible that the most internal, concentric layers of density inside VLPs “10a” and “1g” are highly ordered RNP, we favor the interpretation that they are nested capsids because they have the same width, shape, and density (contrast) as the other capsids. Furthermore, consistent with measurements made by others^{4; 27}, we find that only about one-third of the available CA molecules assemble into capsids, which again precludes concerted condensation models (Table 2-1). Finally, we note that “simple condensation” would require the unreasonable proposition that pentagonal defects, which are presumably distributed throughout a spherical immature Gag lattice, could “migrate” through the hexagonal lattice to cause cone formation.

The mechanism of *de novo* capsid assembly is an important question, and two general models can be envisioned: 1) spontaneous, “concentration-driven” assembly pathways in which the shape of the viral capsid is ultimately determined by local inter-CA interactions, or 2) a “template-driven” mechanism in which other viral components nucleate assembly of the viral capsid. Our data indicate that both local inter-CA and templating interactions likely play important roles in HIV capsid assembly. Spontaneous assembly must be possible because pure recombinant CA proteins can assemble into conical capsids in the absence of any other viral proteins¹⁵ and because we observed the formation of nested capsids within VLPs (see Fig. 2-3A–C). On the other hand, it is likely that the viral matrix and/or RNP layers play a role in helping to nucleate capsid

assembly *in vivo* because a simple concentration-driven model would not explain the observation that up to five total capsids can form in a single VLP (i.e., capsids can form even after the majority of free CA molecules have been incorporated into other capsids; see VLP “1g” and ref. ⁴). Further support for a templated assembly mechanism is provided by our observations that there are defined spatial dispositions between the viral capsid and the adjacent matrix and RNP layers, and by the conserved structural features seen in different viral capsids. The latter two points are considered in greater detail below.

Evidence for specific interactions between the capsid and the adjacent envelope/matrix and RNP layers is provided by the fact that these different layers exhibit similar spacing in multiple VLP structures. The “peak-to-peak” distance between the matrix and the capsid was uniformly 11 nm along the base and the tip of the capsid (Fig. 2-5), and this same spacing was also sometimes observed along the side of the capsid (e.g., see Fig. 2-2, VLP 1k, central image). This spacing is not an artifact of denoising, since the reconstructions used to calculate the average VLP (which document the consistency of the spacing) were not denoised, nor is it an artifact of defocus, because while defocus blurs edges, it does not change the separation between density peaks. At present, we cannot definitively explain why the matrix and capsid layers are so consistently spaced at either end of the capsid, though there must be, of course, some physical interaction that promotes this spacing. It is interesting to note that this distance matches very well the analogous spacing seen in immature virions (see ref. ²⁸ Figure 2-2B, measuring from the center of the lipid envelope/matrix layer to the middle of the presumed capsid peaks), and it may therefore be a remnant of that structure that is

preserved during maturation. It is unlikely, however, that covalent MA-CA linkages are maintained in the mature virion, as Gag processing appears to proceed to completion and mature viral cores can be isolated away from the matrix/envelope layer^{29; 30; 31}. We did not observe any consistent “20 nm thin structural link,” previously termed the core-envelope linkage or CEL structure⁵ between the cap of the viral core and the matrix layer. Similarly, we did not see regular “lateral bodies¹” along the sides of the viral capsid, but instead typically saw scattered and only occasionally aggregated densities between the matrix and capsid layers. We suggest that these previous observations could have been artifacts of fixation and staining. Finally, we did not observe either an “irregular slit” or “cavities or holes...distributed primarily in the wide end” of the capsid structure, as previously reported⁵.

Others have previously observed a preponderance of density within the base (as opposed to the tip) of the core (e.g., see ref³), and it is therefore likely that most of the RNP components reside in the wide end of the capsid. Consistent with these observations, we observed a third layer of density in the averaged VLP structures, which appeared just inside the capsid base (Figure 2-5E, yellow arrow). We interpret this density as part of the RNP complex, and speculate that it might have served as a template to guide formation of the bases into their consistent shape and size. Interestingly, genetic studies also support the idea that the internal capsid surface may make functionally important interactions with the RNP complex and its associated enzymes. For example, subtle mutations in the internal MHR motif of RSV CA apparently do not compromise overall capsid assembly, but nevertheless prevent reverse transcription in the newly infected target cell³². Similarly, point mutations that alter the stability of the HIV-1

capsid also reduce the efficiency of DNA synthesis³³. Thus, it appears that the retroviral capsid performs an important functional role in helping to organize the viral RNP particle for successful uncoating and reverse transcription in a new host cell.

Several observations revealed that a special capsid shape is heavily favored *in vivo*. Firstly, while purified CA protein can form sheets, rods, and various cones in different ratios depending on environmental conditions¹⁵, much less variety was seen here *in vivo*, where the majority of capsids form cones of the 5,7 penton distribution type. If capsid assembly were not a directed process, then the hexagonal capsid net would self-assemble into lattices with pentameric disclinations at random positions. It has been shown, however, that the vast majority of such hypothetical self-assembling surfaces would not close, and it is clear that the vast majority of those that did would be roughly spherical³⁴. The number of cones that would emerge would be small, and those with a 5,7 penton distribution would be a special class among them. The frequency of finding a 5,7 cone with a particular size and shape in its base would be, we believe (though without specific calculation), essentially negligible. Nevertheless the majority class of actual VLPs observed here does in fact share just such an improbable capsid structure, which argues strongly for the presence of local and/or templating interactions that promote this preferred capsid shape *in vivo*.

In this initial tomographic study we used imaging conditions chosen to highlight the gross structural features of HIV-1. Higher resolution structures should be achievable in the near future through several improvements: the use of smaller defocus values, which enhance high resolution features at the expense of low resolution contrast; CTF-correction across the focal gradients present in the images³⁵; optimization of the process

of merging dual-axis tilt series of frozen-hydrated samples^{36, 37}; thinning of the ice and reduction of sucrose and other high density, contrast-matching molecules in the buffer; and ultimately, detection of the underlying periodicity of the protein layers and subsequent “unit cell” averaging until atomic models can be reliably docked.

Materials and Methods

Preparation of VLP. HIV-1 VLPs were made non-infectious by inactivation of the essential Env, RT, and RNase H proteins. An HIV-1_{NL4-3} R9 proviral vector³⁸ with a frameshift mutation in the env gene that blocked Env protein production was obtained as a gift from Dr. Christopher Aiken (Vanderbilt University). Although Env deletion alone blocks viral infectivity, two additional mutations were added that also independently block viral replication. First, the viral RT was inactivated with a D185A (RT_{D185A}) mutation. D185 is an RT active site residue that forms part of the catalytic triad. The mutation has been reported to block viral replication^{39; 40} and this was confirmed in our laboratory (data not shown). Second, the RNase H protein was inactivated with a H539A mutation (RNaseH_{H539A}), which also blocks replication (⁴¹ and our data not shown). DNA sequencing confirmed the presence of all three inactivating mutations in the Δ Env/RT_{D185A}/RNaseH_{H539A} R9 construct.

VLPs were produced by transfecting the Δ Env/RT_{D185A}/RNaseH_{H539A} R9 proviral DNA construct into 293T cells. Lipofectamine (Invitrogen) transfections followed manufacturers' instructions (10×10 cm plates; 10 μ g R9 DNA/plate), and VLP-containing supernatants (8 mL) were harvested 24 and 48 h post-transfection. VLP

particles were concentrated by ultracentrifugation (30,000 RPM for 1.5 h in a Beckman Ti50.2 rotor, 4°C) through 20% sucrose cushions (17.5 mL culture samples overlaid on 8 mL cushions) in STE buffer (10 mM Tris, pH 7.4; 100 mM NaCl, 1 mM EDTA). Concentrated viral stocks were resuspended (250 μ L in STE buffer), overlaid on 10 mL sucrose gradients (20–60%), centrifuged (34,000 RPM for 16 h in a Beckman SW-41 rotor), and harvested in 1 mL fractions. Viral fractions were assayed by SDS-PAGE, and the major bands visible by Coomassie Blue staining were confirmed to be the viral MA, CA, and NC proteins by Western blotting. 4 \times 1 mL VLP-containing fractions were combined, diluted with 2 mL STE buffer, and VLPs were pelleted by ultracentrifugation (55,000 RPM for 1 h in a tabletop ultracentrifuge). The concentrated pellets were then resuspended in \sim 100 μ L STE buffer for EM analyses.

Cryoelectron tomography. Purified HIV-1 VLPs were flash-frozen onto glow-discharged Quantifoil grids in liquid ethane using a Vitrobot. Ten nanometer gold fiducial markers were both dried onto the grids and mixed into the virus solutions before freezing. Frozen-hydrated grids were loaded into the new “flip-flop” tilt rotation holder, introduced into a 300 kV, FEG “G2 Polara” FEI TEM, and kept continuously frozen by thermal contact with liquid nitrogen. Image tilt series were collected from approximately -60° to $+60^\circ$ with a 3° tilt step automatically using the “predictive” UCSF tomography package⁴², and then the grid was rotated $\sim 90^\circ$ and a second tilt series was collected with the same tilt increment through approximately the same tilt range. All images were energy filtered with an energy slit width of 20 eV, recorded with a defocus of $\sim 16 \mu\text{m}$, with CCD pixels representing 0.67 nm on the specimen.

Image processing. Images were binned twofold, and then dual-axis tomographic reconstruction was performed using the IMOD package²¹. Briefly, each single-axis tilt series was aligned independently and used to calculate a three-dimensional reconstruction in real space by standard methods. The second reconstruction was divided into cubes and aligned piecewise to the first by cross-correlation, and was then re-interpolated to compensate for potential distortions between the two tilt series. The first reconstruction and the adjusted second reconstruction were Fourier transformed and merged in reciprocal space by simple averaging in those voxels for which structure factors were available from both tilt series. From the completed tomograms, individual VLPs were manually selected and denoised by 30 rounds of nonlinear anisotropic diffusion²². Capsids were selected and segmented semi-automatically along with their corresponding lipid envelopes using the Amira software package (Mercury Computer Systems, Inc.). Custom Amira modules were written to measure the capsid cone angle as a function of rotation about the cone axis and to align VLPs by either the tip or base of the capsid cone. Figures were produced with Amira.

Acknowledgements

This work was supported by NIH Grant PO1 GM66521 to WIS and GJJ, as well as gifts from the Ralph M. Parsons Foundation, the Agouron Institute, and the Gordon and Betty Moore Foundation to the California Institute of Technology. We are grateful to Uta von Schwedler and Kirsten Stray for assistance with VLP preparations, and we thank Simon Wain-Hobsen for suggesting that we estimate the concentrations of enzymes in the viral core.

References

1. Gelderblom, H. R., Hausmann, E. H. S., Ozel, M., Pauli, G. & Koch, M. A. (1987). Fine-Structure of Human Immunodeficiency Virus (Hiv) and Immunolocalization of Structural Proteins. *Micron and Microscopica Acta* **18**, 335-336.
2. Goto, T., Nakai, M. & Ikuta, K. (1998). The life-cycle of human immunodeficiency virus type 1. *Micron* **29**, 123-38.
3. Briggs, J. A. G., Wilk, T., Welker, R., Krausslich, H. G. & Fuller, S. D. (2003). Structural organization of authentic, mature HIV-1 virions and cores. *EMBO Journal* **22**, 1707-1715.
4. Briggs, J. A. G., Simon, M. N., Gross, I., Krausslich, H. G., Fuller, S. D., Vogt, V. M. & Johnson, M. C. (2004). The stoichiometry of Gag protein in HIV-1. *Nature Structural & Molecular Biology* **11**, 672-675.
5. Hoglund, S., Ofverstedt, L. G., Nilsson, A., Lundquist, P., Gelderblom, H., Ozel, M. & Skoglund, U. (1992). Spatial visualization of the maturing HIV-1 core and its linkage to the envelope. *AIDS Res Hum Retroviruses* **8**, 1-7.
6. Zhu, P., Chertova, E., Bess, J., Lifson, J. D., Arthur, L. O., Liu, J., Taylor, K. A. & Roux, K. H. (2003). Electron tomography analysis of envelope glycoprotein trimers on HIV and simian immunodeficiency virus virions. *Proceedings of the National Academy of Sciences of the United States of America* **100**, 15812-15817.
7. Turner, B. G. & Summers, M. F. (1999). Structural biology of HIV. *J Mol Biol* **285**, 1-32.

8. Rao, Z., Belyaev, A. S., Fry, E., Roy, P., Jones, I. M. & Stuart, D. I. (1995). Crystal structure of SIV matrix antigen and implications for virus assembly. *Nature* **378**, 743-7.
9. Hill, C. P., Worthylake, D., Bancroft, D. P., Christensen, A. M. & Sundquist, W. I. (1996). Crystal structures of the trimeric human immunodeficiency virus type 1 matrix protein: implications for membrane association and assembly. *Proc Natl Acad Sci USA* **93**, 3099-104.
10. Tang, C., Loeliger, E., Luncsford, P., Kinde, I., Beckett, D. & Summers, M. F. (2004). Entropic switch regulates myristate exposure in the HIV-1 matrix protein. *Proc Natl Acad Sci USA* **101**, 517-22.
11. Li, S., Hill, C. P., Sundquist, W. I. & Finch, J. T. (2000). Image reconstructions of helical assemblies of the HIV-1CA protein. *Nature* **407**, 409-413.
12. Mayo, K., Huseby, D., McDermott, J., Arvidson, B., Finlay, L. & Barklis, E. (2003). Retrovirus capsid protein assembly arrangements. *J Mol Biol* **325**, 225-37.
13. Ge, M. & Sattler, K. (1994). Observation of fullerene cones. *Chem. Phys. Lett.* **220**, 192-196.
14. Ebbesen, T. (1998). Cones and tubes: geometry in the chemistry of carbon. *Accounts of Chemical Research* **31**, 558-566.
15. Ganser, B. K., Li, S., Klishko, V. Y., Finch, J. T. & Sundquist, W. I. (1999). Assembly and analysis of conical models for the HIV-1 core. *Science* **283**, 80-83.
16. Jin, Z. M., Jin, L., Peterson, D. L. & Lawson, C. L. (1999). Model for lentivirus capsid core assembly based on crystal dimers of EIAV p26. *Journal of Molecular Biology* **286**, 83-93.

17. Dubochet, J., Adrian, M., Chang, J. J., Homo, J. C., Lepault, J., McDowell, A. W. & Schultz, P. (1988). Cryo-electron microscopy of vitrified specimens. *Q. Rev. Biophys.* **21**, 129-228.
18. Koster, A. J., Grimm, R., Typke, D., Hegerl, R., Stoschek, A., Walz, J. & Baumeister, W. (1997). Perspectives of molecular and cellular electron tomography. *Journal of Structural Biology* **120**, 276-308.
19. Subramaniam, S. & Milne, J. L. S. (2004). Three-dimensional electron microscopy at molecular resolution. *Annu. Rev. Biophys. Biomol. Struct.* **33**, 141-155.
20. Sali, A., Glaeser, R., Earnest, T. & Baumeister, W. (2003). From words to literature in structural proteomics. *Nature* **422**, 216-25.
21. Kremer, J. R., Mastronarde, D. N. & McIntosh, J. R. (1996). Computer Visualization of Three-Dimensional Image Data Using Imod. *Journal of Structural Biology* **116**, 71-76.
22. Frangakis, A. S. & Hegerl, R. (2001). Noise reduction in electron tomographic reconstructions using nonlinear anisotropic diffusion. *J. Struct. Biol.* **135**, 239-50.
23. Ganser-Pornillos, B. K., von Schwedler, U. K., Stray, K. M., Aiken, C. & Sundquist, W. I. (2004). Assembly properties of the human immunodeficiency virus type 1 CA protein. *Journal of Virology* **78**, 2545-2552.
24. Prevelige, P. E., Jr. (1998). Inhibiting virus-capsid assembly by altering the polymerisation pathway. *Trends Biotechnol* **16**, 61-5.
25. Li, F., Goila-Gaur, R., Salzwedel, K., Kilgore, N. R., Reddick, M., Matallana, C., Castillo, A., Zoumplis, D., Martin, D. E., Orenstein, J. M., Allaway, G. P., Freed,

- E. O. & Wild, C. T. (2003). PA-457: a potent HIV inhibitor that disrupts core condensation by targeting a late step in Gag processing. *Proc Natl Acad Sci USA* **100**, 13555-60.
26. Tang, C., Loeliger, E., Kinde, I., Kyere, S., Mayo, K., Barklis, E., Sun, Y., Huang, M. & Summers, M. F. (2003). Antiviral inhibition of the HIV-1 capsid protein. *J Mol Biol* **327**, 1013-20.
27. Lanman, J., Lam, T. T., Emmett, M. R., Marshall, A. G., Sakalian, M. & Prevelige, P. E., Jr. (2004). Key interactions in HIV-1 maturation identified by hydrogen-deuterium exchange. *Nat Struct Mol Biol* **11**, 676-7.
28. Wilk, T., Gross, I., Gowen, B. E., Rutten, T., de Haas, F., Welker, R., Krausslich, H. G., Boulanger, P. & Fuller, S. D. (2001). Organization of immature human immunodeficiency virus type 1. *Journal of Virology* **75**, 759-771.
29. Welker, R., Hohenberg, H., Tessmer, U., Huckhagel, C. & Krausslich, H. G. (2000). Biochemical and structural analysis of isolated mature cores of human immunodeficiency virus type 1. *Journal of Virology* **74**, 1168-1177.
30. Kotov, A., Zhou, J., Flicker, P. & Aiken, C. (1999). Association of Nef with the human immunodeficiency virus type 1 core. *J Virol* **73**, 8824-30.
31. Accola, M. A., Ohagen, A. & Gottlinger, H. G. (2000). Isolation of human immunodeficiency virus type 1 cores: retention of Vpr in the absence of p6(gag). *J Virol* **74**, 6198-202.
32. Cairns, T. M. & Craven, R. C. (2001). Viral DNA synthesis defects in assembly-competent Rous sarcoma virus CA mutants. *J Virol* **75**, 242-50.

33. Forshey, B. M., von Schwedler, U., Sundquist, W. I. & Aiken, C. (2002). Formation of a human immunodeficiency virus type 1 core of optimal stability is crucial for viral replication. *J Virol* **76**, 5667-77.
34. Manolopoulos, D. E., May, J. C. & Down, S. E. (1991). Theoretical studies of the fullerenes: C₃₄ to C₇₀. *Chem. Phys. Lett.* **181**, 105-111.
35. Winkler, H. & Taylor, K. A. (2003). Focus gradient correction applied to tilt series image data used in electron tomography. *Journal of Structural Biology* **143**, 24-32.
36. Mastronarde, D. N. (1997). Dual-axis tomography: an approach with alignment methods that preserve resolution. *J. Struct. Biol.* **120**, 343-52.
37. Penczek, P., Marko, M., Buttle, K. & Frank, J. (1995). Double-Tilt Electron Tomography. *Ultramicroscopy* **60**, 393-410.
38. Swingler, S., Gallay, P., Camaur, D., Song, J., Abo, A. & Trono, D. (1997). The Nef protein of human immunodeficiency virus type 1 enhances serine phosphorylation of the viral matrix. *J Virol* **71**, 4372-7.
39. Boyer, P. L., Ferris, A. L. & Hughes, S. H. (1992). Cassette Mutagenesis of the Reverse-Transcriptase of Human-Immunodeficiency-Virus Type-1. *Journal of Virology* **66**, 1031-1039.
40. Kaushik, N., Rege, N., Yadav, P. N. S., Sarafianos, S. G., Modak, M. J. & Pandey, V. N. (1996). Biochemical analysis of catalytically crucial aspartate mutants of human immunodeficiency virus type 1 reverse transcriptase. *Biochemistry* **35**, 11536-11546.

41. Tisdale, M., Schulze, T., Larder, B. A. & Moelling, K. (1991). Mutations within the Rnase-H Domain of Human-Immunodeficiency-Virus Type-1 Reverse-Transcriptase Abolish Virus Infectivity. *Journal of General Virology* **72**, 59-66.
42. Zheng, Q. S., Braunfeld, M. B., Sedat, J. W. & Agard, D. A. (2004). An improved strategy for automated electron microscopic tomography. *J. Struct. Biol.* **147**, 91-101.

Figure and table legends

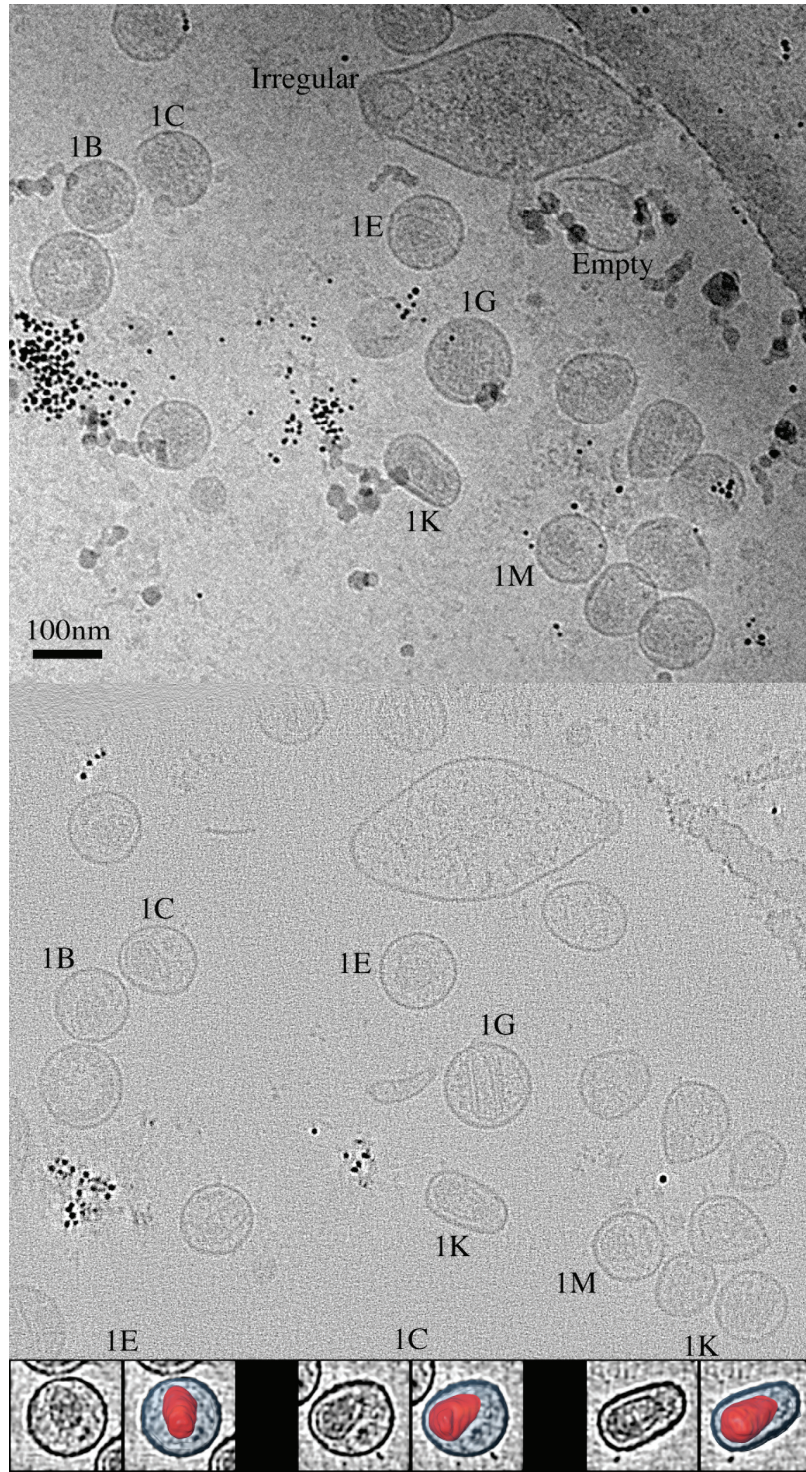


Figure 2-1. Primary data and processing steps.

Top: Purified HIV-1 virus-like particles were frozen in thin films across EM grids. Series of images were recorded of many such fields of frozen particles as the sample was incrementally tilted about one axis and then a second, orthogonal axis. One experimental image from one tilt series is shown. The roughly spherical objects are mostly HIV-1 VLPs (including those labeled “1B,” “1C,” “1E,” “1G,” “1K,” and “1M”), but some apparently “empty” liposomes are also present in the sample (“Empty”) as well as other irregular forms (“Irregular”). The small black dots are 10 nm gold fiducials used to align the tilt series for reconstruction, and the large arc appearing across the upper right corner is the edge of a circular hole in a supporting carbon film. *Middle:* Three-dimensional reconstructions of the fields of VLPs were calculated from the various series of tilted images. A single section 1.34 nm thick through the middle of the reconstruction corresponding to the image above is shown. Because this is a single section, some objects that are seen in the projection image above (for instance many of the gold beads) do not appear. *Bottom:* Individual VLPs were selected from the reconstruction and denoised, and then the boundaries of the lipid bilayer and capsid were semi-automatically delineated (“segmented”). Three examples (“1E,” “1C,” and “1K”) are shown. In each pair, the left image shows a single section through the middle of an extracted, denoised VLP. The right image shows three-dimensional renditions of our interpretation of the capsids in red, shown in place within the denoised section, with the area enclosed by the lipid bilayer in blue.

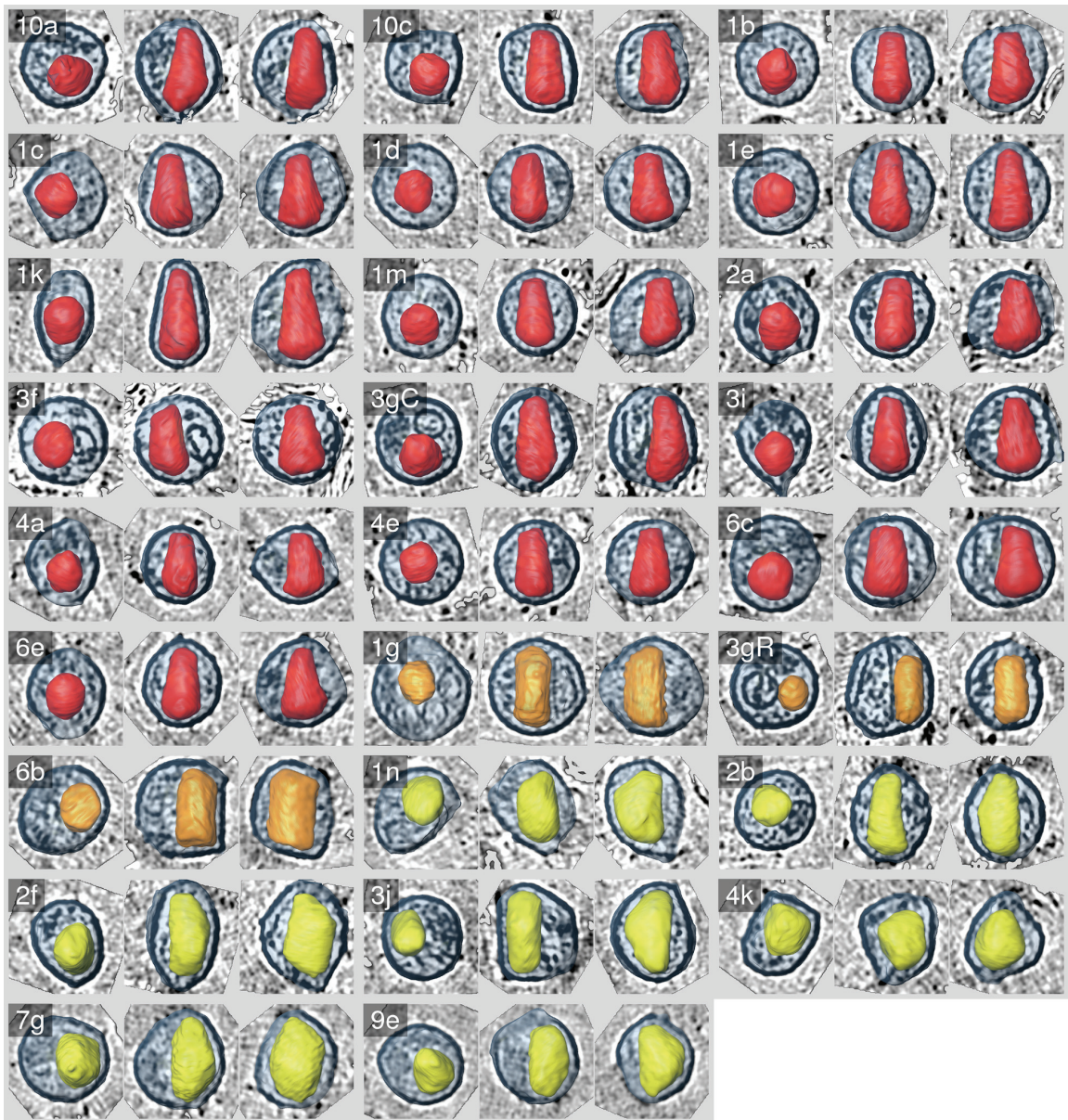


Figure 2-2. Montage of all segmented HIV-1 VLPs.

Twenty-six VLPs were segmented and aligned along their principal axes. Three views are shown for each VLP, presenting from left to right axial, sagittal, and coronal perspectives, respectively. Three-dimensional renditions of the capsid surfaces are shown in red for cones, orange for rods, and yellow for all others, placed within a denoised two-

dimensional section through the middle of the VLP, with the area enclosed by the lipid bilayer in blue. Because each VLP was extracted as a cube from a larger three-dimensional reconstruction and then aligned to the others, the boundaries of the images appear as randomly oriented, clipped squares. Each capsid is identified by a number and a letter, where the number signifies which field of particles it came from. Capsids 3gR and 3gC are part of the same, double-capsid VLP. The edges of the boxes containing each VLP image here and in all other figures represent 160 nm.

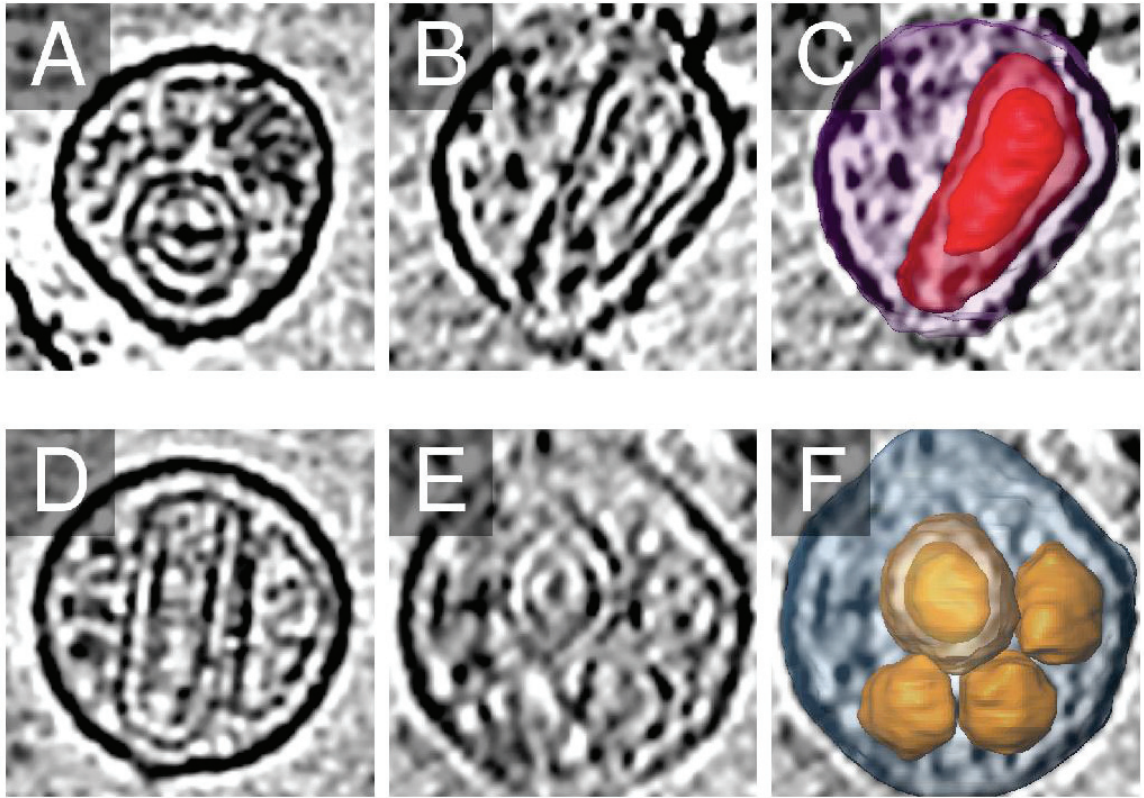


Figure 2-3. Nested capsids.

Two VLPs, “10a” (panels A–C) and “1g” (panels D–F), presented nested capsids. Panels A and D show sagittal sections, panels B and E show coronal sections, and panels C and F show three-dimensional renditions as in Figure 2-2, except that the outer capsid surface has been made transparent to reveal the inner capsid, and in the case of VLP “1g” (panel F), the surfaces of all five capsids present are rendered.

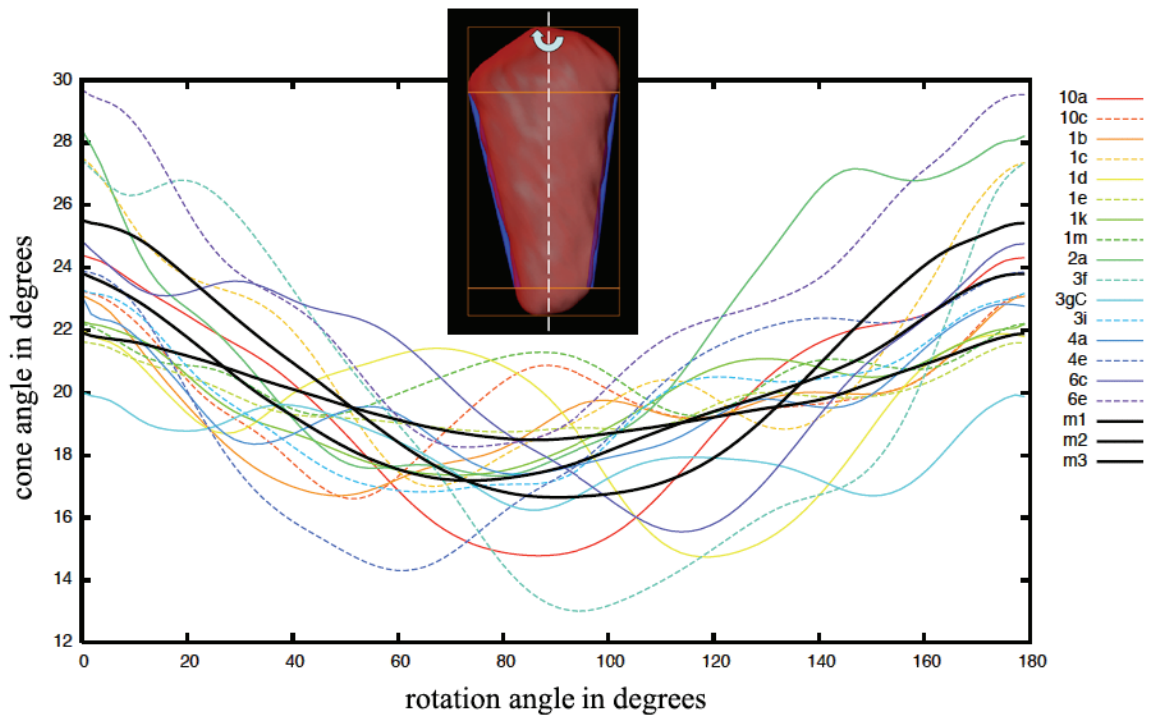


Figure 2-4. Cone angle variation in 3D.

The cone angle in degrees for the 16 conical capsids is plotted as a function of rotation around the cone axis from 0° – 180° . The methodology is depicted in the inset. For each measurement, straight lines (blue in inset) were fit to the edges of the cone between the base and the tip. These lines defined the cone angle as the cone was rotated around its long axis. The resulting values were plotted by assigning the rotation position corresponding to the maximum cone angle as “ 0° .” The unique VLP identifiers are shown in the legend. The three black curves are the corresponding cone angles for three different theoretical fullerene cones modeled to mimic HIV-1 capsids, as described previously^{11; 23}.

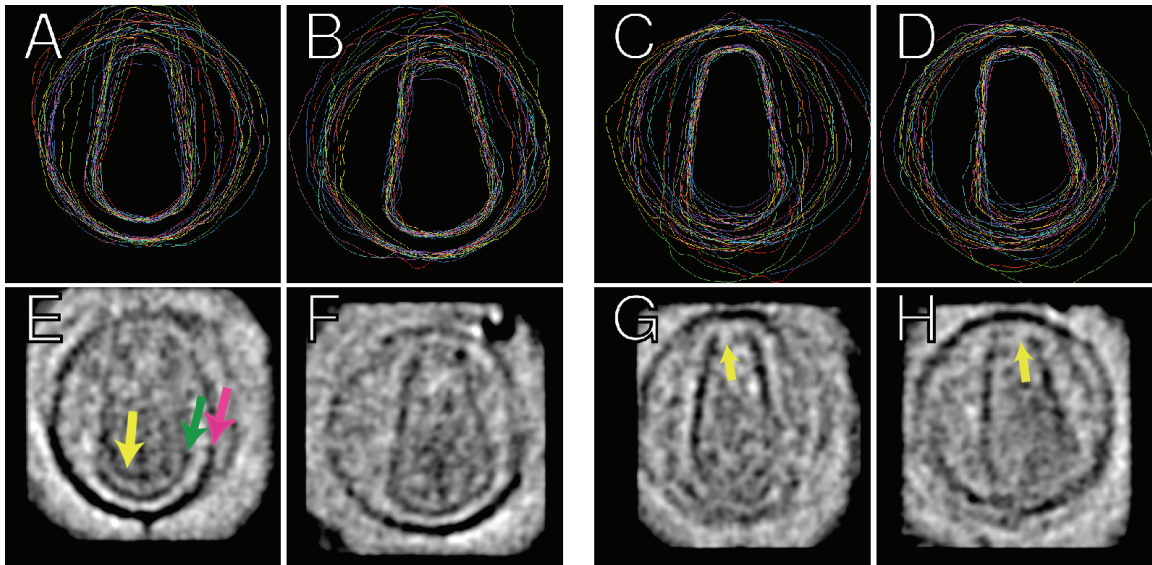


Figure 2-5. Conserved patterns of density in VLPs.

The 16 VLPs with conical capsids were aligned using either the bases (panels A, B, E, and F) or the tips (panels C, D, G, and H). The top panels show sagittal (A and C) and coronal (B and D) sections through the capsids and lipid bilayer surfaces, with the same color code for each VLP as in Figure 2-4. The bottom panels show again sagittal (E and G) and coronal (F and H) sections through the corresponding three-dimensional average VLP. In panel E, the magenta arrow points towards the edge of the average bilayer/matrix layer, the green arrow points towards the edge of the average capsid, and the yellow arrow points towards the presumed average internal RNP density. In panels G and H, the yellow arrows point to the missing average “cap” density. Notable features include the surprisingly uniform, asymmetric capsid base (panel B); the uniform cone angles (particularly panels B and D); the uniform distance between the capsid base and the bilayer/matrix layer (panels A and B); the preponderance of internal density within the base as opposed to the tip of the average capsids (panels E–H); the conserved internal density lining the inside of the average capsid base (panel E in particular); and the lack of clear density in the “cap” of the average capsid tip (panels G and H). The very dark density in the upper right corner of panel F outside the VLP is an artifact due to gold fiducials in one of the reconstructions.

VLP	Experimentally determined external surface areas (nm ²)		Calculated numbers of molecules	
	envelope/ matrix	capsid	MA	CA
10a*	53,000	27,000	4,700	1,600
10c	45,000	18,000	3,600	1,100
1b	46,000	17,000	3,500	1,000
1c	48,000	17,000	4,000	1,000
1d	47,000	16,000	3,700	1,000
1e	52,000	19,000	4,200	1,200
1g*	62,000	59,000	5,100	3,600
1k	49,000	21,000	4,300	1,300
1m	45,000	16,000	3,400	900
2a	48,000	18,000	3,900	1,100
3f	52,000	17,000	4,300	1,000
3g*	54,000	33,000	4,200	2,000
3i	47,000	17,000	3,900	1,000
4a	39,000	14,000	2,800	900
4e	46,000	16,000	3,400	900
6c	56,000	20,000	4,500	1,200
6e	45,000	16,000	3,400	1,000
6b	60,000	24,000	4,900	1,400
1n	52,000	20,000	4,400	1,200
2b	48,000	19,000	3,700	1,200
2f	50,000	21,000	4,000	1,300
3j	51,000	19,000	4,000	1,200
4k	45,000	17,000	3,600	1,000
7g	53,000	23,000	4,200	1,400
9e	45,000	18,000	3,300	1,100
mean	49,000	21,000	4,000	1,300
stddev	5,200	9,000	530	540

Table 2-1. Surface area measurements.

The surface areas of each segmented envelope/matrix and capsid shell were measured and presented in the same order as they appear in Figure 2-2. Assuming each is a hexagonal net, and taking lattice spacings from the literature (see text), the numbers of

MA and CA monomers involved were estimated. Asterisks mark VLPs with multiple capsids, where the entire capsid surface area was summed.

Chapter 3: Immature HIV-1 virus-like particles imaged by electron cryotomography

Elizabeth R. Wright^{1§}, Jordan Benjamin^{1§}, H. Jane Ding¹, Collin Kieffer², Christopher Fillmore³, Wesley I. Sundquist², and Grant J. Jensen^{1*}

¹Division of Biology, California Institute of Technology, 1200 E. California Blvd.,
Pasadena, CA 91125

²Department of Biochemistry, University of Utah, 20 North 1900 East, Salt Lake City,
UT 84132

³Translational Genomics Research Institute, 445 N. Fifth St., Phoenix, AZ 85004

§These authors contributed equally to this work.

*To whom correspondence should be addressed: jensen@caltech.edu, 626-395-8827
(phone) 626-395-5730 (fax)

Abstract

The major structural elements of retroviruses are contained in a single polyprotein, Gag, which in HIV-1 comprises the matrix (MA), capsid (CA), SP1, nucleocapsid (NC), SP2, and p6 proteins. In the immature HIV-1 virion, the domains of Gag are arranged radially with the amino-terminus of MA at the membrane and NC-p6 facing the particle center. While assembly of the mature virus from the immature form has been studied extensively, and the structural elements of both have been identified and determined, a complete understanding of the immature virus has remained elusive. Here, we report the first three-dimensional structure of individual immature HIV-1 virus-like particles (VLPs) obtained by electron cryotomography. We measured the viral particles and found the diameters ranged from 115 to 140 nm with a mean of 127 nm. The radial spoke arrangement of the Gag polyprotein was clearly visible in the tomograms. The thicknesses of the domains of the Gag polyprotein were measured to be: membrane-MA $78 \pm 11 \text{ \AA}$, CA $77 \pm 12 \text{ \AA}$, and NC $43 \pm 11 \text{ \AA}$. Upon producing surface projections of each layer of Gag, it was determined that only the CA and SP1 domains contained regions of order within the viral particles. The CA and SP1 layers were arranged in hexagonal lattices interspersed between patches of disorder. The ring to ring spacing of the CA NTD lattice was 8 nm and the ring to ring spacing of the SP1 lattice was 7.5 nm. From our data, we propose a pseudoatomic model for the CA and SP1 domains of immature HIV-1.

Introduction

The major structural elements of retroviruses are contained in a single polyprotein, Gag, which in HIV-1 comprises the matrix (MA), capsid (CA), SP1, nucleocapsid (NC), p1, and SP2 proteins [1]. Each of these folds into an independent domain of Gag with the exceptions of SP1 and SP2, which are short spacer peptides, and CA, which is itself divided into globular N- and C-terminal domains (the NTD and CTD). In the immature HIV-1 virion, the domains of Gag are arranged radially with the N-terminus of MA at the membrane and NC-p6 facing the particle center [2]. Once the immature virus buds from the cell, the maturation process begins as protease (PR) cleaves Gag. The individual domains reassemble into the mature viral form, in which MA remains associated with the membrane through a myristyl modification and CA forms the conical viral core that contains NC, the genomic RNA, and other viral material.

While assembly of the mature virus from the immature form has been studied extensively, and the structural elements of both have been identified and determined, a complete understanding of the immature virus has remained elusive. Both immature and mature viral particles are roughly spherical in shape and range in size from 100 to 250 nm [2-5]. The Gag shell of the immature virus has usually been described as ring-shaped in two-dimensional sections or projection images, but asymmetrical crescent-shapes have also been reported [2, 3, 6]. It has been difficult to elucidate the structural roles played by each of the Gag domains in the immature virion, partly because the assembly process is quite robust. However, molecular genetic studies have indicated that the CA CTD and SP1 regions are most important to the assembly process, with NC and p6 promoting nonspecific interactions through RNA binding [7-11]. It has been proposed that MA

forms a trimeric lattice that helps stabilize the Gag shell, although MA is not essential for viral budding or replication [12-19].

The immature HIV particle contains approximately 5,000 copies of Gag as measured by a combination of cryo-EM and STEM [5]. Upon maturation, less than one-third of the CA from Gag forms the core of the mature virus, thereby leaving a large amount of CA either free within the virus or able to form multiple cores [4, 20, 21].

Models of the CA lattice of mature HIV-1 have been generated based on crystal structures and electron cryo-microscopy of isolated viral cores, *in vitro* assembled CA tubes and cores, and two-dimensional crystals of membrane-tethered CA [22-25]. Briefly, the mature CA lattice consists of hexameric rings formed by CA NTDs, with adjacent rings interconnected by dimers of CA CTDs [23, 26-28]. A CA NTD hexamer from a related virus has been solved to atomic resolution, revealing the major interfaces to be an 18-helix bundle formed by helices 1, 2, and 3, as well as interactions in the center of the ring between the N-terminal β -hairpin loops of the NTDs [29]. Several lines of evidence suggest this model is not valid for the immature particle. The β -hairpin cannot be formed without proteolytic cleavage of CA from MA [30-32]. Several groups have measured the spacing of the immature Gag lattice by electron cryo-microscopy and found it to be around 8 nm, while the mature CA lattice spacing is reported as 10–11 nm [2, 5, 19, 22, 33, 34]. To date, visualizations of the immature particle have not resolved the lattice structures of individual Gag domains, and no pseudoatomic model has yet been proposed.

Here, we report the first three-dimensional structure of individual immature HIV-1 virus-like particles (VLPs) obtained by electron cryotomography. We measured the components of the viral particles, observed the arrangement of the Gag polyprotein

within the immature virus, visualized locally ordered patches of CA and SP1 arranged in hexagonal lattices and measured their spacing, and propose a pseudoatomic model of the CA domain.

Results

Electron cryotomography. Immature HIV-1 VLPs were produced using a proviral expression vector containing mutations to the PR, RT, and RNase H enzymes. The mutation to PR halted the virus in the immature state; additionally RT and RNase H were mutated to insure the non-infectious nature of the viral preparations without altering viral structure. The VLPs were generated by transfecting the viral construct into 293T cells, harvesting the supernatant, and concentrating the viral particles by ultracentrifugation. The viral fractions were analyzed by SDS-PAGE (data not shown).

Solutions containing the immature HIV-1 VLPs were plunge-frozen onto EM grids. The frozen grids were inserted into a 300 kV FEG TEM and imaged at liquid nitrogen temperature. In addition to the immature HIV-1 VLPs, small vesicles, cellular debris, and other material was occasionally observed on the grids. Tilt series, which were energy filtered, were collected on the VLPs at defocus values ranging from 4 to 8 μm . Three-dimensional reconstructions were calculated using the IMOD tomography package (Figure 3-1) [35]. The immature VLPs were extracted from the tomograms and denoised with non-linear anisotropic diffusion (Figure 3-2) [36]. Sixteen of the highest quality reconstructions were selected for further analysis.

Radial Gag shell structure. The diameters of the viruses ranged from 115 to 140 nm with a mean of 127 nm. The radial spoke arrangement of the Gag protein layer

was clearly visible in slices through the tomograms (Figure 3-1). However, the Gag shell was not continuous around the diameter of any of the viruses, but rather had sectors where no ordered spokes were visible. The empty or disordered regions were substantial, comprising up to half of the viral surface. The two bands of the membrane-MA were apparent in ordered regions of the Gag shell, but only a single layer could be resolved in the disordered or empty regions (Figure 3-3). In areas with a double layer, this dimension was subdivided into two regions of density (outer: $32 \pm 3 \text{ \AA}$, inner: $31 \pm 5 \text{ \AA}$) separated by a space of $21 \pm 2 \text{ \AA}$. In regions where the Gag shell was discontinuous, a single layer with a thickness of $48 \pm 6 \text{ \AA}$ was observed. Radial density profiles of the viruses revealed three discrete bands, which were presumed to be the membrane-MA, CA, and NC domains (Figure 3-3). The average peak to peak distances between the membrane-MA, CA, and NC layers were $39 \pm 10 \text{ \AA}$ and $30 \pm 8 \text{ \AA}$, respectively. In several viral profiles, separate bands corresponding to the N- and C-terminal domains (NTD and CTD) of CA were resolved (Figure 3-3). The peak-to-peak distance between the two subdomains of CA was approximately 45 \AA .

Gag lattice analysis. Spherical triangle mesh surfaces were generated with their radii aligned to the three outer layers identified in the radial density plots for each virus. The electron density surrounding those surfaces was then projected onto them by summing the density sampled along radial lines at each triangle, with the size of the triangles chosen to be less than the voxel dimensions (Figure 3-4). A hexagonal lattice was clearly visible in large areas of the projected density from the CA layers of the viruses, but no order or pattern was apparent in the other two layers. The lattice appeared only on regions of the viruses in which the layers of Gag were clearly visible in slices

through the tomograms (Figure 3-5). An automated peak detection procedure was used to locate the putative unit cells of the hexagonal lattice. The resulting peaks were then ranked according to the standard deviation of the distance to each peak's six nearest neighbors, as a measure of the local hexagonal order (Figure 3-6). There was no significant correlation between those standard deviation values and the polar angle from the peak to the Z axis ($R^2 = 0.17$). A radial density plot was calculated from only the regions of one virus with standard deviation of neighbor distance less than 14 Å, which occupied 26% of the virus' area. Compared to the plot from the whole virus, this plot showed stronger and more distinct peaks for the CA and NC domains, as well as a small shoulder on the membrane-MA peak (Figure 3-3).

Real space averaging of Gag unit cells. The 120 peaks with a standard deviation of neighbor distance less than 14 Å were chosen from a representative viral surface projection. For each peak, the region of the tomogram containing the virus was rotated and translated so as to align the unit cells. An average was calculated from the transformed regions (Figure 3-7). The membrane-MA layer displayed no order and the leaflets of the bilayer could not be resolved in the averaged density. A distinct layer of low density at a radius of 525 Å separated the MA and CA domains. The average revealed a clear hexagonal pattern in the CA layer with a ring-to-ring spacing of 8 nm. The lattice extended beyond the single unit cell used for alignment and spanned a diameter of five hexamers, after which it became more diffuse until no order was discernable. Closer to the center, around 444 Å, was a featureless shell of relatively high density, followed by another hexagonal lattice with a center-to-center spacing of 7.5 nm. The density of this second lattice was inverted from the upper layer, comprising balls of

high density isolated by networked rings of low density (Figure 3-8). The high density regions of the second lattice were exactly beneath the holes of the first lattice. Beneath the second lattice was another undifferentiated high density layer, followed by the relatively uniform density of the viral center. A similar average computed from the 120 lowest ranked peaks showed only the low density hole and one dense ring in the CA layer used to generate the alignment, with no lattice structure apparent in that layer or any other.

Discussion

The structural characterization of immature HIV-1 has relied heavily upon standard negative stain and cryo- electron microscopy methods [2, 3, 5, 6, 33]. With the advent of electron cryotomography, automated data collection, and software developments; many questions concerning the structural details of large, non-symmetrical biological materials including viruses, cells, and macromolecular complexes are accessible. Efforts in the study of mature HIV-1 viral particles have already benefited from electron cryotomography. Several articles have described the morphology and position of the CA core within the mature virus using this method [4, 20].

A striking morphological element of immature viral particles illuminated through this study was the asymmetry of the Gag shell (Figure 3-2). Discontinuity within the Gag shell had been observed previously [2, 3, 6], but this was only seen in a minority of the two-dimensional slices and projections then available. All the immature particles analyzed in our study contained both ordered and disordered regions within the Gag shell. If this were an artifact of the virions' positions within the ice layer, or of the missing

wedge of information in the tomograms, we would expect to see a correlation between the degree of order observed and the position on the viral shell relative to the plane of the ice. That we did not find such a correlation suggests that the patchwork nature of the Gag lattice was a true feature of the viral structures. It is possible that the Gag shell does not close completely during the budding process. If this is the case, the formation of spherical Gag shells may not require the incorporation of pentamers, since the lattice is not closed [37].

The thickness of the three domains comprising the Gag shell of the immature viral particles were measured and were found to be consistent with the literature [3, 5]. A novel finding was that the membrane-MA domain had variability in its thickness depending on its location with respect to the ordered areas of Gag. When associated with ordered regions, it was thicker and maintained the double leaflet appearance. At regions where the Gag shell was not observed, the membrane-MA layer was substantially thinner (Figure 3-2). This may reflect the absence of MA protein at the membrane [3].

Using the radial surface projections, we were able to directly visualize the organization of each protein layer. We saw no repeating lattice in the MA shell projections, nor in the three-dimensional average, which lends further support to the idea that MA-MA contacts do not play a significant role in the structure of the Gag shell [8, 12, 13, 33, 38]. In the CA layer, a hexagonal lattice was easily discerned in the surface projections and even in slices through the tomograms. By applying what we believe is a novel procedure for real space averaging of repeating lattices embedded in curved surfaces, we were able to calculate an ensemble average from 120 unit cells. Interpretation was facilitated by comparison of the radial density plot to the

corresponding positions in the average (Figure 3-8). Hexagonal lattices were observed in both the CA NTD layer and, surprisingly, the SP1 spacer peptide between CA CTD and NC.

The 8 nm spacing and overall appearance of the NTD lattice were consistent with previous observations of the immature Gag lattice or in vitro equivalents [2, 5, 19, 22, 33, 34, 39]. While our reconstruction does not have sufficient resolution to unambiguously place crystal structures of CA, it does provide useful constraints for modeling. The relatively large (~40 Å) central holes in the NTD hexamers are incompatible with the structure observed in the mature lattice, in which helices 1 and 2 point toward the center of the ring. The spatial constraints favor a model in which NTDs from neighboring hexamers form dimeric interactions [22]. A crystal structure of Rous Sarcoma Virus CA NTD bearing an N-terminal extension has been solved [32]. That structure had a dimeric crystal contact along a twofold axis in the region of helix 6, and it was proposed that this dimer interface may be present in the immature particle. However, it was not possible to orient the NTDs to preserve that dimer interface and still fit the resulting hexamers into our density. We found that the NTDs could fit well with helix 5 lining the central hole in the hexamer (Figure 3-9). Although the CTD layer was poorly resolved, there was room in the electron density for the crystallographically defined CTD dimer connecting adjacent hexamers.

We observed a second hexagonal lattice in the averaged structure that was similar to the NTD layer, but with the density inverted. Examination of the radial density plot showed that this second lattice was formed by the SP1 spacer peptides between CA CTD and NC. The protein density associated with SP1 is directly below the central pore of the

hexameric lattice of the NTD. The SP1 peptide is required for viral assembly [40, 41] and forms an α -helix that may assemble into dimers or trimers [42]. There is evidence that SP1 preferentially stabilizes the Gag shell [40]. We found that a hexamer of SP1 α -helices docked perfectly into the second lattice layer in the averaged reconstruction, with NC and viral RNA presumably making up the disordered layer beneath (Figure 3-9, 3-10). Our model could allow the bundles of SP1 to help hold together CTDs from each hexamer, maintaining the tighter lattice characteristic of the immature particle.

Materials and Methods

Preparation of Immature VLPs. Mutations in the PR, RT, and RNase H genes of the HIV-1_{NL4-3} R9 proviral vector were made to render HIV-1 VLPs non-infectious and immature. The point mutations PR_{D25N}/RT_{D185A}/RNaseH_{H539A} were introduced via QuikChange PCR mutagenesis and confirmed by DNA sequencing (Stratagene).

VLPs were produced by transfecting the proviral DNA construct into 293T cells. 293T cells were grown in DMEM (Gibco/Invitrogen) + 10% FBS (Gibco/Invitrogen) in 10 cm plates (30 plates seeded with 6×10^6 cells per plate) and incubated for 24 hours (37° C at 5% CO₂). The cells were transfected with 12 μ g of the proviral DNA construct and 50 μ L Fugene6 transfection reagent (Roche) per plate. Six hours post-transfection, the media was replaced with 7 mL DMEM + 10% FBS and the cells were incubated for 40 hours. The supernatant containing VLPs was collected and filtered through a 0.45 μ m SFCA syringe filter (Corning) to remove cell debris. The filtered supernatant (~200 mL) containing the VLPs was placed onto 6 separate 5 mL 20% sucrose cushions (20% Sucrose W/V in STE Buffer (10 mM Tris, pH 7.4; 50 mM NaCl, 1 mM EDTA)) and

centrifuged (25,000 RPM for 2.5 hours at 4° C in a Beckman SW28 Large Ultracentrifuge Rotor) to concentrate the VLPs. The viral pellets were resuspended in 1 mL of STE buffer, pooled, and centrifuged (1 hour at 41,000 RPM at 4° C in a Beckman SW41 Small Ultracentrifuge Rotor). The final VLP pellet was gently rinsed with 100 μ L STE buffer, resuspended in 30 μ L STE, and dialyzed in 1 L STE buffer for 2 hours in a 50 μ L micro equilibrium dialyzer (10,000 MWCO / Harvard Apparatus) to remove excess sucrose from the preparation. The dialyzed solutions were gently centrifuged (5,000 RPM for 5 min in a microcentrifuge at 4° C) with the supernatants containing the purified VLPs used for freezing and imaging. The presence of VLPs at specific stages of the protocol was evaluated by SDS-PAGE and western blot with α -CA, α -MA, and α -Env antibodies.

Electron cryotomography. Solutions of the purified HIV-1 VLPs were flash-frozen onto glow-discharged Quantifoil grids (Quantifoil, Germany) in liquid ethane using a Vitrobot (FEI, The Netherlands). 10 nm colloidal gold was both combined with the viral solutions and applied separately on the grids before freezing.

All images were captured on the GIF CCD (Gatan) using a slit width of 20 eV, a defocus range of 4–8 μ m, and CCD pixel size of 0.46 or 0.56 nm on the specimen. Tilt series were collected from approximately -70° to $+70^\circ$ with 1° and 2° tilt steps automatically using the predictive UCSF tomography package [43].

Analysis of viral particles. Tomographic reconstructions were performed using the IMOD package, images were binned twofold within IMOD [35]. Individual immature VLPs were selected manually from the completed tomograms and were denoised by nonlinear anisotropic diffusion as implemented in the BSOFIT suite [36, 44]. Radial

density profiles were generated by sampling spherical shells of the tomograms and plotting the density per unit area as a function of radius. Measurements of the domains of Gag were made from the tomograms and the radial density profiles. Within the tomograms, central Z slices were selected and viewed and the width of each domain was measured. From the radial density profiles, the central slices were examined and the thicknesses of the domains were measured from the point halfway along the rising edge to the point halfway along the falling edge of the density. Surface projections were created by sampling the density in the tomogram along vectors normal to a triangle mesh surface of spherical shape, then assigning to each vertex on the surface the summed density along the vector at that point. To locate the unit cells, the points on the projected surfaces having the lowest values within a specified radius were selected. Those points were then labeled with the standard deviation of the distance to their six nearest neighbors, as a measure of the local degree of order in the hexagonal lattice. Amira extension modules created within our lab executed the preceding functions. For unit cell averaging, the set of extrema on the projected surface layers having the least variation in the distance to their neighbors was selected. For each of the selected points, a local coordinate system was established comprising the normal vector to the surface (the Z axis), the vector from the point to its nearest neighbor (the X axis), and their cross product (the Y axis). The entire volume containing the VLP was then rotated into alignment with the global axes and translated so as to superimpose all of the selected surface extrema.

Acknowledgements

This work was supported in part by NIH Grant PO1 GM66521 to WIS and GJJ, NIH Grant 1 F32 GM075543-01 to ERW, the Beckman Institute at Caltech, and gifts to Caltech from the Ralph M. Parsons Foundation, the Agouron Institute, and the Gordon and Betty Moore Foundation.

References

1. Freed, E.O., *HIV-1 gag proteins: diverse functions in the virus life cycle*. Virology, 1998. **251**(1): p. 1-15.
2. Fuller, S.D., et al., *Cryo-electron microscopy reveals ordered domains in the immature HIV-1 particle*. Curr Biol, 1997. **7**(10): p. 729-38.
3. Wilk, T., et al., *Organization of immature human immunodeficiency virus type 1*. J Virol, 2001. **75**(2): p. 759-71.
4. Briggs, J.A., et al., *The mechanism of HIV-1 core assembly: insights from three-dimensional reconstructions of authentic virions*. Structure, 2006. **14**(1): p. 15-20.
5. Briggs, J.A., et al., *The stoichiometry of Gag protein in HIV-1*. Nat Struct Mol Biol, 2004. **11**(7): p. 672-5.
6. Ohagen, A., et al., *The morphology of the immature HIV-1 virion*. Virology, 1997. **228**(1): p. 112-4.
7. Alfadhli, A., et al., *Analysis of human immunodeficiency virus type 1 Gag dimerization-induced assembly*. J Virol, 2005. **79**(23): p. 14498-506.

8. Ako-Adjei, D., M.C. Johnson, and V.M. Vogt, *The retroviral capsid domain dictates virion size, morphology, and coassembly of gag into virus-like particles*. J Virol, 2005. **79**(21): p. 13463-72.
9. Yamashita, M. and M. Emerman, *Capsid is a dominant determinant of retrovirus infectivity in nondividing cells*. J Virol, 2004. **78**(11): p. 5670-8.
10. McDermott, J., et al., *Structural analysis of human immunodeficiency virus type 1 Gag protein interactions, using cysteine-specific reagents*. J Virol, 1996. **70**(8): p. 5106-14.
11. Krausslich, H.G., et al., *The spacer peptide between human immunodeficiency virus capsid and nucleocapsid proteins is essential for ordered assembly and viral infectivity*. J Virol, 1995. **69**(6): p. 3407-19.
12. Borsetti, A., A. Ohagen, and H.G. Gottlinger, *The C-terminal half of the human immunodeficiency virus type 1 Gag precursor is sufficient for efficient particle assembly*. J Virol, 1998. **72**(11): p. 9313-7.
13. Reil, H., et al., *Efficient HIV-1 replication can occur in the absence of the viral matrix protein*. EMBO J, 1998. **17**(9): p. 2699-708.
14. Forster, M.J., B. Mulloy, and M.V. Nermut, *Molecular modelling study of HIV p17gag (MA) protein shell utilising data from electron microscopy and X-ray crystallography*. J Mol Biol, 2000. **298**(5): p. 841-57.
15. Morikawa, Y., et al., *Roles of matrix, p2, and N-terminal myristoylation in human immunodeficiency virus type 1 Gag assembly*. J Virol, 2000. **74**(1): p. 16-23.

16. Hill, C.P., et al., *Crystal structures of the trimeric human immunodeficiency virus type 1 matrix protein: implications for membrane association and assembly*. Proc Natl Acad Sci USA, 1996. **93**(7): p. 3099-104.
17. Massiah, M.A., et al., *Three-dimensional structure of the human immunodeficiency virus type 1 matrix protein*. J Mol Biol, 1994. **244**(2): p. 198-223.
18. Massiah, M.A., et al., *Comparison of the NMR and X-ray structures of the HIV-1 matrix protein: evidence for conformational changes during viral assembly*. Protein Sci, 1996. **5**(12): p. 2391-8.
19. Huseby, D., et al., *Assembly of human immunodeficiency virus precursor gag proteins*. J Biol Chem, 2005. **280**(18): p. 17664-70.
20. Benjamin, J., et al., *Three-dimensional structure of HIV-1 virus-like particles by electron cryotomography*. J Mol Biol, 2005. **346**(2): p. 577-88.
21. Lanman, J., et al., *Key interactions in HIV-1 maturation identified by hydrogen-deuterium exchange*. Nat Struct Mol Biol, 2004. **11**(7): p. 676-7.
22. Mayo, K., et al., *Retrovirus capsid protein assembly arrangements*. J Mol Biol, 2003. **325**(1): p. 225-37.
23. Li, S., et al., *Image reconstructions of helical assemblies of the HIV-1 CA protein*. Nature, 2000. **407**(6802): p. 409-13.
24. Barklis, E., et al., *Organization of HIV-1 capsid proteins on a lipid monolayer*. J Biol Chem, 1998. **273**(13): p. 7177-80.
25. Welker, R., et al., *Biochemical and structural analysis of isolated mature cores of human immunodeficiency virus type 1*. J Virol, 2000. **74**(3): p. 1168-77.

26. Ganser-Pornillos, B.K., et al., *Assembly properties of the human immunodeficiency virus type 1 CA protein*. J Virol, 2004. **78**(5): p. 2545-52.
27. von Schwedler, U.K., et al., *Functional surfaces of the human immunodeficiency virus type 1 capsid protein*. J Virol, 2003. **77**(9): p. 5439-50.
28. Lanman, J., et al., *Identification of novel interactions in HIV-1 capsid protein assembly by high-resolution mass spectrometry*. J Mol Biol, 2003. **325**(4): p. 759-72.
29. Mortuza, G.B., et al., *High-resolution structure of a retroviral capsid hexameric amino-terminal domain*. Nature, 2004. **431**(7007): p. 481-5.
30. Tang, C., Y. Ndassa, and M.F. Summers, *Structure of the N-terminal 283-residue fragment of the immature HIV-1 Gag polyprotein*. Nat Struct Biol, 2002. **9**(7): p. 537-43.
31. von Schwedler, U.K., et al., *Proteolytic refolding of the HIV-1 capsid protein amino-terminus facilitates viral core assembly*. EMBO J, 1998. **17**(6): p. 1555-68.
32. Nandhagopal, N., et al., *Dimeric rous sarcoma virus capsid protein structure relevant to immature Gag assembly*. J Mol Biol, 2004. **335**(1): p. 275-82.
33. Briggs, J.A., et al., *Cryo-electron microscopy reveals conserved and divergent features of gag packing in immature particles of Rous sarcoma virus and human immunodeficiency virus*. J Mol Biol, 2006. **355**(1): p. 157-68.
34. Nermut, M.V., et al., *Further evidence for hexagonal organization of HIV gag protein in prebudding assemblies and immature virus-like particles*. J Struct Biol, 1998. **123**(2): p. 143-9.

35. Kremer, J.R., D.N. Mastronarde, and J.R. McIntosh, *Computer visualization of three-dimensional image data using IMOD*. J Struct Biol, 1996. **116**(1): p. 71-6.
36. Frangakis, A.S. and R. Hegerl, *Noise reduction in electron tomographic reconstructions using nonlinear anisotropic diffusion*. J Struct Biol, 2001. **135**(3): p. 239-50.
37. Caspar, D.L. and A. Klug, *Physical principles in the construction of regular viruses*. Cold Spring Harb Symp Quant Biol, 1962. **27**: p. 1-24.
38. Accola, M.A., B. Strack, and H.G. Gottlinger, *Efficient particle production by minimal Gag constructs which retain the carboxy-terminal domain of human immunodeficiency virus type 1 capsid-p2 and a late assembly domain*. J Virol, 2000. **74**(12): p. 5395-402.
39. Nermut, M.V., et al., *Fullerene-like organization of HIV gag-protein shell in virus-like particles produced by recombinant baculovirus*. Virology, 1994. **198**(1): p. 288-96.
40. Accola, M.A., S. Hoglund, and H.G. Gottlinger, *A putative alpha-helical structure which overlaps the capsid-p2 boundary in the human immunodeficiency virus type 1 Gag precursor is crucial for viral particle assembly*. J Virol, 1998. **72**(3): p. 2072-8.
41. Liang, C., et al., *Characterization of a putative alpha-helix across the capsid-SP1 boundary that is critical for the multimerization of human immunodeficiency virus type 1 gag*. J Virol, 2002. **76**(22): p. 11729-37.

42. Morellet, N., et al., *Helical structure determined by NMR of the HIV-1 (345-392)Gag sequence, surrounding p2: implications for particle assembly and RNA packaging*. Protein Sci, 2005. **14**(2): p. 375-86.
43. Zheng, Q.S., et al., *An improved strategy for automated electron microscopic tomography*. J Struct Biol, 2004. **147**(2): p. 91-101.
44. Heymann, J.B., *Bsoft: image and molecular processing in electron microscopy*. J Struct Biol, 2001. **133**(2-3): p. 156-69.

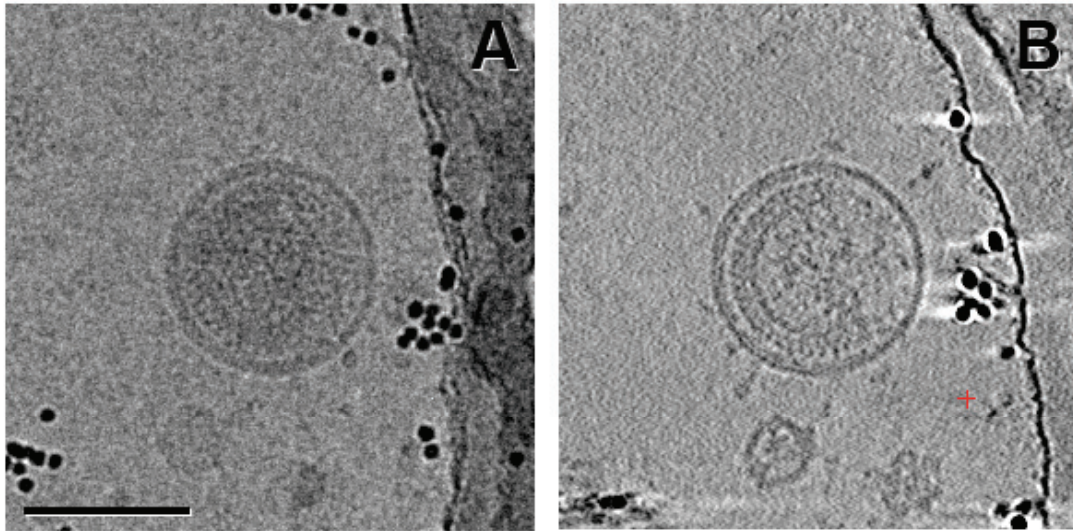
Figures

Figure 3-1. Primary data and tomogram.

(A) The central image from a tilt series of an immature HIV-1 VLP. (B) A 5.6 nm slice through the middle of the reconstruction. Scale bar 100 nm.

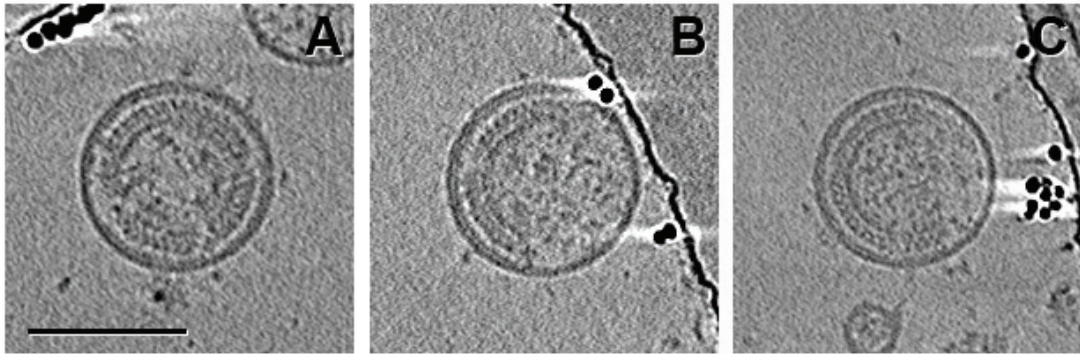


Figure 3-2. Gag sectors and associated membrane structure.

11 nm slices through tomographic reconstructions. Scale bar 100 nm.

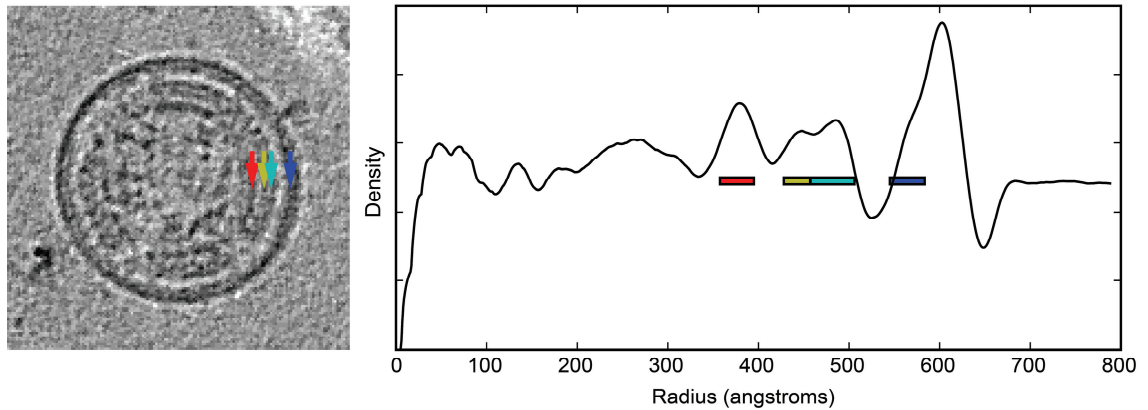


Figure 3-3. Immature HIV-1 VLP and radial density plot.

At left: 11 nm slice through a three-dimensional reconstruction of an immature HIV-1 VLP. The arrows denote the layers of density associated with the Gag domains NC, CA CTD, CA NTD, and MA (left to right). At right: radial density plot of the virion. Bars indicate layers projected onto surfaces in Figure 3-4.

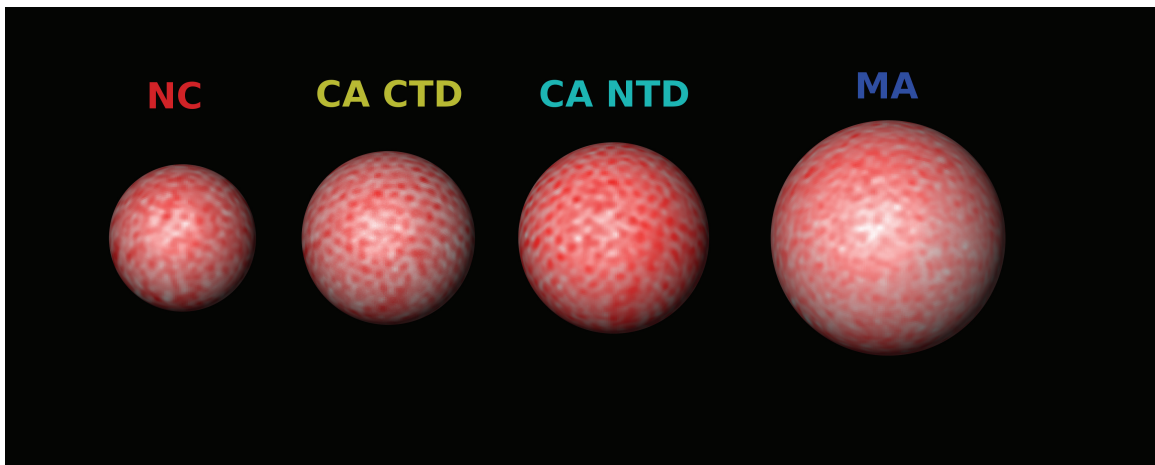


Figure 3-4. Gag shell surface projections of an immature HIV-1 VLP.

One representative immature viruse was used to display the protein densities associated with each layer of the Gag polyprotein (left to right: NC, CA CTD, CA NTD, MA). It was observed that only the CA layers contained regular patterning attributed to the protein densities. Red is more dense.

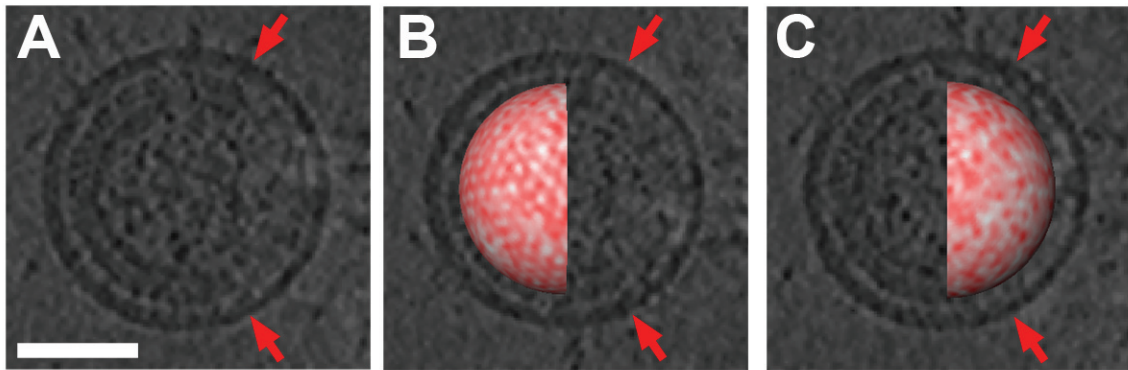


Figure 3-5. Ordering of the Gag polyprotein within the immature HIV-1 VLP.

One representative reconstructed immature VLP in which the internal organization of the Gag polyprotein is observed. In A, the discontinuous nature of the layers of the Gag polyprotein is evident (arrows mark the boundaries of the ordered region). B and C, are the surface projections of the CA (capsid) layer in which the regular patterning is only observed within the ordered region shown in A. Scale bar 50 nm.

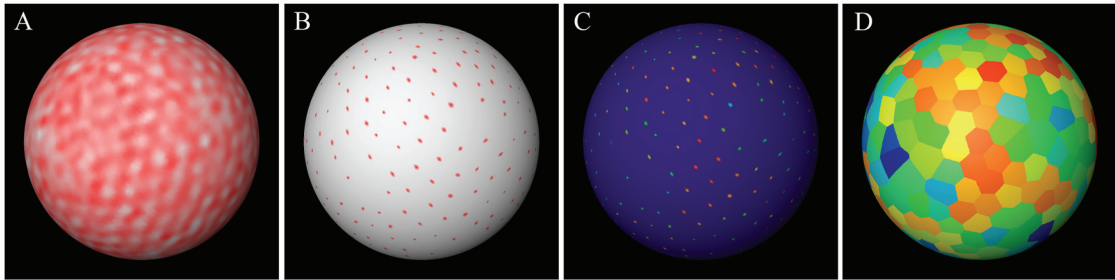


Figure 3-6. Analysis of the surface projection of the CA protein within one immature HIV-1 VLP.

(A) Surface projection from the densities of the CA protein layer of Gag. (B) The points of lowest density selected from the surface projection. (C) The local extrema color coded to denote the local order associated with each point (red, greatest degree of order; light blue, least degree of order). (D) Surface area associated with each point (color code is same as C).

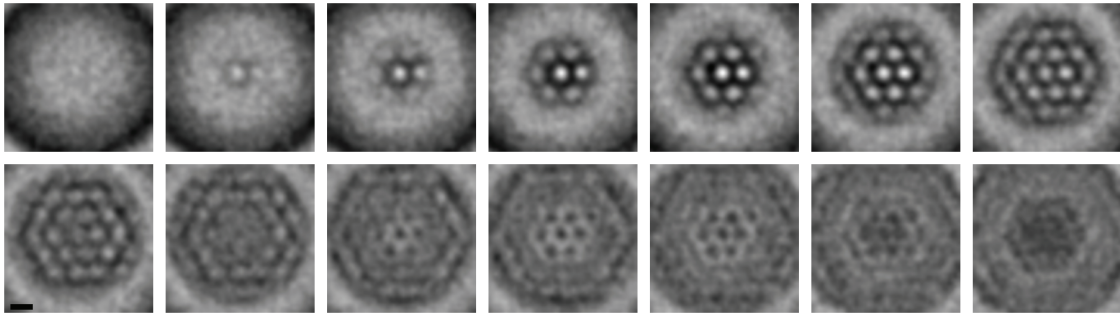


Figure 3-7. Montage of the averaged unit cell of an immature HIV-1

VLP.

Slices are 1.12 nm thick. Radial positions, from left to right, top to bottom: 526.4, 515.2, 504.0, 492.8, 481.6, 470.4, 459.2, 448.0, 436.8, 425.6, 414.4, 403.2, 392.0, 380.8.

Scale bar 8 nm.

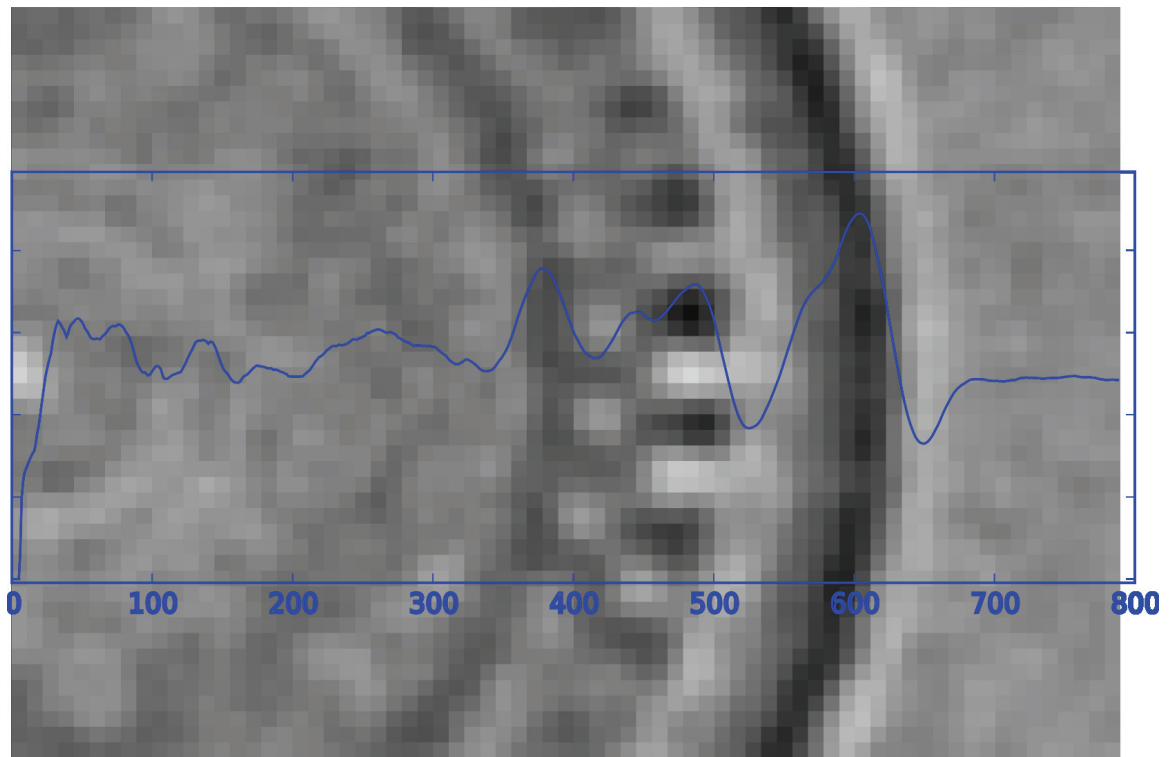


Figure 3-8. Averaged unit cell with radial density plot.

1.12 nm slice through Z axis. Peaks were aligned to position near center of image.

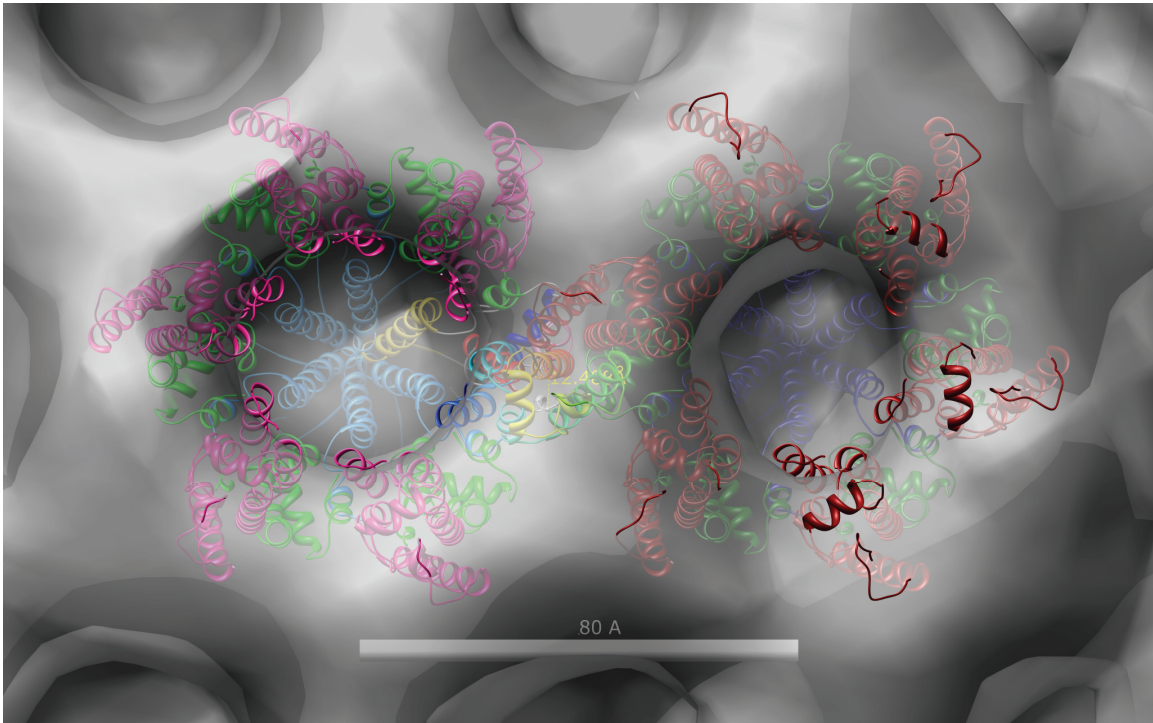


Figure 3-9. Top view of Gag components docked into the averaged density.

CA NTD is red, CA CTD is green, and SP1 is blue.

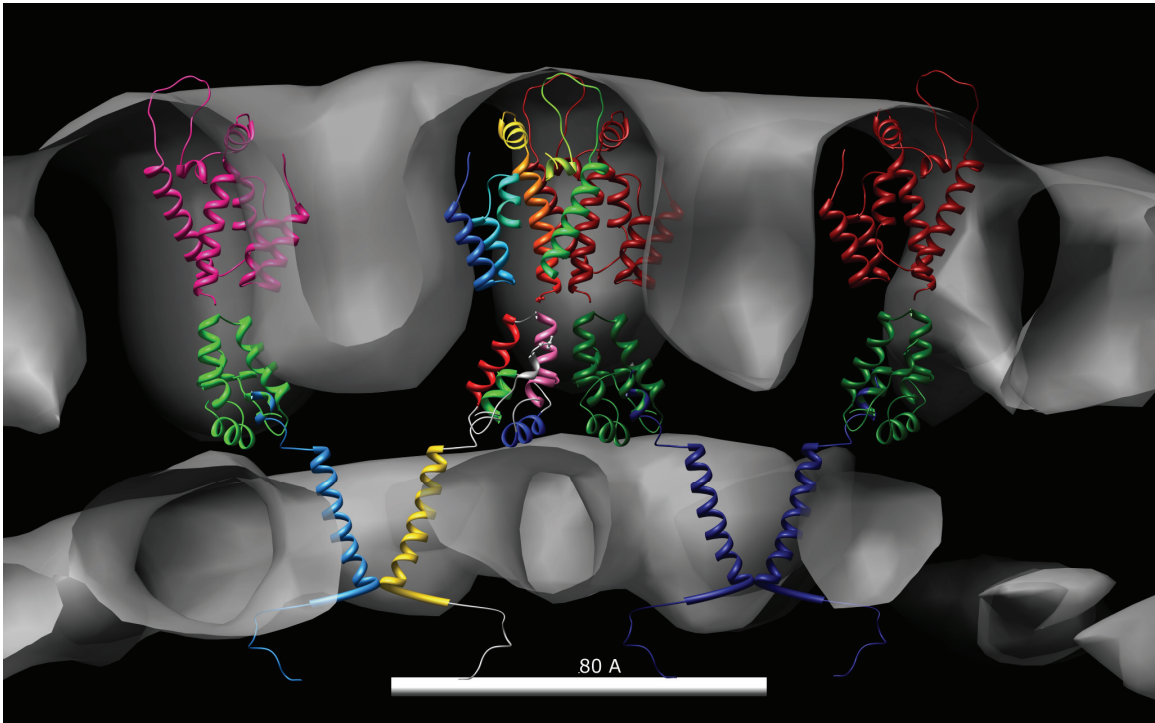


Figure 3-10. Side view of Gag components docked into the averaged density.

Only two monomers from each hexamer are displayed, for clarity.

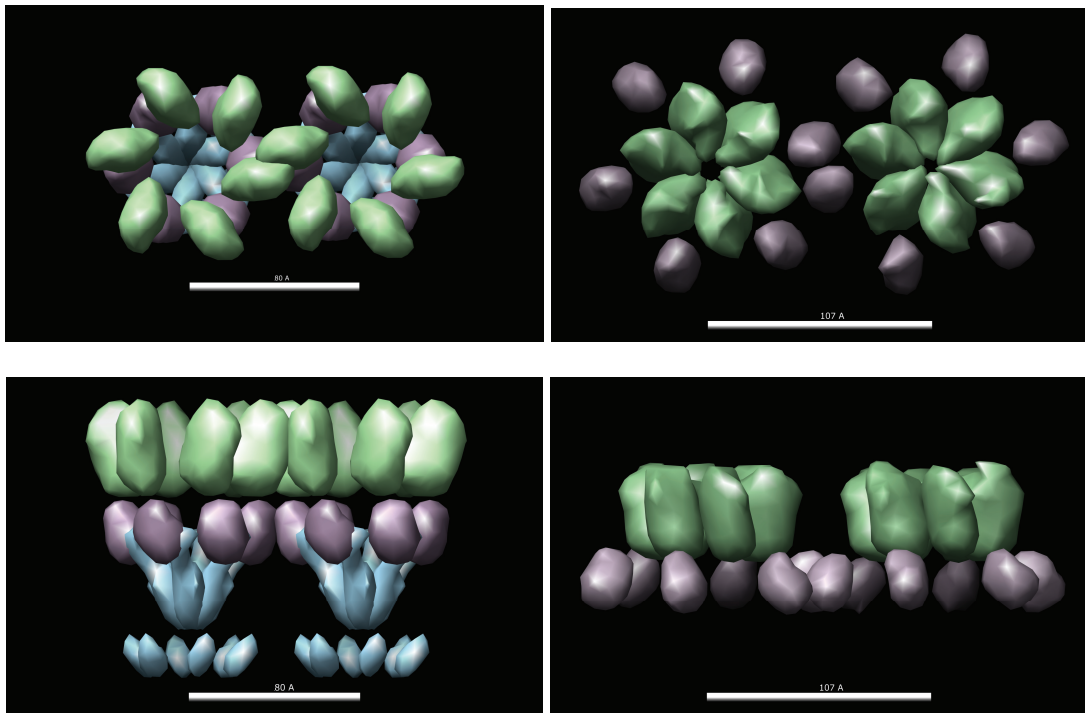


Figure 3-11. Comparison of immature and mature lattices.

Left: Top and side views of immature lattice model. CA NTD is green, CA CTD mauve, and SP1 blue.

Right: Top and side views of mature CA model. Colors are the same as in the left panels.

Appendix A: A “flip-flop” rotation stage for routine dual-axis electron cryotomography

Cristina V. Iancu^{†1}, Elizabeth R. Wright^{†1}, Jordan Benjamin¹, William F. Tivol¹,
D. Prabha Dias¹, Gavin E. Murphy¹, Robert C. Morrison², J. Bernard Heymann³, and
Grant J. Jensen^{1*}

¹Division of Biology, California Institute of Technology, 1200 E. California Blvd.,
Pasadena, CA 91125

²Gatan (UK), 25 Nuffield Way, Abingdon Oxon OX14 1RL UK

³Current address: Laboratory of Structural Biology Research, National Institute of
Arthritis, Musculoskeletal and Skin Diseases, National Institutes of Health, Bethesda,
Maryland 20892

[†]These authors contributed equally

*To whom correspondence should be addressed: jensen@caltech.edu, 626-395-8827
(phone) 626-395-5730 (fax)

Published in *Journal of Structural Biology* Volume 151, Issue 3 , September 2005, Pages
288–297

doi:10.1016/j.jsb.2005.07.004

Received 3 March 2005; revised 6 June 2005; accepted 6 July 2005. Available online 11
August 2005.

Abstract

Electron cryotomography can be used to solve the three-dimensional structures of individual large macromolecules, assemblies, and even small intact cells to medium (~4–8 nm) resolution in a near-native state, but restrictions in the range of accessible views are a major limitation. Here we report on the design, characterization, and demonstration of a new “flip-flop” rotation stage that allows facile and routine collection of two orthogonal tilt-series of cryosamples. Single- and dual-axis tomograms of a variety of samples are compared to illustrate qualitatively the improvement produced by inclusion of the second tilt-series. Exact quantitative expressions are derived for the volume of the remaining “missing pyramid” in reciprocal space. When orthogonal tilt-series are recorded to $\pm 65^\circ$ in each direction, as this new cryostage permits, only 11% of reciprocal space is left unmeasured. The tomograms suggest that further improvement could be realized, however, through better software to align and merge dual-axis tilt-series of cryosamples.

Keywords:

tomography, electron microscopy, cryoEM, dual-axis, cryoholder, missing wedge

Introduction

The highest resolution technique currently available for three-dimensional structural studies of unique objects is electron tomography, in which a specimen is imaged multiple times in an electron microscope (EM) while being incrementally tilted through a range of views. The method has the potential to couple the exquisite spatial resolution of modern electron microscopes, which in some cases can now be even sub-Angstrom [1, 2], with three-dimensional structure determination through a variety of reconstruction algorithms. Thus electron tomography is emerging as a powerful new technique in both materials and life science research [3-5].

There are several practical limitations for biological samples, however, including radiation damage and the typically restricted range of tilt-angles from which images can be recorded. The tilt-angle limitation arises because most EM samples are thin disks of material approximately 3 mm in diameter and ~30–500 nm thick, and as these samples are incrementally tilted, the depth of material the electron beam must pass through increases as one over the cosine of the tilt-angle. At high tilt-angles, most samples become prohibitively thick. In addition, the edges of standard sample holders block the electron beam at high tilt-angles. Because each projection image provides the amplitudes and phases of just one central section of the specimen's three-dimensional Fourier transform, this data collection constraint translates into a "missing wedge" of information in reciprocal space.

Early in the development of electron tomography, this missing wedge problem was significantly reduced for room temperature samples by collecting two tilt-series

about orthogonal axes, thus reducing the missing “wedge” to just a missing “pyramid” [6, 7]. This procedure was relatively straightforward because room-temperature samples could be removed from the microscope and the specimen holder, manually rotated 90°, and replaced for collection of the second tilt-series without much challenge. Despite complications due to the shrinking and warping of plastic-embedded sections during data collection, dramatic improvements in the quality of the tomograms were realized by inclusion of the second tilt-series, and dual-axis tomography became the recognized standard, best practice [8].

Concurrently, various improvements in microscope technology and sample preparation made it possible to image biological materials in a life-like, “frozen-hydrated” state. Such samples are produced by either plunge-freezing thin films [9] or cryosectioning high-pressure-frozen bulk samples [10, 11]. These developments have made it possible to study the three-dimensional structures of unique objects including even whole cells *in their near-native states* [5], and strong efforts are now being invested to maximize resolution and interpretability.

One of the challenges has been the development of a cryostage that allowed facile collection of two perpendicular tilt-series. Because frozen-hydrated samples must always be kept at very low temperatures (standard practice is to maintain better than -160°C) to prevent ice crystallization, they cannot be simply removed from the microscope, rotated 90° and replaced unless it is done under cold nitrogen gas. This is awkward at best, and is not routinely successful because of the difficulty of fine grid manipulations under these conditions and the frequency of grid contamination. In an attempt to allow grid rotation within the microscope column, the Martinsreid group in collaboration with Gatan

modified a standard cryostage and then used it to collect dual-axis tilt-series of at least one frozen-hydrated sample [12], but the stage was not described and seems not to have been used in recent work from the same group [13-16]. A motor-driven tilt-rotation holder (the Gatan CT3500RT) has also been developed for standard side-entry goniometers, but no results of its use in this context are yet available. Here we report on the design, characterization, and experimental benefit of a new “flip-flop” cryorotation stage that allows routine dual-axis cryotomography in the FEI Polara transmission electron microscope, and identify new image processing challenges this type of data presents.

The flip-flop rotation stage

The “flip-flop” rotation stage was an experimental product designed and built by Gatan UK (RCM) in consultation with Caltech (GJJ) and others. The prototype was then tested and characterized experimentally at Caltech, as reported below. The stage is a derivative of the new cartridge-based, multispecimen stage system implemented to accommodate liquid-helium sample-cooling in the new Polara series of TEMs from the FEI Company. Frozen-hydrated grids are first clamped into cartridges, and then up to six cartridges at a time are loaded into a multispecimen holder. The holder is sealed, evacuated, mounted on the microscope column, and then opened to the column vacuum. Individual cartridges are picked up with an insertion tool and introduced into the column proper, where they are threaded onto a permanently-inserted specimen rod.

The flip-flop rotation stage consists of modified cartridges and a special rotation tool in the multispecimen holder. The modified cartridges house an inner, rotationally

mobile cup into which the grid is clamped (Fig. A-1A). This mobile cup has two protrusions extending out beyond the edge of the cartridge in opposite directions. The rotation tool is like a two-car garage, in that it can house cartridges in either side, but unlike a garage, it moves over and around the cartridges while they remain fixed (Fig. A-1B). When a cartridge is docked in the multispecimen holder, the rotation tool can be pushed over the cartridge (Fig. A-1C) in such a way that it catches one of the protrusions on the inner cup and causes the cup to rotate 90°. Depending on which docking position the cartridge occupies in the multispecimen holder, pushing the rotation tool causes the cup to be rotated into either the “flip” position or the “flop” position, 90° away.

Collection of a dual-axis tilt-series proceeds as follows. A cryosample is clamped into the cup of a flip-flop cartridge and loaded into the multispecimen holder. The multispecimen holder is mounted onto the microscope, the flip-flop cartridge is moved to position 5 in the multispecimen holder, and the rotation tool is pushed over the cartridge to ensure the cup begins in the “flip” position. Then the cartridge is introduced into the column, threaded onto the specimen rod, and a suitable specimen is located and imaged through one tilt-series. The cartridge is then retrieved from the column and placed into position 6 of the multispecimen holder, all the while protected by the microscope’s column vacuum. The rotation tool is once again pushed over the cartridge, this time rotating the cup and grid into the “flop” position. The cartridge is again threaded onto the specimen rod, the object of interest is re-located, and the second, orthogonal tilt-series is recorded.

Technical characterization

One of the challenges for any cryostage is to minimize thermal drift. The grid must be in good, uniform, thermal contact with the cryoholder. There was concern that the rotating cup in the flip-flop cartridge would make poor contact with the rest of the cartridge and cause drift. Fortunately, no more drift was observed with the flip-flop cartridges than with regular cartridges, and both are impressively stable. A simple test grid with colloidal gold on carbon was allowed to equilibrate in the column at liquid nitrogen temperature for several hours. The drift rate was then measured at one-minute intervals for five minutes, manifesting displacements of 0.7, 0.8, 0.4, 0.3, and 0.3 nm (average 0.5 nm per minute).

Next, the actual rotation realized and the vertical displacement of the grid effected by the rotation were measured by setting eucentric height, recording a nominally untilted image, rotating the sample with the flip-flop mechanism, refinding the target region, resetting eucentric height, and recording a second nominally untilted image. In nine trials involving three different flip-flop cartridges, the rotation angle ranged from 87.0° to 88.8°, with an average of 87.7° and a standard deviation of 0.6°. The vertical displacements ranged from 0.15 to 2.65 μm , with an average of 1.07 μm and a standard deviation of 0.73 μm .

The dose needed to re-center the target region under the beam after rotation can be reduced to arbitrarily low values, including zero. The grid coordinate system can be re-oriented by imaging markers around the target region, for instance, which allows objects to be re-centered simply by moving to their new coordinates. Fine re-centering can be done by finding “focus” spots close to but on either side of the target. More

routinely, however, we have re-centered targets directly with low dose, low magnification images that deliver less than 1 electron/Å². All other preparative steps can be performed on peripheral areas, including resetting the eucentric height and re-centering the energy filter slit if necessary.

Qualitative comparisons of single- versus dual-axis tomograms

Using the flip-flop stage, dual-axis tomograms of a variety of representative frozen-hydrated specimens were produced including whole bacterial cells, virus-like-particles, bacterial carboxysomes, and solutions of purified proteins. The whole cell chosen was the bacterium *Mesoplasma florum*, a very small and simple cell that inhabits citrus plants. *M. florum* cells were plunge-frozen on Quantifoil grids into liquid ethane using an FEI Vitrobot. A tilt-series was collected from -66° to $+62^\circ$ with a 1° tilt step, and then the grid was rotated $\sim 90^\circ$ about the z-axis and a second tilt-series was collected from -62° to $+66^\circ$. The total dose used for each tilt-series was $60 \text{ e}^-/\text{\AA}^2$, the defocus was $\sim 15 \text{ }\mu\text{m}$ (first CTF zero at $\sim 1/5.5 \text{ nm}$), and the magnification was set such that each CCD pixel represented 1.34 nm on the specimen. All images here and below were energy-filtered (slit width of 20 eV) and recorded on a 300 kV FEG “G2 Polara” TEM with the sample cooled by liquid nitrogen to $\sim 82 \text{ K}$.

Three-dimensional tomograms of the first and second tilt-series were calculated and combined using the IMOD package [7], and then the individual and combined tomograms were denoised by 40 rounds of nonlinear anisotropic diffusion [17]. Fig. A-2 shows slices through the centers of three tomograms of a *M. florum* cell: one from each

of the two independent tilt-series and one from their combination. All the XY slices (left column) are comparably well-defined, and many individual large protein complexes are resolved within the cell. Nevertheless, while the tomogram from the first tilt-series (top row) shows some detail in the XZ slice (albeit smeared in the Z direction), the YZ slice is quite poor. The tomogram from the second tilt-series (middle row) is the opposite, showing some detail in the YZ but not the XZ slice. Only in the dual-axis tomogram (bottom row) are particles resolved in all three directions. The residual missing pyramid of data is still evident, though, in the membrane's lack of closure over the top and bottom surfaces of the cell.

Next, the impact of including a second tilt-series was observed on a purified, HIV-1 virus-like particle (VLP). HIV-1 is an enveloped retrovirus whose outer layer consists of a lipid bilayer and a matrix protein shell. In these VLPs, the Env protein was removed to eliminate infectivity, so no surface “spikes” are seen. Inside the lipid/matrix layer there is a typically conical capsid shell [18]. An HIV-1 VLP was plunge-frozen, imaged through orthogonal tilt-series, reconstructed, and denoised as described above for *M. florum*, except that the tilt-series were from -57° to $+60^\circ$ and -60° to $+60^\circ$ with a 3° tilt step, the defocus was $\sim 16 \mu\text{m}$ (first CTF zero at $\sim 1/5.6 \text{ nm}$), the image pixel size was 1.34 nm , the total dose was $240 \text{ e}^-/\text{\AA}^2$ and only 20 rounds of denoising were performed (Fig. A-3). Although still not complete, the dual-axis tomogram resolved significantly more of the viral layers' morphologies than either single-axis tomogram. This was made particularly obvious in the three-dimensional renderings of the viral envelope isosurface. The improved but still imperfect point-spread-function was also evidenced by the gold

fiducial, which appeared nicely round in the XY plane, but still elongated in the Z direction.

In the two previous cases (MF and HIV-1), comparisons were made between single-axis tomograms and their dual-axis combinations. While this eliminated structural differences between the compared objects, the dual-axis tomograms unfairly profited from twice the dose. Two additional samples were therefore tested where single- and dual-axis tomograms could be calculated from separate but very similar objects, using the same *total* dose. The first such sample was purified carboxysomes from the prokaryote *Synechococcus species*. Carboxysomes are ~100 nm microcompartments consisting of a proteinaceous shell surrounding many tens of copies of the enzyme ribulose 1,5-bisphosphate carboxylase/oxygenase (RuBisCO), as well as other, smaller enzymes [19]. Carboxysomes were plunge-frozen and imaged through either a single tilt-series or through two orthogonal tilt-series, in every case to $\pm 64^\circ$. The dose (total) was $120 \text{ e}^-/\text{\AA}^2$, the tilt step was 2° , the defocus was $\sim 10 \text{ }\mu\text{m}$ (first CTF zero at $\sim 1/4.5 \text{ nm}$), the image pixel size was 6.7 \AA , and 200 rounds of denoising were performed. The protein shell and many individual RuBisCO molecules can be resolved in the tomograms (Fig. A-4). Again the resolution of the dual-axis tomogram is clearly more isotropic, but still not as good in the Z direction as in the X or Y directions.

Finally, several different purified protein complexes were imaged, including the molluscan hemocyanin from *Megathura crenulata*. This hemocyanin is an $\sim 8 \text{ MDa}$ complex that forms a double-layered, hollow barrel approximately 30 nm in diameter and 35 nm in length. Hemocyanin was plunge-frozen and imaged through single- (-66° to 63°) and dual-axis (-66° to 63° first axis, $\pm 63^\circ$ second) tilt-series with an angular step

size of 3° , a defocus of $8\ \mu\text{m}$ (first CTF zero at $\sim 1/4.0\ \text{nm}$), and a pixel size of $6.7\ \text{\AA}$. Single- and dual-axis tomograms were recorded with the same total dose ($110\ \text{e}^-/\text{\AA}^2$) from different holes in the same square of a single grid with as similar ice thicknesses and other characteristics as possible. Three-dimensional renderings of particles that froze with their long axes in the plane of the sample and either parallel or perpendicular to the tilt-axis, and with their long axis perpendicular to the sample (“vertical”) are shown (Fig. A-5) after 20 rounds of denoising and alignment to a reference [20] using the BSOFIT software package [21]. The particles were not symmetrized before rendering. While the dual-axis tomograms are perhaps just slightly better, the improvement was more modest than expected. As discussed below, this is probably due to non-optimal merging of the two tilt-series, which was most challenging in this case of isolated protein complexes.

Novel data processing challenges

The IMOD software package [7] was used to produce all these tomograms. The procedure begins by calculating two independent, real-space tomograms from the two tilt-series, and then the second tomogram is transformed into approximate alignment with the first using the coordinates of corresponding gold fiducials. The second tomogram is then sampled with an array of subvolumes (“patches”), and each patch is cross-correlated with a corresponding patch from the first. A map of the resulting displacement vectors is fit to a smooth function, and a new, “dewarped” version of the second tomogram is calculated. The dewarped second and the first tomograms are Fourier transformed and averaged in reciprocal space, and then a final, dual-axis tomogram is produced by inverse transformation. While these algorithms have been used and refined extensively to merge

tilt-series of plastic sections, the data from cryosamples can be different in important ways: (1) the gold beads are typically distributed throughout the sample rather than just on the top and bottom surfaces; (2) no shrinkage or distortion during data collection is expected; (3) images are more noisy due to the stringent dose limitations; and (4) contrasty objects can be more sparse, as, for instance, the isolated hemocyanin molecules were against the feature-less background of vitreous ice.

These differences introduced novel image processing problems. First, while no evidence for shrinking or warping was seen, a small fraction of the gold fiducials used to align the two tilt-series moved by up to several nm during acquisition of the data. Because no reproducible pattern was recognized, this mismatch is likely caused by the fiducials diffusing randomly within the vitreous ice. Thus their movements were sometimes significant, but not correlated with movements of neighboring objects of interest (unlike fiducials on the surface of a shrinking plastic section).

Next, the strategy of mapping local distortions between the first and second tomograms seemed non-ideal in this context, especially for the isolated protein complexes. In the case of hemocyanin, for instance, the best results were obtained when exceedingly large patches and high “warping residual limits” were used. This is probably because small patches sometimes contained only vitreous ice, and were therefore nearly featureless, and yielded misleading distortion vectors. To solve this problem, IMOD already allows users to identify specific regions to be included in the dewarping procedure, and discard anomalous vectors, but superior results would likely be obtained by using each reconstructed macromolecular complex as a “patch.” An iterative refinement procedure in which all the images from both tilt-series were re-aligned to

projections of the reconstructed object of interest (as in standard “single particle analysis,” see [22], might be best of all. In principle, the structure of cryosamples should not be changing during data collection, and thus no dewarping at all should be necessary. Slight changes in the electron optics, non-idealities of the tilt-axis, and distortions caused by the energy filter are still probably introducing slight distortions which can and should be corrected.

Finally, it was observed that in the three-dimensional power spectra of the final tomograms, the average intensity in regions where data was combined from both tilt-series was lower than the average intensity in regions covered by just one or the other (Fig. A-6a). The algorithm used in IMOD to merge tilt-series was a simple average: in regions of reciprocal space where there was data from both or neither tilt-series, the two values were simply averaged vectorially, whereas in regions where there was data from just one tilt-series, that single value was used. While this seems entirely reasonable, the reduced amplitudes in doubly-measured regions can be explained simply by the fact that the average length of two vectors is always larger than the length of their *vector* average, except in the rare case that their directions (phases) are identical. While this difference may not be large for well-aligned data with a high signal-to-noise ratio, it was apparent in these cryotomograms. D. Mastronarde therefore introduced an IMOD option to simply attenuate the amplitudes in the singly-measured regions to match those in the doubly-measured regions within shells of reciprocal space (Fig. A-6b). Whether this is the optimal procedure has yet to be explored.

Size of the missing pyramid in single- versus dual-axis data collection

The potential benefit of dual-axis tomography can be assessed quantitatively by calculating the percentage of reciprocal space covered by single- and dual-axis tilt-series. While isolated results of similar calculations already appear in the tomography literature, the formulas and their derivations do not to our knowledge, and because they involve principles of spherical trigonometry unfamiliar to most investigators in this field, they are presented here. In spherical trigonometry, lengths and areas are quantified in degrees and “spherical” degrees, respectively, and by “spherical polygon” is meant a region on the surface of a sphere whose borders are defined by planes passing through the sphere’s origin. The area of a spherical polygon in spherical degrees is equal to its angular excess; *i.e.*, the amount by which the sum of its angles exceeds that of an analogous polygon on a plane. For example, on a globe the spherical triangle formed by a segment of the equator and two meridians of longitude has an area equal to the angle between the meridians, since the angles between each meridian and the equator is 90° , and account by themselves for the sum of the three angles of a planar triangle.

Making the assumption that the flip-flop holder yields two tilt-series that are indeed orthogonal, but allowing different maximum tilt-angles in both the positive and negative direction for both tilt-axes, one can calculate the size of the missing pyramid using Fig. A-7. The view is down the direction of the electron beam, or Z axis, and the four large arcs (two splitting away from and rejoining the X axis and two splitting away from and rejoining the Y axis) represent the limits of the two tilt-series. Thus the first tilt-series (along X) is from α_{\min} to α_{\max} , and the second tilt-series (along Y) is from β_{\min} to β_{\max} . These arcs should be thought of as lying on the surface of a sphere in reciprocal

space, while the X and Y axes lie within an “equatorial” plane below, such that they do not intersect with the arcs except at the endpoints. Since the totality of information out to any specified resolution is a sphere, and since the solid angle of the missing pyramid is the same regardless of the sphere’s radius, the fraction of missing information is the ratio of the area of the spherical quadrilateral bounded by the planes of maximum tilts (shaded region) to the area of the full hemisphere, or 360 spherical degrees. The missing area is equal to its angular excess, or $(180^\circ - \theta^{++}) + (180^\circ - \theta^{+-}) + (180^\circ - \theta^{-+}) + (180^\circ - \theta^{--}) - 360^\circ$. Napier’s rules for right spherical triangles state that the cosine of one of the non-right angles is equal to the sine of the other non-right angle times the cosine of the opposite side length. Thus $\cos(\theta^{++}) = \sin(90^\circ - \alpha_{\max})\cos(\beta_{\max})$, or $\cos(\alpha_{\max})\cos(\beta_{\max})$. Similarly, $\cos(\theta^{+-}) = \cos(\alpha_{\min})\cos(\beta_{\max})$, $\cos(\theta^{-+}) = \cos(\alpha_{\min})\cos(\beta_{\min})$, and $\cos(\theta^{--}) = \cos(\alpha_{\max})\cos(\beta_{\min})$. Given α_{\min} , α_{\max} , β_{\min} , and β_{\max} , the percentage of missing information can be found by calculating the angles θ , and then the angular excess of the missing region. Note that the formulas are symmetric with respect to which angles are called α and β , which directions are called “max” and “min,” and give correct results at limiting values including the case of single-axis tilting.

Several key results are listed in Table A-1. In order to reduce the missing information to just 10% (an arbitrary example target) with single-axis tilting, $\pm 81^\circ$ must be obtained. This is of course fundamentally problematic, because thin films are 6.4 times thicker parallel to the electron beam at 81° than they are untilted. For dual-axis tilting, reducing the missing pyramid to 10% requires reaching just 67° , where the sample is only

2.6 times thicker. The flip-flop cartridges allow imaging to $\pm 65^\circ$, so that all but 11% of the data can be gathered for a thin sample.

Discussion

From this work we conclude that (1) the new flip-flop holder succeeds in making the collection of dual-axis tilt-series of cryosamples convenient and routine, (2) including the second tilt-series does result in more isotropic resolution as expected, but (3) further gains should be realizable through better software to merge the data. The flip-flop holder has been used to collect more than a hundred dual-axis tilt-series of various samples now, of which only a few examples were shown here. These demonstrated that inclusion of the second tilt-series clarified the morphology of membranes, protein shells, and individual protein complexes. We have since observed other cases where dual-axis tilting has proven critical, including one dramatic case where a key bacterial cytoskeletal filament was essentially invisible in the tomogram of the first tilt-series, but was clearly resolved in the second. Except for the 90° rotation, the two tilt-series were otherwise identical in defocus, etc., and of course radiation damage does not explain the difference, since the filament was seen in the second tilt-series but not the first. Instead, this filament exemplified how long, tubular features that lie perpendicular to the tilt-axis are nearly invisible to single-axis tomography.

Despite these encouraging improvements, the results also suggest that better methods for alignment and merging are needed. This study is the first attempt to our knowledge to merge dual-axis tilt-series of isolated macromolecules suspended in vitreous ice. Considering the range of views used in the hemocyanin tomograms, the

dual-axis tomograms theoretically profited from an additional 15% coverage of reciprocal space (72% for the single-axis tomograms, 87% for the dual). The gains experimentally realized in this particular case (as seen in Fig. A-5) were only modest. We attribute this to non-optimal alignment and merging, which should be improved by more customized software.

Finally, the cartridge-based specimen holder system was originally designed to allow samples to be cooled with liquid helium rather than liquid nitrogen, in hopes that radiation damage could be further slowed or restrained. One of the potential disadvantages of the flip-flop stage design was that the sample had to be warmed to approximately -190°C between tilt-series for rotation because the multispecimen holder is only nitrogen-cooled. Thus the potential advantages of helium-cooling would be lost mid-way. Disappointingly, this is no longer a concern. Only disadvantages have been observed for liquid helium-cooling in cryotomography, and we now routinely use only liquid nitrogen. As part of the present investigations, however, the effects of warming helium-cooled samples to -190°C for rotation in the multispecimen holder were extensively explored. While the results will be reported in full alongside related experiments evidencing phase transitions in vitreous ice (manuscript in preparation), we note here that the warming associated with rotation did indeed relax some radiation-induced strains. The relaxation was a net advantage, however, if anything, as it tended to restore lost contrast and delay the appearance of small bubbles.

Acknowledgements

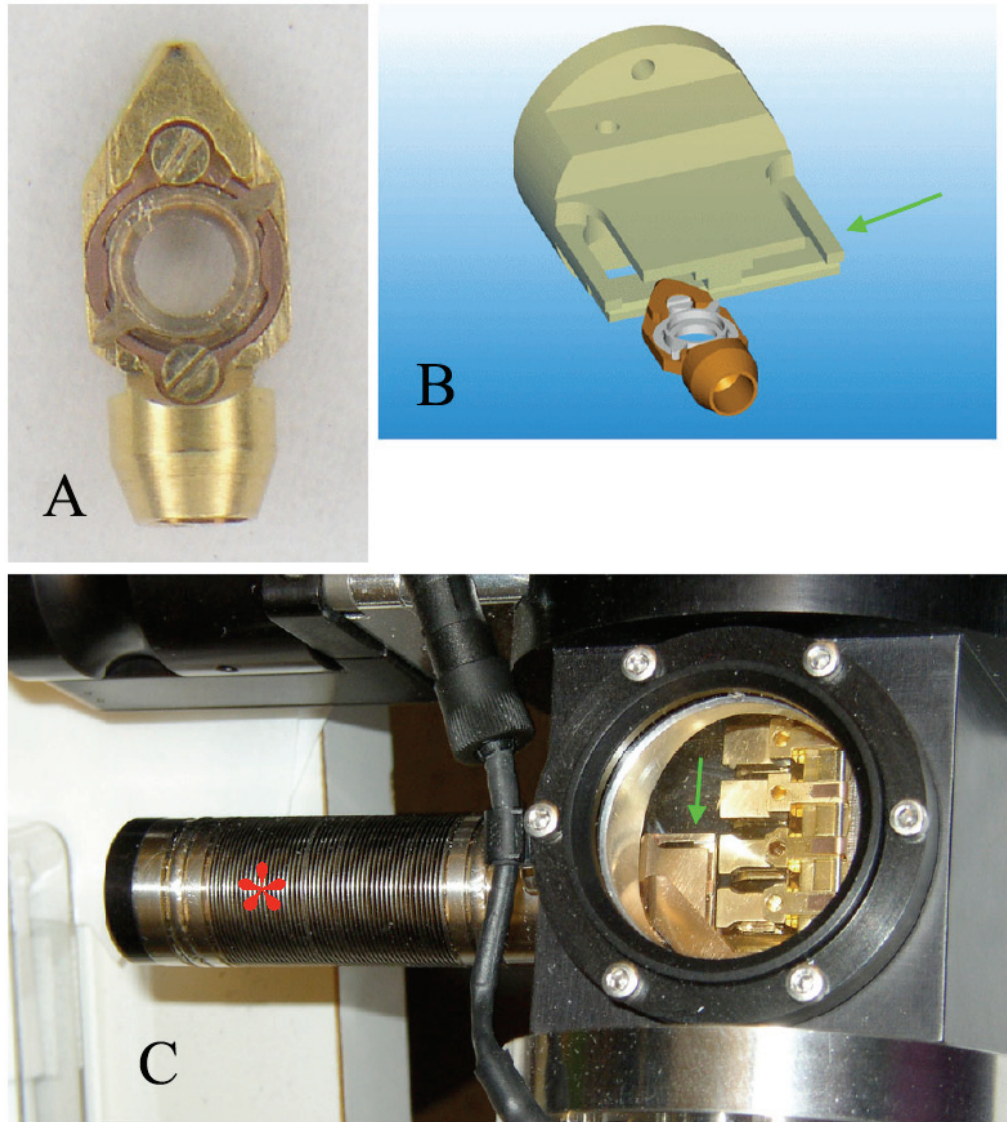
We thank D. Mastronarde for assistance with IMOD, H.J. Ding and B. Wen for image processing, A. Martino for providing purified carboxysomes, W. Sundquist for purified HIV-1 virus-like particles, and S. Tivol for reading the manuscript. This work was supported in part by NIH Grant PO1 GM66521 to GJJ, DOE grant DE-FG02-04ER63785 to GJJ, the Beckman Institute at Caltech, and gifts to Caltech from the Ralph M. Parsons Foundation, the Agouron Institute, and the Gordon and Betty Moore Foundation.

References

1. Batson, P.E., N. Dellby, and O.L. Krivanek, *Sub-angstrom resolution using aberration corrected electron optics*. Nature, 2002. **418**(6898): p. 617-20.
2. Hosokawa, F., et al., *A spherical aberration-corrected 200 kV TEM*. J. Electron Microsc., 2003. **52**(1): p. 3-10.
3. Ziese, U., K.P. de Jong, and A.J. Koster, *Electron tomography: a tool for 3D structural probing of heterogeneous catalysts at the nanometer scale*. Applied Catalysis A:General, 2004. **260**(1): p. 71-74.
4. Subramaniam, S. and J.L.S. Milne, *Three-dimensional electron microscopy at molecular resolution*. Annu. Rev. Biophys. Biomol. Struct., 2004. **33**: p. 141-155.
5. Baumeister, W., *Mapping molecular landscapes inside cells*. Biol. Chem., 2004. **385**(10): p. 865-72.
6. Penczek, P., et al., *Double-Tilt Electron Tomography*. Ultramicroscopy, 1995. **60**(3): p. 393-410.
7. Mastronarde, D.N., *Dual-axis tomography: an approach with alignment methods that preserve resolution*. J. Struct. Biol., 1997. **120**(3): p. 343-52.
8. McEwen, B.F. and M. Marko, *The emergence of electron tomography as an important tool for investigating cellular ultrastructure*. J. Histochem. Cytochem., 2001. **49**(5): p. 553-64.
9. Dubochet, J., et al., *Cryo-electron microscopy of vitrified specimens*. Q. Rev. Biophys., 1988. **21**(2): p. 129-228.

10. Hsieh, C.E., et al., *Electron tomographic analysis of frozen-hydrated tissue sections*. J. Struct. Biol., 2002. **138**(1-2): p. 63-73.
11. Al-Amoudi, A., et al., *Cryo-electron microscopy of vitreous sections*. EMBO J., 2004. **23**(18): p. 3583-8.
12. Nickell, S., et al., *Pyrodictium cannulae enter the periplasmic space but do not enter the cytoplasm, as revealed by cryo-electron tomography*. J. Struct. Biol., 2003. **141**(1): p. 34-42.
13. Beck, M., et al., *Nuclear pore complex structure and dynamics revealed by cryoelectron tomography*. Science, 2004. **306**(5700): p. 1387-90.
14. Grünewald, K., et al., *Three-dimensional structure of herpes simplex virus from cryo-electron tomography*. Science, 2003. **302**(5649): p. 1396-8.
15. Cyrklaff, M., et al., *Cryo-electron tomography of vaccinia virus*. Proc. Natl. Acad. Sci. U.S.A., 2005. **102**(8): p. 2772-7.
16. Kürner, J., A.S. Frangakis, and W. Baumeister, *Cryo-electron tomography reveals the cytoskeletal structure of Spiroplasma melliferum*. Science, 2005. **307**(5708): p. 436-8.
17. Frangakis, A.S. and R. Hegerl, *Noise reduction in electron tomographic reconstructions using nonlinear anisotropic diffusion*. J. Struct. Biol., 2001. **135**(3): p. 239-50.
18. Benjamin, J., et al., *Three-dimensional structure of HIV-1 virus-like particles by electron cryotomography*. J. Mol. Biol., 2005. **346**(2): p. 577-588.
19. Cannon, G.C., et al., *Microcompartments in prokaryotes: carboxysomes and related polyhedra*. Appl. Environ. Microbiol., 2001. **67**(12): p. 5351-61.

20. Mouche, F., et al., *Automated three-dimensional reconstruction of keyhole limpet hemocyanin type I*. J. Struct. Biol., 2003. **144**(3): p. 301-12.
21. Heymann, J.B., *Bsoft: image and molecular processing in electron microscopy*. J. Struct. Biol., 2001. **133**(2-3): p. 156-69.
22. Frank, J., *Single-particle imaging of macromolecules by cryo-electron microscopy*. Annu. Rev. Biophys. Biomol. Struct., 2002. **31**: p. 303-19.

Figure and table legends.**Figure A-1. Flip-flop rotation stage.**

Panel A: photograph of a flip-flop cartridge. The lower (non-pointed) end houses threads used to mount the cartridge to the end of the specimen rod, which resides permanently in the microscope. The inner cup can be rotated, and has two protrusions

seen here at “2-” and “8-o’clock.” For scale, the cup circumscribes grids 3 mm across.

Panel B: a drawing of a flip-flop cartridge positioned in front of the rotation tool (courtesy FEI Company and Gatan UK). The rotation tool is like a two-car garage in that it could house the cartridge in either of two positions, here seen as “left” and “right” sides. If the rotation tool were pushed over the cartridge as aligned in the drawing, its front edge would catch the right cup protrusion and cause the cup to rotate 90°. Panel C: a photograph of the part of the multispecimen holder that houses the rotation tool.

Through the circular glass window on top, cartridge docking positions 3 (top) through 6 (bottom) are visible on the right, and the front edge of the rotation tool is visible on the left (green arrows in panels B and C point to rotation tool in the same orientation).

Pushing the bellowed piston (red asterisk) seen on the left side of the photograph moves the tool over and around cartridge docking positions 5 and 6, rotating any cartridges that may be present into either the flip or flop orientation, depending on their position.

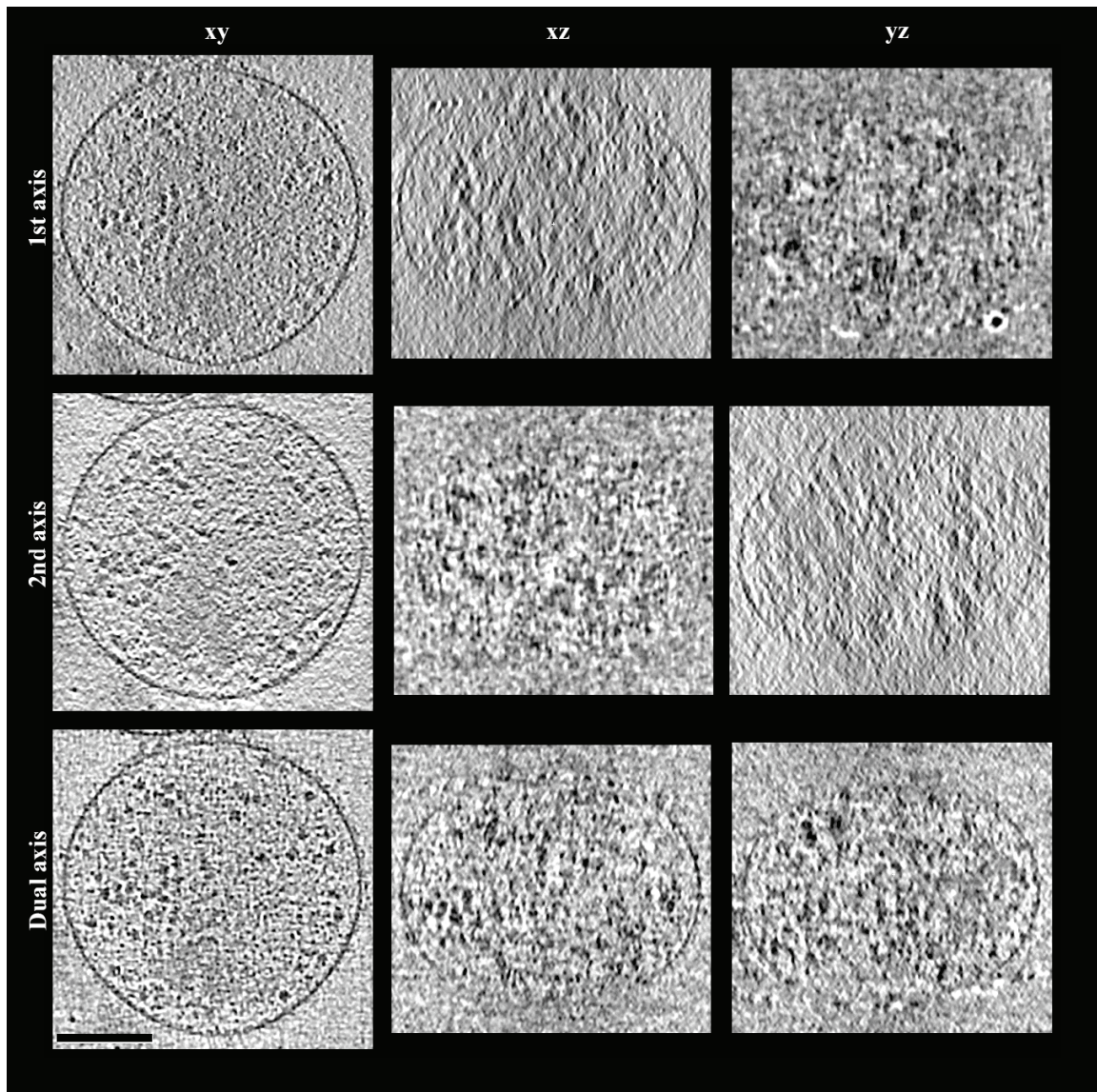


Figure A-2. Single- and dual-axis tomograms of an intact cell.

On the top, middle, and bottom rows are shown single slices of the first single-axis tomogram, the second single-axis tomogram, and the combined dual-axis tomogram, respectively, of an intact *M. florum* cell. The left, middle, and right columns show XY, XZ, and YZ slices, respectively. While individual macromolecular complexes are visible in the XY slices of all three tomograms, only in the dual-axis tomogram are the densities resolved (punctate) in all three directions. The extended but still not complete definition

of the membrane clearly reveals the improved but still anisotropic point-spread-function.
Scale bar is 150 nm.

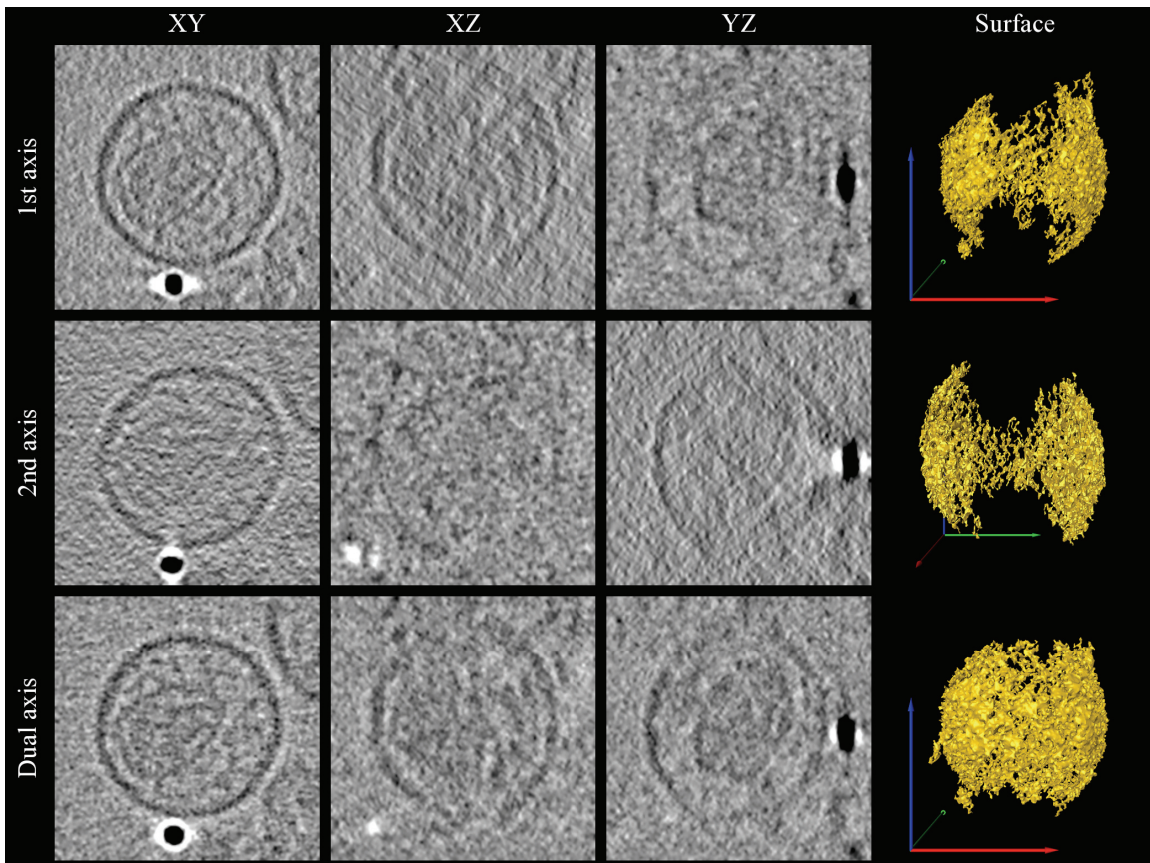


Figure A-3. Single- and dual-axis tomograms of an HIV-1 virus-like particle.

XY, XZ, and YZ slices from the first single-axis tomogram (top), the second single-axis tomogram (middle), and the combined dual-axis tomogram (bottom) of an HIV-1 virus-like particle are shown as in Fig. A-2. The outer bilayer/matrix layer and the capsid are visible. A single gold fiducial also appears at the bottom of the XY slices and on the right side of the YZ slices, which shows well the asymmetry of the point-spread-function in the single-axis tomograms. Dual-axis tilting makes this point-spread-function round in the XY slice, but it is still elongated in the Z direction. Three-dimensional renditions of the continuous envelope density are shown on the far right (note that the

view in the second row has been rotated 90° relative to the others to show its missing wedge). These isosurfaces were defined by the “Magic Wand” tool in the Amira software package, which marks voxels that are both connected to an initial seed voxel and have densities higher than a user-specific value. For scale, the diameters of the gold fiducial and virus-like particle are 10 and ~ 125 nm, respectively.

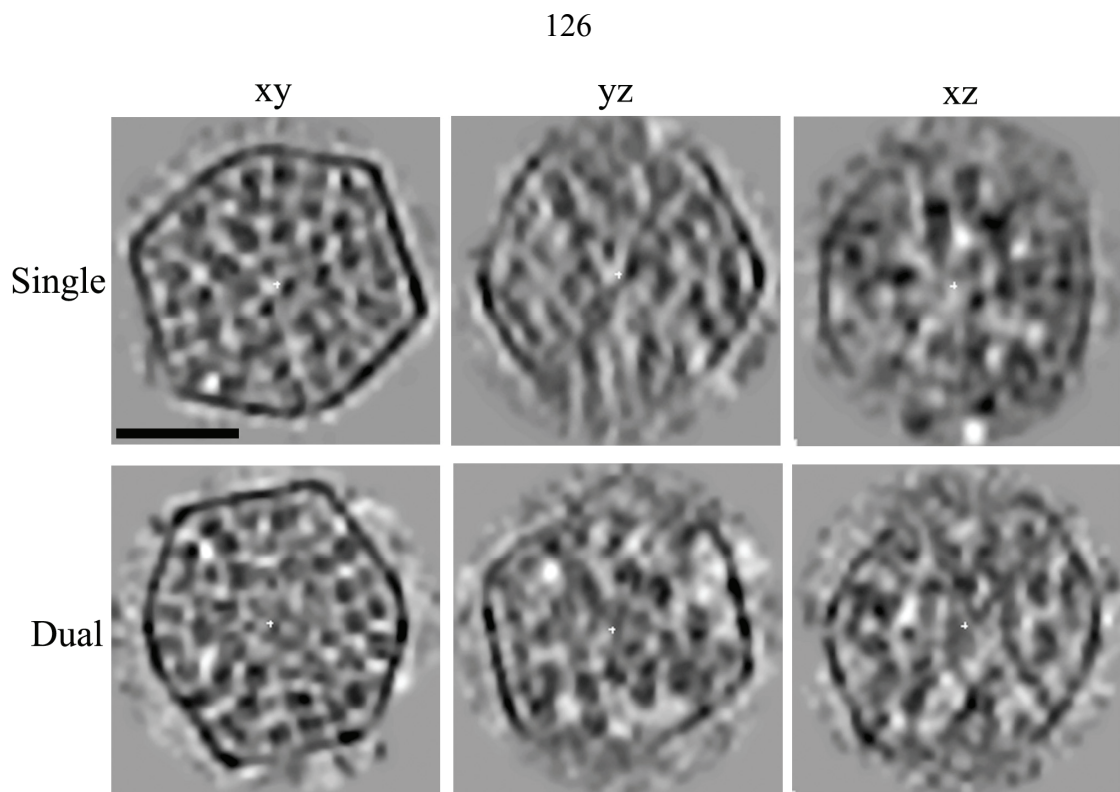


Figure A-4. Single- and dual-axis tomograms of prokaryotic carboxysomes.

XY, YZ, and XZ slices through the tomograms of two different carboxysomes are shown. The outer protein shell can be seen enclosing many tens of RuBisCO enzymes inside. Each tomogram used the same total dose, so the improvements in the dual-axis tomogram are due to data collection geometry rather than any increase in dose. Scale bar is 50 nm.

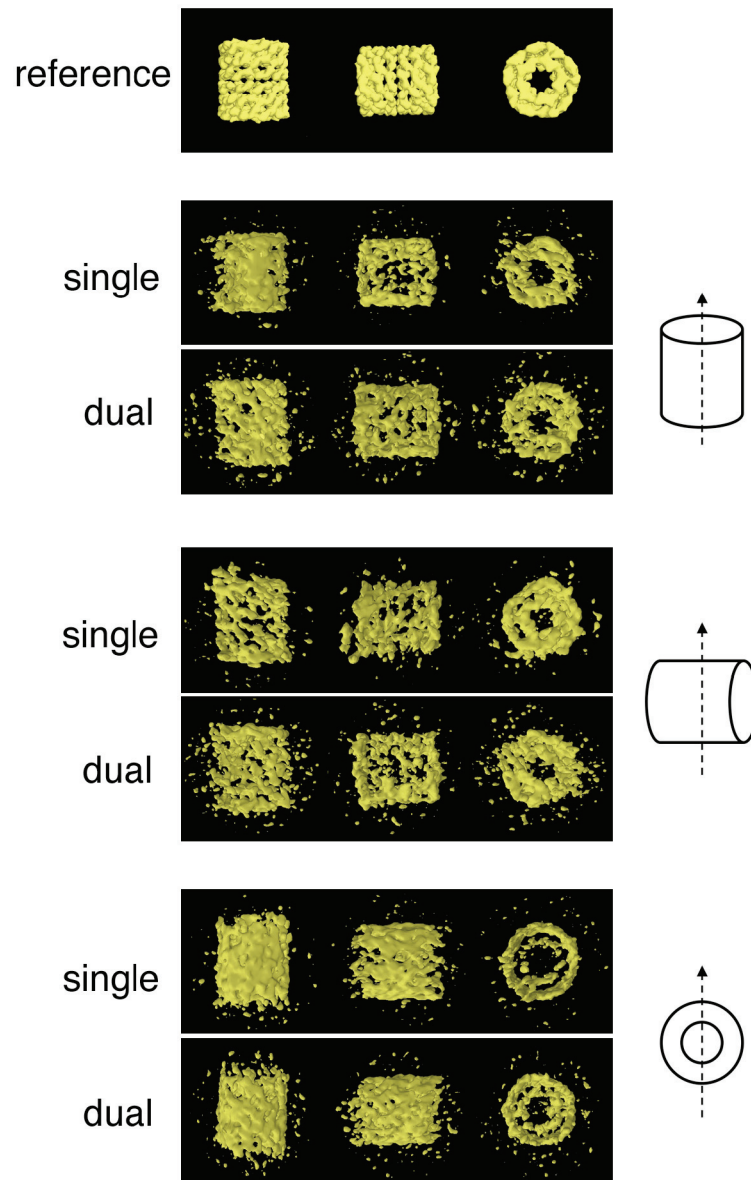


Figure A-5. Single- and dual-axis tomograms of individual protein complexes.

Surface renderings of seven independent reconstructions of the barrel-shaped hemocyanin protein complex are shown. Each row presents one reconstruction, seen from three different points-of-view. The top row displays the 12 Å “single-particle” reconstruction obtained by averaging hundreds of projection images [20], and is shown

for comparison and orientation. The even- and odd-numbered rows show single- and dual-axis tomograms, respectively, generated with the same total dose. The particular particles shown were chosen to control for and reveal how orientation in the ice, as depicted on the right, influenced the results. In the schematic, the dotted line represents the tilt axis (or the first tilt axis in the case of the dual-tilt tomograms), and the plane of the schematic represents the plane of the grid. Simple isosurfaces are shown, contoured at 2.5 standard deviations above the mean. For scale, hemocyanin is ~35 nm in length.

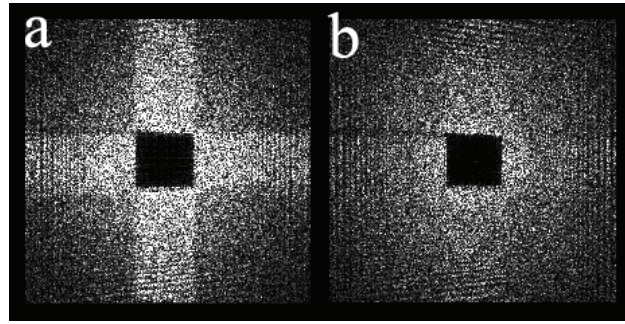


Figure A-6. Missing pyramid and intensity scaling.

Sections from the three-dimensional power spectrum of a reconstructed *M. florum* cell are shown. Both are the fortieth XY section above the central “ $Z = 0$ ” section, so that the missing pyramid is visible as a square in the middle. In (a), the overweighted intensities in the singly-measured regions of reciprocal space appear as a bright cross. The same section is shown in (b) after application of the new intensity scaling function.

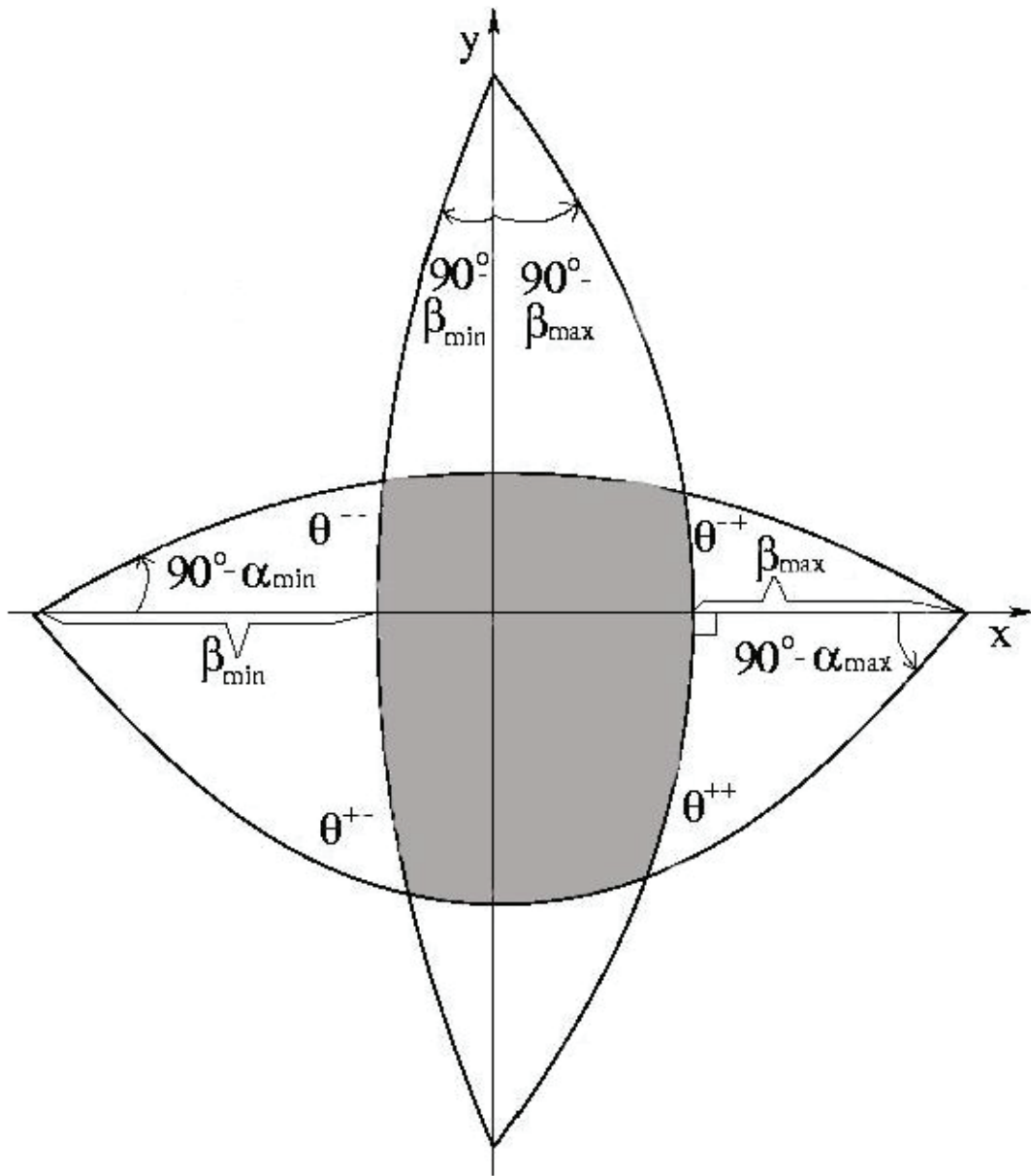


Figure A-7. Diagram used to find the area of the “missing pyramid.”

The four large arcs delineate the angular limits of data collection in the two orthogonal tilt-series (α_{\min} , α_{\max} , β_{\min} , and β_{\max}) on the surface of a sphere in reciprocal space. The area of the missing pyramid is equal to the “angular excess” of the shaded spherical quadrilateral, and is found as described in the text.

Tilt range	Thickness increase at angular extreme	Percent of reciprocal space unmeasured	
		Single-axis data collection	Dual-axis data collection
$\pm 60^\circ$	2.0×	33%	16%
$\pm 67^\circ$	2.6×	26%	10%
$\pm 70^\circ$	2.9×	22%	7.5%
$\pm 81^\circ$	6.4×	10%	1.6%

Table A-1. Percent coverage of reciprocal space in single- and dual-axis tomography.